FABRICATION, CHARACTERIZATION AND MODELLING OF HIGH EFFICIENCY INVERTED POLYMER SOLAR CELLS

José Guadalupe Sánchez López

UNIVERSITAT ROVIRA I VIRGILI
FABRICATION, CHARACTERIZATION AND MODELLING OF HIGH EFFICIENCY INVERTED POLYMER SOLAR CELLS
José Guadalupe Sánchez López

UNIVERSITAT ROVIRA I VIRGILI
FABRICATION, CHARACTERIZATION AND MODELLING OF HIGH EFFICIENCY INVERTED POLYMER SOLAR CELLS
José Guadalupe Sánchez López

José Guadalupe Sánchez López

FABRICATION, CHARACTERIZATION AND MODELLING OF HIGH EFFICIENCY INVERTED POLYMER SOLAR CELLS

Ph. D. Thesis

Supervised by

Prof. Josep Pallarès Marzal

Departament d'Enginyeria Electrònica, Elèctrica I Automàtica

Nanoelectronic and Photonic Systems (NePhoS)

UNIVERSITAT ROVIRA i VIRGILI

Tarragona

2018

UNIVERSITAT ROVIRA I VIRGILI
FABRICATION, CHARACTERIZATION AND MODELLING OF HIGH EFFICIENCY INVERTED POLYMER SOLAR CELLS
José Guadalupe Sánchez López

UNIVERSITAT ROVIRA i VIRGILI

Escola Tècnica Superior D'Enginyeria
Departament d'Enginyeria Electrònica, Elèctrica i Automàtica
Campus Sescelades
Avinguda dels Països Catalans, 26
43007 Tarragona
Espanya
Tel.: + 34 977 559 610 / 559 728
Fax: + 34 977 559 605

I state that the present study, entitled "Fabrication, characterization and modelling of high efficiency inverted polymer solar cells" presented by José Guadalupe Sánchez López for the award of the degree of Doctor, has been conducted under my supervision at the Department of Electrical, Electronic and Automatic Engineering of this University, and that it satisfies all requirements to be eligible for the International Doctorate Award.

Tarragona, 29th June 2018

Doctoral Thesis Supervisor

Dr. Josep Pallarès Marzal

UNIVERSITAT ROVIRA I VIRGILI
FABRICATION, CHARACTERIZATION AND MODELLING OF HIGH EFFICIENCY INVERTED POLYMER SOLAR CELLS
José Guadalupe Sánchez López

Acknowledgments

I would like to express my gratitude and sincere appreciation to my supervisor, Dr. Josep Pallarès, for his gentleness, encouragement, advice, support and for guidance me throughout this PhD thesis. I thank him for sharing with me his invaluable experience and knowledge.

I would also like to thank Dr. Lluis F. Marsal for providing me the opportunity to complete this work. Thank you for his invaluable support and leadership. He always encouraged me to reach my own goals. I like to take a time to thank Dr. Josep Ferré-Borrull for always being close to this work and helping me whenever I needed it.

I would like to thank Dr. Elizabeth von Hauff for offering me the opportunity to work and learn in her research group at the Vrije Universiteit Amsterdam, the Netherlands. I appreciate her support, advice and the encouraging discussions.

A special mention to Dr. Emilio Palomares and his work team from ICIQ for their support and collaboration in characterization measurements and result discussions. I am also grateful to the staff at the Servei de Recursos Cientifics i Tècnics, Dr. Lukas Vojkuvka and Dr. Mariana Stankova, for their support and patience during the characterization sessions.

I would like to especially thank Dr. Magali Estrada and Dr. Antonio Cerdeira, for trusting me in all aspects and for their invaluable support. They always sharing with me their experience, knowledge and friendship.

I like to take a time to thank Dr. Víctor Balderrama and Dr. Aurelien Viterisi for their comments and suggestions of the scientific articles. To them both, sincerely thank for sharing with me their experience, knowledge and friendship. I like thank to Dr. Pilar Formentín for her friendship and her invaluable assistance during this work.

I would like to thank the whole members of Nephos group, past and present, for their collaboration and friendship: Karen, Víctor, Aurelien, Pilar, Maria A., Peilin,

Maria P., Gerard, Pedro, Caterina, Elizabeth, Chris, Pili, Francesc, Laura and Jakub. I would also like to express my gratitude to all my friends with I whom shared every day these years: Javier, Gloria, baby boy Óliver, Maricarmen, Carlos, Edith, Francoise, Jonathan, Harold, Sara, Magaly, Angel, Isai, Yoanlys, Sandra, Arturo.

I am very grateful to my wife Karen, for filling me up with so much love and happiness, for being there whenever I needed her. This work would have never been possible without her support. Thank you for being the woman whom I love, respect and admire.

I would like to thank my family. To my mother Carmelita and father Jesús, for their unconditional love, trust and encouragement throughout my whole life. To my brothers Lauder and Carlos and my sister Yedid for your unconditional support and love, for a whole life together. To my nephews Jesús, Valentin, Diego and my nieces Kamilah, Carmelita, Ana Paula, Elisa and Johari. I love you with all my heart.

I would like to thank all my friends and family from México for their support, love and encouragement during this work and my whole life. Families: López Zavala, Sánchez Aquino, Sánchez López, Acosta Capilla, Capilla Bermudez, Velázquez López, Sánchez Zavala, López Elers, Cervantes Acosta, Sánchez García, Ramírez Acosta, Sánchez Reyes, López Sánchez, Villalobos Sánchez, Sánchez Camacho, Sánchez Castillejos, Almazán González, Cruz Martínez and Corona Sandoval. To all of you and those people that I did not mention, thank you.

This work was funded by:

Marti i Franquès Grant from Rovira i Virgili University

Spanish Ministry of Economy and Competitiveness (MINECO) grants: TEC 2012-34397, TEC 2015-71324-R and TEC2015-71915-REDT

Catalan Authority under projects: AGAUR 2014-SGR 1344, AGAUR 2017 SGR 1527

ICREA for the ICREA Academy Award

List of Abbreviations

Ag	—	Silver
a-Si	—	Amorphous silicon
Ba	—	Barium
BHJ	—	Bulk heterojunction
Ca	—	Calcium
CE	—	Charge extraction
CdTe	—	Cadmium telluride
CIGS	—	Copper indium gallium selenide
CSP	—	Concentrating solar power
CT-state	—	Charge-transfer state
D/A	—	Donor/Acceptor
DC	—	Direct current
DIO	—	1,8-diiodooctane
DOS	—	Density of states
E_g	—	Energy gap
EQE	—	External quantum efficiency
ETL	—	Electron transporting layer
FF	—	Fill factor
HOMO	—	Highest occupied molecular orbitals
HTL	—	Hole transporting layer
ICBA	—	Indene-C 60 bisadduct
ITO	—	Indium tin oxide
iPSCs	—	Inverted polymer solar cells
IJP	—	Inkjet printing
IS	—	Impedance spectroscopy
J	—	Current density

J_{Ph}	—	Photo-current density
J_{SC}	—	Short circuit current density
J-V	—	Current density *vs.* voltage
LiF	—	Lithium fluoride
LUMO	—	Lowest unoccupied molecular orbitals
Mg	—	Magnesium
MoO_3	—	Molybdenum oxide
Mw	—	Molecular weight
n_{id}	—	Ideality factor
NiO	—	Nickel oxide
NREL	—	National Renewable Energy Laboratory
OSCs	—	Organic solar cells
$PC_{60}BM$	—	[6,6]-phenyl-C61-butyric acid methyl ester
$PC_{70}BM$	—	[6,6]-phenyl-C71 butyric acid methyl ester
PCDTBT	—	Poly[N-9′-heptadecanyl-2,7-carbazole-alt-5,5-(4′,7′-di-2-thienyl-2′,1′,3′-benzothiadiazole)]
PCE	—	Power conversion efficiency
PCPDTBT	—	Poly[2,6-(4,4-bis-(2-ethylhexyl)-4H-cyclopenta [2,1-b;3,4-b′]dithiophene)-alt-4,7(2,1,3-benzothiadiazole)]
PDI	—	Polydispersity index
PDTP-DFBT	—	Poly[2,7-(5,5-bis-(3,7-dimethyloctyl)-5H-dithieno[3,2-b:2′,3′-d]pyran)-alt-4,7-(5,6-difluoro-2,1,3-benzothiadiazole)]
PDTSTTz	—	Poly[2,6-(4,4′-bis(2-ethylhexyl)dithieno[3,2-b:2′,3′-d] silo-le)-alt-5,5′-(3,6-bis[4-(2-ethylhexyl)thienyl-2-yl]-s-tetrazine]

PEDOT:PSS	—	Poly(3,4-ethylenedioxythiophene)-poly(styrenesulfonate)
PFDTBT	—	Poly{[2,7-(9,9-bis-(2-octyl)-fluorene)]-alt-[5,5-(4,7-di-20-thienyl-2,1,3-benzothiadiazole)]}
PFN	—	Poly [(9,9-bis(3'-(N,N-dimethylamino)propyl)-2,7-fluorene)-alt-2,7-(9,9dioctyl-fluorene)]
PSBTBT	—	Poly[(4,40-bis(2-ethylhexyl) dithieno[3,2-b:20,30-d] silole)-2,6-diyl-alt-(2,1,3-benzothiadia-zole)-4,7-diyl]
PSCs	—	Polymer solar cells
PTB1	—	Poly((4,8-bis(octyloxy)benzo(1,2-b:4,5-b')dithiophene 2,6-diyl)(2-(dodecyl-oxy)carbonyl)thieno(3,4-b)thiophenediyl))
PTB7	—	Poly[[4,8-bis[(2-ethylhexyl)oxy]benzo[1,2-b:4,5-b']dithiophene-2,6-diyl][3-fluoro-2-[(2-ethylhexyl)carbonyl]thieno[3,4-b]thiophene diyl]]
PTB7-Th	—	Poly[4,8-bis(5-(2-ethylhexyl)thiophen-2-yl)benzo[1,2-b;4,5-b']dithiophene-2,6-diyl-alt-(4-(2-ethylhexyl)-3-fluoro-thieno[3, 4-b]thiophene-)-2-carboxylate-2-6-diyl)]
PTFE	—	Polytetrafluoroethylene
PV	—	Photovoltaics
P3HT	—	Poly (3-hexylthiophene)
RMS	—	Root-mean-square
R_S	—	Series resistance
R_{Sh}	—	Shunt resistance
R2R	—	Roll-to-roll
SC	—	Spin coating
Si	—	Silicon

T	—	Temperature
TE	—	Thermal evaporation
TiO_x	—	Titanium oxide
TPV	—	Transient photovoltage
V	—	Voltage
V_{OC}	—	Open circuit voltage
V_2O_5	—	Vanadium oxide
ZnO	—	Zinc oxide

List of Figures

List of Tables

List of Contributions

Journal Articles

1. V. S. Balderrama, **J. G. Sánchez**, G. Lastra, W. Cambarau, S. Arias, J. Pallarès, E. Palomares, M. Estrada, L. F. Marsal, "High-efficiency organic solar cells based on a haloid salt and polyfluorene polymer with high alignment-level of cathode selective contact", *Journal of Materials Chemistry A*, *Just accepted*, 2018

2. Y. Galagan, L. Ciammaruchi, R. Oliveira, A. Charas, Tulus, E. von Hauff, G. Polino, F. Brunetti, R. Hansson, E. Moons, M, Krassas, G. Kakavelakis, E. Kymakis, **J. G. Sánchez**, J. Ferre-Borrull, L. F. Marsal, S. Züfle, et al., "Stability of Organic Solar Cells with PCDTBT donor polymer: an inter-laboratory study", *Journal of Materials Research, 33 (13), 1909–1924,* 2018.

3. **J. G. Sánchez**, V. S Balderrama, S. I Garduño, E. Osorio, A. Viterisi, M. Estrada, J. Ferré-Borrull, J. Pallarès, L. F. Marsal, "Impact of inkjet printed ZnO electron transport layer on the characteristics of polymer solar cells", *RSC Advances 8 (24), 13094-13102,* 2018.

4. E. Osorio, **J. G. Sánchez**, L. N. Acquaroli, M. Pacio, J. Ferré-Borrull, J. Pallarès, L. F. Marsal, "Degradation Analysis of Encapsulated and Nonencapsulated TiO_2/PTB7:$PC_{70}BM$/V_2O_5 Solar Cells under Ambient Conditions via Impedance Spectroscopy", *ACS Omega 2 (7), 3091-3097,* 2017.

5. **J. G. Sánchez**, V. S. Balderrama, M. Estrada, E. Osorio, J. Ferré-Borrull, L. F. Marsal, J. Pallarès, "Stability study of high efficiency polymer solar cells using TiO_x as electron transport layer", *Solar Energy 150, 147-155,* 2017.

6. V. S. Balderrama, F. Avila-Herrera, **J. G. Sánchez**, J. Pallarès, O. Vigil-Galán, L. F. Marsal, M. Estrada, "Organic solar cells toward the fabrication under air environment", *IEEE Journal of Photovoltaics 6 (2), 491-497,* 2016.

7. V. S. Balderrama, **J. G. Sánchez**, M Estrada, J. Ferre-Borrull, J. Pallarès, L. F. Marsal, "Relation of polymer degradation in air with the charge carrier concentration in PTB1, PTB7, and PCBM layers used in high-efficiency solar cells", *IEEE Journal of Photovoltaics 5 (4), 1093-1099,* 2015.

Communications to Conferences

1. **J. G. Sánchez**, V. S. Balderrama, S. I. Garduño, E. Osorio, A. Viterisi, M. Estrada, J. Ferré-Borrull, J. Pallarès and L. F. Marsal, "Inverted Polymer solar with Inkjet printed ZnO as ETL", *Stability of Emerging Photovoltaics from Fundamentals to Applications, SEPV,* Barcelona, Spain, 2018. (Oral and poster presentation)

2. M. P. Montero-Rama, **J. G. Sánchez**, C. Stenta, A. Viterisi, J. Pallarès and L. F. Marsal, "Thin Film Metal Oxides as Electron Transport Layer for Efficient Polymer Solar Cells", *Nano PT,* Lisbon, Portugal, 2018. (Poster presentation)

3. **J. G. Sánchez**, V. S. Balderrama, A. Viterisi, M. Estrada, J. Ferré-Borrull, L. F. Marsal and J. Pallarès, "Influence of Pd-doped TiO_x on inverted organic solar cells performance", *European photovoltaic solar energy conference and exhibition, EU PVSEC,* Amsterdam, The Netherlands, 2017. (Poster presentation)

4. V. S. Balderrama, **J. G Sánchez**, M. Estrada, J. Pallarès, J. Ferré-Borrull, L. F Marsal, "Air Dependence of Electrical Performance Parameters in Polymeric Organic Solar Cell", *The Electrochemical Society Meeting*, New Orleans, USA. 2017, (Oral presentation).

5. **J. G. Sánchez**, V.S. Balderrama, M. Estrada J. Ferré-Borrull, L. F. Marsal and J. Pallarès, "Influence of Pd-Doped TiO_x on Performance Parameters of High Efficiency Organic Solar Cells", *Spanish Conference on Electron Devices, CDE*, Barcelona, Spain, 2017. (Oral presentation)

6. **J. G. Sánchez**, V. S. Balderrama, M. Estrada, J. Ferré-Borrull, J. Pallarès and L.F. Marsal, "Inverted Polymer Solar Cells using Pd-doped TiO_x as Cathode Buffer Layer", *Graduate Students Meeting on Electronics Engineering,* Tarragona, Spain, 2017. (Poster presentation)

7. **J. G. Sánchez**, V.S. Balderrama, M. Estrada, J. Ferrè-Borrull, L.F. Marsal and J. Pallarès, "Inverted BHJ solar cells based on PTB7:$PC_{70}BM$ using TiO_x as electron transport layer", *Spanish Nanophotonics Conference, CEN*, Valencia, Spain, 2016, (Oral presentation)

8. **J. G. Sánchez**, V. S. Balderrama, M. Estrada, E. Osorio, J. Ferré-Borrull, L.F. Marsal and J. Pallarès, "Fabrication, Characterization and Stability Analysis of Inverted Polymer Solar Cells", *Graduate Students Meeting on Electronics Engineering,* Tarragona, Spain, 2016. (Oral presentation)

9. **J. G. Sánchez**, V. S. Balderrama, M. Estrada, J. Ferré-Borrull, L.F. Marsal and J. Pallarès, "Performance Comparison of BHJ Organic Solar Cells Based on P3HT with $PC_{70}BM$ and ICBA", *IEEE Autumn Meeting on Power, Electronics and Computing, ROPEC*, Ixtapa, Mexico, 2015. (Oral presentation)

10. **J. G. Sánchez**, V.S. Balderrama, M. Estrada, J. Ferré-Borrull, L.F. Marsal and J. Pallarès, "Inverted Bulk Heterojunction Organic Solar Cell Based on PTB7:$PC_{70}BM$ with a Titanium Oxide as Electron Transport Layer", *Graduate Students Meeting on Electronics Engineering,* Tarragona, Spain, 2015. (Poster presentation)

"I don't study to know more, but to ignore less"

Sor Juana Inés de la Cruz

"I am just a child who has never grown up.
I still keep asking these 'how' and 'why' questions.
Occasionally, I find an answer"

Stephen Hawking

UNIVERSITAT ROVIRA I VIRGILI
FABRICATION, CHARACTERIZATION AND MODELLING OF HIGH EFFICIENCY INVERTED POLYMER SOLAR CELLS
José Guadalupe Sánchez López

CONTENTS

Chapter 1

Introduction

1.1 Background

During the last decade, many progress on the renewable energy field research has been achieved. The advances on the renewable energy technologies still allow obtaining good performances with lower cost than fossil fuel prices. For this reason, the interest of public and private organizations in clean, renewable and sustainable energy sources such as hydroelectric, wind power, bioenergy, geothermal, ocean and solar has increased. Solar energy is one of the most common renewable energy technology because of the possibility to use the energy of sun directly. Some technologies such as solar thermal heating and cooling, concentrating solar power (CSP) and solar photovoltaics (PV) capture the solar energy (in form of radiant light or heat) to transform it in a useful energy for human benefit. Among them, the PV is the most developed solar energy technology. The Solar PV (also called solar cells) convert the sunlight energy (photons) into electricity (voltage) by the photovoltaic effect. Nowadays, important advances in solar cells technology field have been achieved. There have been emerged new technologies alternative energy source based on inorganic and organic materials to the traditional solar cells systems.

1.2 Motivation

Since the first evidence of photovoltaic effect in polymer:fullerene blend, the organic solar cells based on these materials were considered as a promising low-cost energy source. Recently, the research on organic solar cells based on polymer:fullerene materials have progressively growing due to the lastly efficiencies over 10%. Several research groups

have focused on the development of more efficient polymer materials for OSCs applications. Moreover, the studies on the manufacturing process and device' engineering allowed to develop different OSC's architecture with more efficient interpenetrating network morphology. The development of OSCs with inverted architecture, as well as the synthesis of polymers based on thieno[3,4-b]-thiophene and benzodithiophene marked a turning point in the research of high efficient OSCs. These two-progress allowed to fabricate single junction OSCs based on polymers materials (PSCs) with both high photon conversion and charge carrier extraction efficiencies. Moreover, the development of PTB-based polymers and inverted architecture prompted to researchers to develop PSCs with a tandem architecture.

For these reason, this thesis is focused on the fabrication, characterization and modelling of single junction high efficient PSCs with inverted architecture (iPSCs). The iPSCs concerned were fabricated with two of the most efficient PTB-based polymers blended with a fullerene used as active layer.

1.3 Aims of the thesis

The major aim of this thesis is:

- Fabrication, characterization and modelling of high efficient polymer:fullerene-based solar cells with inverted architecture.

Additionally, there are several specific aims:

1. To analyse the effect of an ultra-thin layer of titanium oxide as an electron transport layer in the performance of inverted polymer solar cells based on PTB7:$PC_{70}BM$.

2. To analyse the stability and lifetime of the PTB7:$PC_{70}BM$-based iPSCs with TiO_x (TiO_x-iPSCs) in comparison to similar PSCs which use different electron transport layers.

3. To analyse the stability of TiO_x-iPSCs under different degradation conditions.

4. To determine the loss mechanisms in TiO_x-iPSCs based on PTB7-Th:$PC_{70}BM$ by electrical and optical characterization.

5. To analyse the effect of zinc oxide film deposited by inkjet printing (ZnO-IJP) as an electron transport layer on the performance of PTB7-Th:$PC_{70}BM$-based PSCs, for use in the large-scale manufacture of PSCs.

6. To analyse the performance of iPSCs based on PTB7-Th:$PC_{70}BM$ with ZnO-IJP in comparison to similar iPSCs using ZnO deposited by different thin layer deposition techniques.

7. To determine the loss mechanisms in iPSCs based on PTB7-Th:$PC_{70}BM$ with ZnO deposited by different techniques by electrical, photophysical and optical characterization.

1.4 Summary

The thesis is organized as follows:

Chapter 2 presents a literature review as introduction to the organic semiconducting materials. The basics, operation principles and performance parameters of organic solar cells are described. The different architectures of organic solar cells are introduced. A brief introduction to organic solar cell based on polymer:fullerene is also presented. Finally, the state-of-the-art of the most important semiconducting polymer used for organic solar cell applications are described.

Chapter 3 introduces the polymer donor and fullerene acceptor materials used for the devices fabrication. Moreover, the materials used as buffer layers and electrodes are presented. The operation principle of the different thin-films coating and printing technologies used for the devices fabrication are described. The full step-by-step process for the fabrication of devices is also described. Finally, the methodology for the devices characterization used in this thesis is discussed.

Chapter 4 describes the fabrication and characterization of iPSCs based on PTB7:$PC_{70}BM$ using a titanium oxide (TiO_x) film as electron transport layer (ETL). The effects of TiO_x on the performance parameters and stability of iPSCs compared to the effects on conventional PSCs and iPSCs using PFN as ETL is presented. The results of impedance spectroscopy analysis on encapsulated and non-encapsulated TiO_x-iPSCs under ambient conditions are discussed. Finally, the effects of the palladium-doped TiO_x layer on the performance of iPSCs are shown.

Chapter 5 presents the effects of ZnO layers deposited by inkjet printing as electron transport layer ETL on the performance of iPSCs based on PTB7-Th:$PC_{70}BM$ active layers. The performance of iPSCs with ZnO-IJP are compared to that of iPSCs with ZnO deposited by spin coating (ZnO-SC) and thermal evaporation techniques (ZnO-TE). Finally, results obtained from electrical, optical and photophysical characterization measurements of iPSCs with ZnO-IJP, ZnO-SC and ZnO-TE are discussed.

Chapter 6 presents the general conclusions of the thesis and resume the overall results achieved during this research. The further works related to this research are also presented.

Chapter 2

Basics of organic solar cells

2.1 Introduction

Since the first-time observation of the photovoltaic effect in 1839 by Becquerel[1], some important advances in solar energy technology have been developed. The first solar cell, based on a layer of selenium covered with a thin film of gold, was reported by Fritts in 1883.[2] In 1954, Bell Laboratories developed the first inorganic solar cell (silicon-based) cell with an efficiency of 6%.[3] While the first organic solar cell (based on a bilayer of phtalocyanine and perylene derivatives) was reported in 1986 by Tang with an efficiency of 1%.[4] The exponential growth of the global operating capacity of solar cell in the last years (as shown in Figure 2.1) has driven the developing of cost-competitive and high efficiency solar cells technologies.

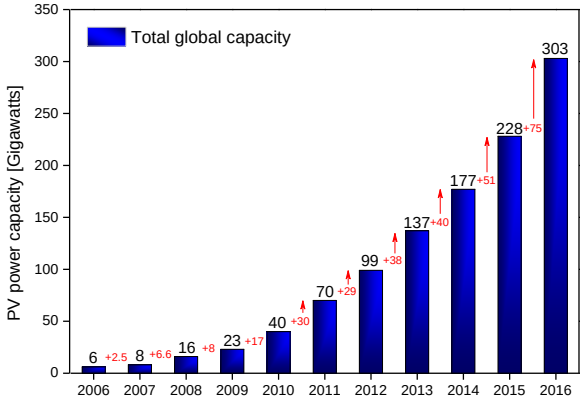

Figure 2.1 Global operating capacity of PV from 2006 to 2016 [*Source IEA PVPS]*

The progress on photovoltaic technology has been divided mainly in three solar cells generations. The first-generation solar cells are based on silicon (Si) wafer technology with a record performance of 26.7%.[5] This solar cell technology exhibits great advantages such as good performance

and high stability. However, making high quality silicon used as raw material in this technology fabrication is time-consuming and expensive. For this reason, the second-generation solar cells based on amorphous silicon (a-Si), cadmium telluride (CdTe) and copper indium gallium selenide (CIGS) were developed. The advantages of the second-generation solar cell lie in the lower production costs (in comparison to Si wafers technology) and their high performance with a record efficiency of 22.6%.[6] Nevertheless, the vacuum and high temperature post-treatments processes are still limiting the fabrication cost of these solar cells. The third-generation solar cells are focused on high-efficiency photon conversion devices at a cheaper production cost. Several solar cells technologies such as dye-sensitized cells (11.9%)[7], quantum dots cells (11.3%)[8], perovskite solar cells (21%)[9] and organic solar cells (11.5%)[10] have been classified as third-generation solar cell technologies. Figure 2.2 shows several record efficiencies reached by different solar cell technologies.

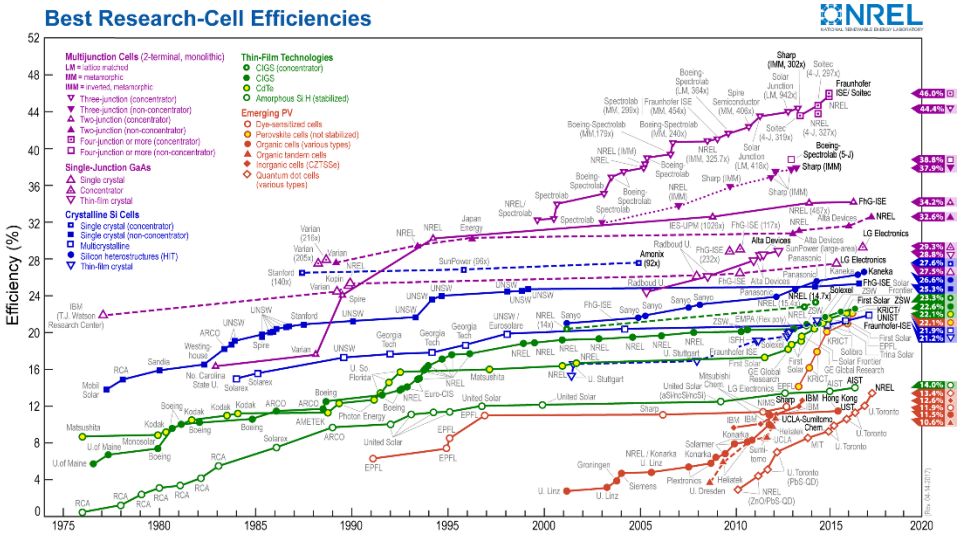

Figure 2.2 Currently record efficiencies in solar cells
[*Source: National Renewable Energy Laboratory (NREL)*]

During the last years, the interest of the research community on organic solar cells (OSCs) has grown. The OSCs are composed of organic semiconducting materials, so-called small molecules and polymers. The features that differentiate OSCs from all the others technologies are their light-weight, high transparency, as well as their low-cost and straightforward fabrication on large-scale flexible substrates.[11] Another important characteristic of OSCs is the high absorption coefficients of the organic materials, which provide thin devices (~100 nm) with high absorption. However, the low charge-carrier mobility and small diffusion length of excitons in organic materials limit the efficiency of these devices.[12] Since then, studies have focused on new organic materials design and on the engineering of device architecture directed toward improving cell performance.

2.2 Organic semiconductor materials

Organic semiconductors are materials mainly based on carbon and hydrogen atoms, and some hetero-atoms such as oxygen, nitrogen and sulphur. The semiconducting properties of these materials lie in the alternation between single and double carbon-carbon bonds. The single bonds (so-called σ-bonds) are associated with localized electrons, and double bonds contain both σ and π-bonds. The electronic configuration of carbon in the ground state is: $1s^2\ 2s^2\ 2p_x^1\ 2p_y^1\ 2p_z^0$.[13] According to this, carbon atoms should form two covalent bonds due to its two unpaired electrons:

$$\underset{1s}{\uparrow\downarrow}\ \underset{2s}{\uparrow\downarrow}\ \underset{2p_x}{\boxed{\uparrow}}\ \underset{2p_y}{\boxed{\uparrow}}\ \underset{2p_z}{\ }$$

However, it is well known that carbon atoms can form four covalent bonds. To do so, one electron must be promoted from orbital *2s* to the orbital *2pz*, which leads the generation of four *sp* hybrid orbitals. The orbital hybridization of carbon atoms allows them bond to themselves (and to other atoms) with *sp, sp^2, and sp^3* hybrid orbitals.

2.2.1 The *sp* and sp^3 hybridizations

In *sp* hybridization, the $2s^2$ orbital and one of the *2p* orbitals combine to form two *sp* orbitals (each composed of 50% *s* and 50% *p*) but leave the other *2p* electrons unchanged. This results in a linear arrangement with an angle of 180° between bonds, which reduce electron repulsion. The two other *2p* orbitals, at 90° to one another and to the two *sp* orbitals, are available for π-bonding. Figure 2.3a shows the *sp* hybridization of carbon. In the case of sp^3 hybridization, the $2s^2$ and the three *2p* orbitals combine and four hybrid sp^3 bonds (σ-bounds) are formed with bonds angle of 109.5°. Therefore, the materials with this type of hybridization are poor conductors because all electrons are well localized in the σ-bonds.[14,15] The sp^3 hybridization of carbon is shown in Figure 2.3b.

2.2.2 The sp^2 hybridization

Especially this type of hybridization is the most common in organic semiconductors. Here, the hybridization of the *2s* and *2p* orbitals forms three sp^2 orbitals and leaves the 2*pz* orbital unchanged. The sp^2 orbitals are positioned with 120^o between them forming a triangle in a plane, while the *pz* orbital is placed in the plane perpendicularly to the three sp^2 orbitals.[14] The overlap of sp^2 orbitals results in a stronger σ-bonds, while the overlap of *pz* orbitals forms delocalized π-bonds (see Figure 2.3c).

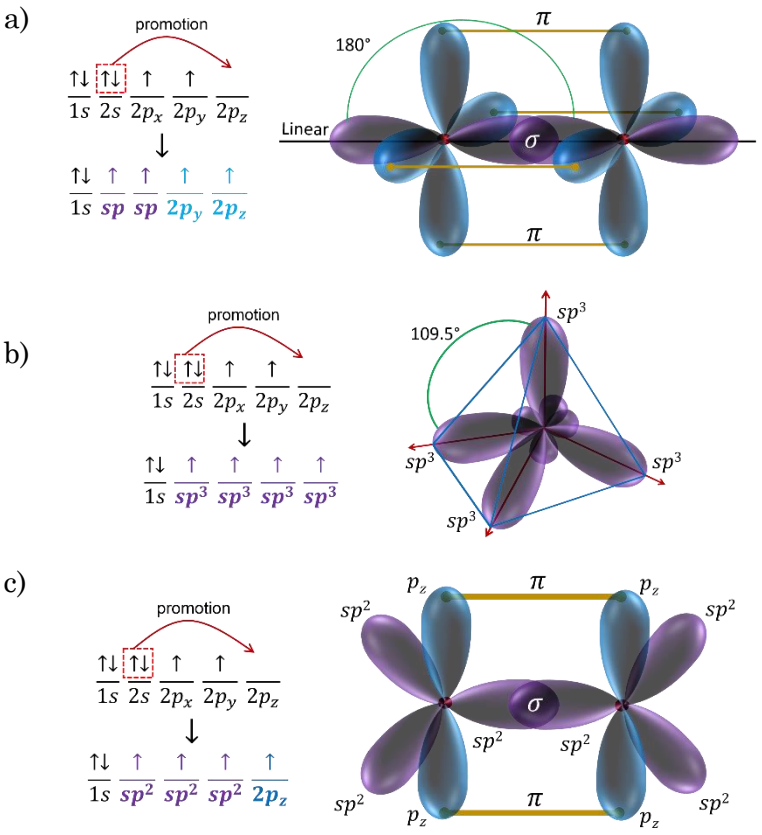

Figure 2.3 Schematic representation of *sp* (a), sp^3 (b) and sp^2 (c) hybridizations of carbon

The mobility of π-electrons is higher than thus of the σ-electrons because they can move freely between carbon atoms. The delocalized π-electron is responsible for the electrical conductivity in organic semiconductor materials. The ability to absorb photons of these materials lie in the antibonding π^*-state, which is an energy near to that of the π-state. The interactions of π^*-orbitals form a conduction band, so-called lowest unoccupied molecular orbitals (LUMO), whereas interactions of π-orbitals yield a valence band known as highest occupied molecular orbitals (HOMO). The two bands are separated by an energy gap (E_g). Figure 2.4 shows the energy levels splitting of orbitals in a π-conjugated

molecule. The HOMO and LUMO of organic semiconductors determine their electrical and optical properties.[14,15]

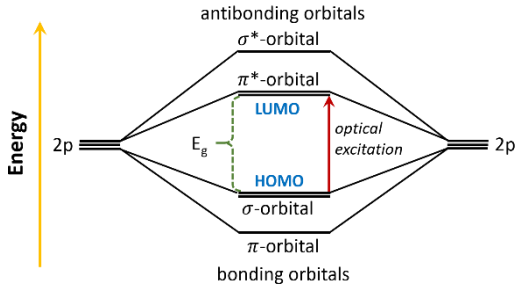

Figure 2.4 Energy levels splitting of orbitals in a π-conjugated molecule

The position of the absorption band of organic semiconductors is determined by the E_g of HOMO-LUMO. Moreover, the LUMO determines the ionization potential and the HOMO, the electron affinity of the materials. These two properties define the ability to donate or accept electrons. Organic semiconductors with higher HOMO levels usually work as electron-donor material with hole-transporting ability, (p-type semiconductors), while those with lower LUMO levels can act as electron-acceptor and electron transporting materials (n-type semiconductors). π-conjugated materials are molecules bonded by van der Waals forces, resulting in weaker intermolecular bonds. Consequently, the delocalization of electronic wave functions is much weaker having directly impact on the charge transport of the materials. The charge transport in these materials occurs by intermolecular hopping among the highly localized charge carriers. The hopping rate in organic π-conjugated materials is usually described by two theoretical models: Miller-Abrahams formalisms[16] and the Marcus theory.[17] Although Miller-Abrahams formalisms were used to describe the hopping rates in inorganic semiconductors, they are also often used to describe these in

organic semiconductors because of their simplicity. On the other hand, Marcus' expressions calculate the hopping rate, considering an intermediate energetic barrier originated from energetic relaxation. Since an efficient charge transport lie in the capability of charges to move from molecule to molecule, the charge carrier mobility plays an important role in hopping transport. In organic semiconductors, the charge carrier mobility is influenced by several factors such as the high electron-vibration coupling, weak electronic coupling, molecular packing, disorder, impurities, and molecular weight.[18]

2.3 Physics of organic solar cells

In a solar cell, the light absorbed by the semiconductor material results in the generation of excitons (electron-hole pair attracted to each other by the electrostatic Coulomb force). The separation of excitons in free charges is caused by an electric field. This electric field is produced at the electrode junction to another material with a different work function (ionization energy).[19] These processes are quite complex in organic semiconductors because of their chemical impurities, semi crystalline lattice and structural disorders. As a result, generated excitons diffuse as uncharged particles through the semiconductor until be dissociated by an electric field. The charge generation process in OSCs can be described in four steps (see Figure 2.5): exciton generation, exciton dissociation, charge transporting, and charge collection.

2.3.1 Exciton generation

First, the incident sunlight is absorbed by the donor material. The light absorption is limited by many factors including the optical

absorption coefficient, the band-gap (photons with energy > E_g are absorbed), optical losses (e.g. reflection, refraction and scattering), and the overlapping of absorption spectrum of material with the solar radiation spectrum. Some organic semiconductors can absorb up to 77% of solar radiation on earth (Air Mass 1.5, or AM1.5) with thickness around 100 - 300 nm because of their relative high absorption coefficients (~10^{-5} cm^{-1}). These materials have a wide optical absorption in the visible range due to their narrow absorption bands. When light is absorbed, electrons are promoted from ground state to excited one resulting in the exciton formation[20] (see Figure 2.5a).

2.3.2 Exciton dissociation

Subsequently, the generated exciton diffuses into the donor material (exciton diffusion length ~ 20 nm) until it reaches the donor/acceptor (D/A) interface, which is energetically favourable to dissociate exciton into free charge carriers. To achieve the exciton dissociation into electron free charge, the energy difference between the ionization potential donor material and the electron affinity acceptor must be higher than the exciton binding energy (0.1 - 0.5 eV). To do so, the LUMO of acceptor must be lower than that of the donor. In this case, the energy difference between the LUMO of the donor and acceptor provides the energy necessary to dissociate the exciton into a free electron and an associated free hole. Moreover, the electric field generated by the different work-functions of the electrodes (built-in electric field) can assist the exciton dissociation. The free hole remains in the donor while the free electron is transferred to the acceptor, which takes place within 100 fs.[21] Figure 2.5b shows the exciton diffusion and separation into free charge carriers.

2.3.3 Charge transporting

Upon exciton dissociation, the free charge carriers drift toward their corresponding electrode via the donor and acceptor materials. The electrons move across the acceptor to reach the cathode electrode, while the holes are transferred to the anode electrode through the donor as depicted in Figure 2.5c. The transportation of free charge carriers to their respectively electrodes is driven by the built-in electric fields. In amorphous organic semiconductors, the charge transport mechanism is mainly performed by the hopping transport. This mechanism is less efficient than others (e.g. band transport), since amorphous organic semiconductors exhibit high trap concentrations that result in low charge carrier mobility and charge recombination.[22,23]

2.3.4 Charge collection

Finally, the free charges are collected at the electrodes. The electrons are collected at the cathode electrode (a low work function metal) and holes at the anode electrode (a high work function metal) as shown in Figure 2.5d. To perform an accurate charge carrier extraction, the LUMO level energy of acceptor should be higher than that of the work-function of the cathode, while the HOMO level energy of the donor should be lower than that of the work-function of the anode. The difference between those energies determines if contacts between organic material and electrodes are ohmic or non-ohmic. The ohmic organic/electrode contact is the most suitable for a high efficient charge collection. On the contrary, a non-ohmic contact could cause electrical losses and lower charge injection resulting in a blocking contact. The charge collection efficiency is affected by several factors such as charge transfer, dipole formation, chemical reactions, traps within the organic material, and charge recombination.[18]

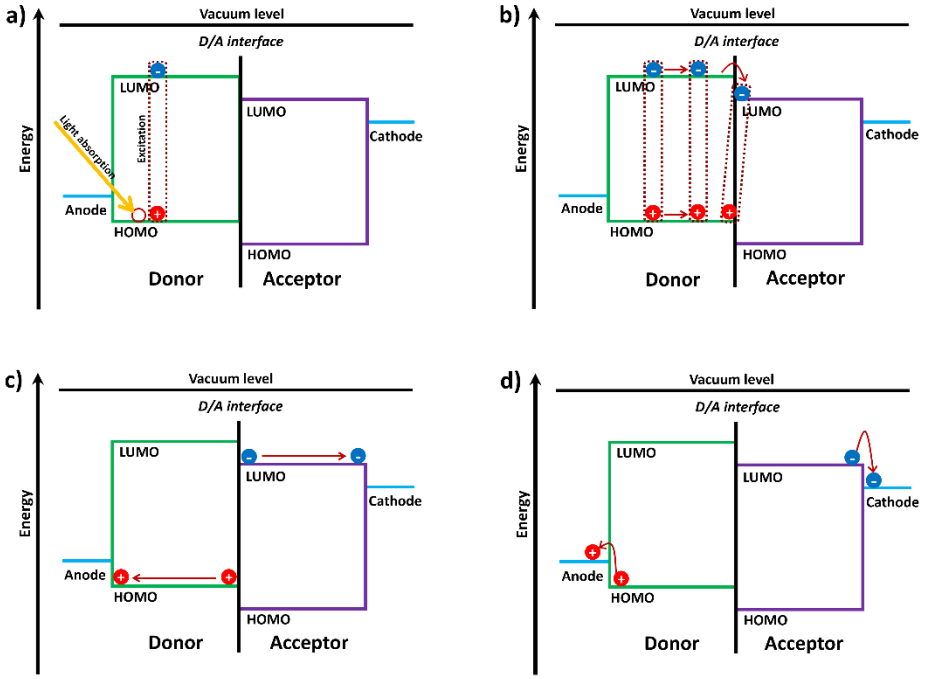

Figure 2.5 Charge generation process in OSCs: a) exciton generation, b) exciton dissociation, c) charge transporting, and d) charge collection

2.3.5 Charge extraction limiting mechanisms

During the energy conversion process, from light absorption to the collection of free charge carriers, several charge loss mechanisms, such as geminate and non-geminate recombination, can take place. The geminate, or monomolecular, recombination refers to the recombination of charge carriers during exciton dissociation. Here, the generated bound charges, or charge-transfer (CT) state[24], turn back to the ground state before dissociating into free charge carriers. Thus, the germinate recombination occurs after the exciton reaches the D/A interface and the electron-hole pair is separated, remaining the hole in the donor, while the electron is transferred to the acceptor. The electron-hole pair is strongly bounded by Coulomb interactions (CT-state) with a typical binding energy of 0.1-0.5

eV. The generated bound electron-hole pair must be dissociated into free charge carriers before geminate recombination takes place. On the other hand, non-geminate (or bimolecular) recombination describes the recombination of free charge carriers after exciton dissociation. In non-geminate recombination, two fully dissociated charge carriers diffuse to within their Coulomb capture radius of each other before recombination. This type of recombination is induced by relative high trap concentration and low charge carrier mobility of disordered organic semiconductors. The non-geminate recombination is the primary loss process that limits the photocurrent generation in OSCs, since it reduces the carrier lifetime and carrier density.[24-26] The geminated and non-geminate recombination processes are depicted in Figure 2.6.

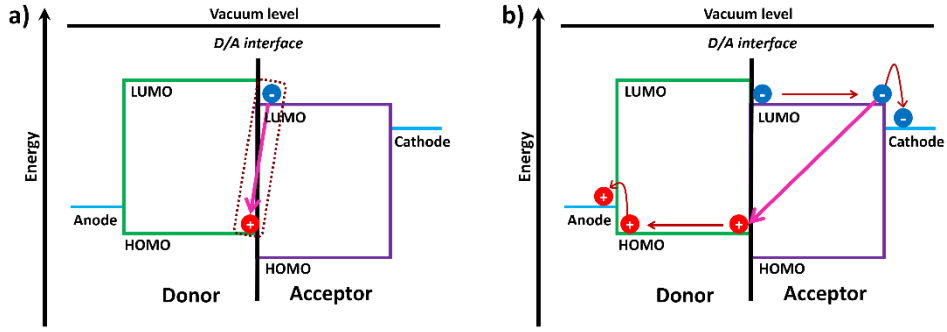

Figure 2.6 Geminate (a) and non-geminate (b) recombination mechanisms

2.4 Architecture of organic solar cells

The main architecture of organic solar cells is consisting of an organic semiconductor active layer placed between two metals, which work as the anode and cathode electrodes. One of these electrodes (the front contact) must be highly semi-transparent to ensure the maximum light absorption. A highly reflective metal is usually used as the back

contact to redirect the non-absorbed light into the organic materials. The OSCs architecture plays an important role on the exciton dissociation and transportation of charge carriers. The efficient exciton dissociation is driven by the built-in electric field (formed by the work function difference of electrodes) and by the strong drop of potential at the interfaces: donor/acceptor and semiconductor/electrodes. The most basic architectures of OSCs are single layer, bilayer heterojunction, and the bulk heterojunction. These architectures are based on active layers comprised by two materials (donor and electron acceptor), excluding the single layer architecture which is comprised by only one material.[27,28] The main differences among OSCs' architectures are the exciton dissociation, and the charge transport mechanisms.

2.4.1 Single layer OSCs

The single layer is the simplest architecture of OSCs, in which a photoactive organic material (typically p-type) is sandwiched between two electrodes with different work functions (see Figure 2.7a). In this architecture, a Schottky barrier is formed between the p-type organic semiconductor and the electrode with lower work function.[29] On the other hand, an ohmic-contact is formed between the organic semiconductor and the electrode with higher work function. The work function difference between the electrodes creates an electric field in the organic layer. The electric field causes the band bending of the HOMO and LUMO, starting at the Schottky barrier depletion region *W* (rich in electrons), close to the low work function electrode. Therefore, the electric field dissociates the excitons generated in the depletion layer and the free electrons are collected at the low work function electrode.[28] The free holes are transported through the organic semiconductor to the electrode with high

work function, as shown in Figure 2.7b. The single layer OSCs exhibit low power conversion efficiencies (< 1%). Since the exciton diffusion length is lower than 20 nm in organic materials, only the excitons generated in the depletion region contribute to the photocurrent. Moreover, the electric field is usually not strong enough to achieve an effective exciton dissociation. The free charge carriers move through the same material; therefore, the recombination depends of electron and hole concentrations.[30]

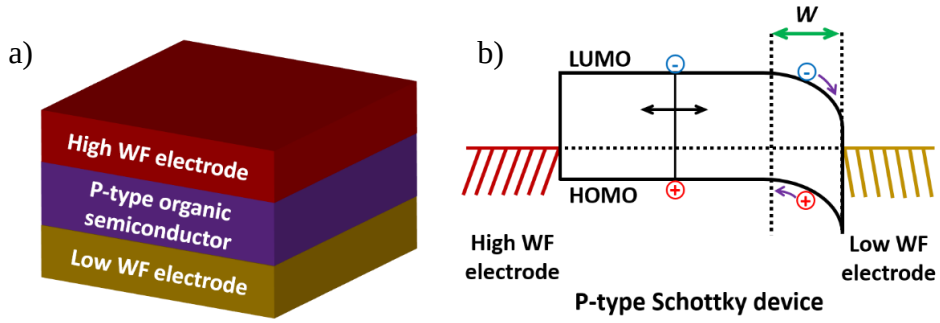

Figure 2.7 Single layer architecture of OSCs (a); exciton diffusion and dissociation process in a single layer OSCs with a Schottky contact at low work function electrode (b)[28]

2.4.2 Bilayer heterojunction OSCs

The bilayer heterojunction architecture includes a donor and an acceptor material stacked together with a planar interface. The organic bilayer is placed between two electrodes with different work functions. In the bilayer OSCs, the exciton dissociation takes place at the planar interface by effect of the large potential drop between donor and acceptor. To ensure an accurate charge extraction, the donor HOMO is matched to the electrode with higher work function, while the acceptor LUMO is matched to the electrode with lower work function.[31] Figure 2.8a shows

the bilayer heterojunction architecture. Upon light absorption in the donor, the photogenerated exciton diffuses, until it reaches the donor/acceptor interface, at which, the difference between the ionization potential and electron affinity of materials, allows the separation of the electron and hole from their Coulomb potential bond. Then, the holes remain in the donor HOMO and the electrons are transferred to the acceptor LUMO. The free charge carrier moves to their respective electrodes to be finally collected, the electrons at the low work function electrode and the holes at the high work function electrode (see Figure 2.8b). The main advantages of this cell structure, over the single layer architecture are the more efficient exciton dissociation and the monomolecular charge transport, thus the recombination is reduced, depending mostly on trap densities. Nevertheless, the efficiency of bilayer OSCs is still low, since the exciton diffusion length is only of few nanometers and the typical donor layer needs a thickness of at least 100 nm to absorb enough light.[32] However, in a thicker layer to provide enough absorption of light, the exciton can be generated far from the donor/acceptor interface, in which case it will not be dissociated and recombines.

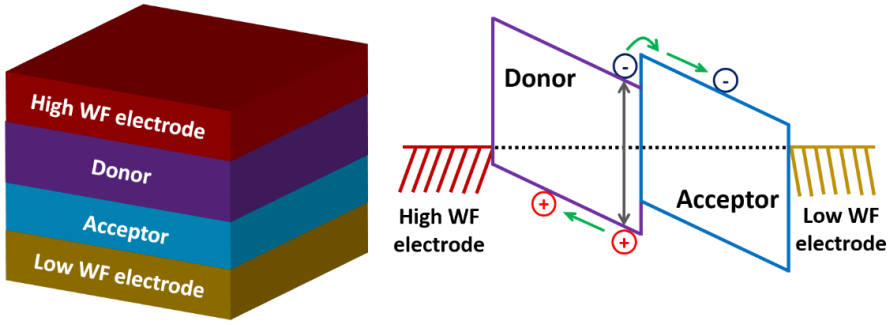

Figure 2.8 Bilayer heterojunction architecture of OSCs (a); exciton diffusion and dissociation process in a bilayer heterojunction OSCs (b)[28]

2.4.3 Bulk heterojunction OSCs

In bulk heterojunction OSCs, the donor and acceptor materials are mixed together to form a blend that will be used as active layer of the cell. Thereby, the donor/acceptor interfacial area within a distance less than the exciton diffusion length is maximized. The operation principle of bulk heterojunction OSCs is similar to the bilayer one, but the donor/acceptor interface area for exciton dissociation is largely increased (in comparison to the planar bilayer architecture) allowing the efficient exciton dissociation everywhere in the bulk. The increment of the donor/acceptor area lies in the formation of the interpenetrated network due to phase segregations.[33] The architecture of bulk heterojunction OSCs is depicted in Figure 2.9. Bulk heterojunction OSCs exhibit much higher efficiencies in comparison to bilayer OSCs, since the interpenetrated network dispersed in the bulk, allows to dissociate more excitons within their lifetime. Unlike bilayer OSCs, in which the donor/acceptor materials contact their corresponding electrode, in bulk heterojunction OSCs the donor and acceptor phases form a bi-continuous and interpenetrating network determining the shape, crystallinity and orientation of the active layer.[34] Nevertheless, the electrons and holes conduction through the donor and acceptor phases to the electrodes is limited by the non-continuity in the interpenetrating network. Moreover, the non-continuity in the interpenetrating network and the typically low charge carrier mobility of organic semiconductors increase the probability of non-geminate recombination of generated free charge carriers. Thus, the bulk heterojunction OSCs are sensitive to the nanoscale morphology of the blend, which depends on the conditions of the manufacturing process such as donor:acceptor ratio, solvent, solvent additive, thermal annealing and post annealing and solvent annealing, among others.[35,36]

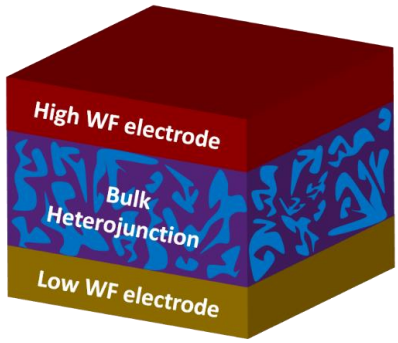

Figure 2.9 Bulk heterojunction architecture of OSCs

2.4.4 Interfacial buffer layers

In OSCs, the heterojunction between the organic semiconductors and the electrodes plays an important role in device performance since the charge extraction takes place only at these interfaces. A low quality organic/electrode interface can limit the charge extraction by appearing resistance effects, which decrease the power conversion efficiency of the device. For this reason, the HOMO and LUMO level of organic semiconductors should be considered during the electrodes choice. The most common material used as front anode electrode is the indium tin oxide (ITO) because of its high transparency, semiconducting properties, and the ability to form an ohmic contact with the HOMO level of donor material.[37,38] Some low work function metals such as calcium (Ca), magnesium (Mg), and barium (Ba) are used as back cathode electrode, due to the ohmic contact they can formed with the LUMO of the acceptor material. However, the high reactivity of these low work-function materials reduces the lifetime of devices. To solve this problem, more stable metals such gold, silver and aluminium are used as cathode. However, since the work function of these metals is higher than that of Ca, Mg or Ba, the barrier layer at the organic/cathode increases, resulting

in a lower holes collection. After great efforts to overcome these problems, it was discovered that a thin layer between the electrodes and the organic semiconductors can improve the charge collection and extraction. These layers are called buffer layers, or interfacial layers or interlayers. The effectivity of these layers lies in their ability to improve the energy-level alignment between HOMO and LUMO levels of organic materials with the work function of electrodes.[39]

Materials, such as metals, neutral polymers, salts, metals oxide, and polyelectrolytes are usually used as buffer layers in OSCs. The buffer layer between the cathode and the acceptor improves the electron transporting and collection, and it is known as electron transporting layer (ETL). The most common materials used as ETL in OSCs are: Ca, lithium fluoride (LiF), zinc oxide (ZnO), and titanium oxide (TiO_x), and the poly [(9,9-bis(3'-(N,N-dimethylamino)propyl)-2,7-fluorene)-alt-2,7-(9,9dioctyl-fluorene)] (PFN). On the other hand, the buffer layer between the anode and the donor, so-called hole transporting layer (HTL), improves the hole transporting and collection. Commonly, the molybdenum oxide (MoO_3), nickel oxide (NiO), and vanadium oxide (V_2O_5) and the poly(3,4-ethylenedioxythiophene)-poly(styrenesulfonate) (PEDOT:PSS) are used as HTL.[40]

2.4.5 OSCs with inverted architecture

For OSCs with conventional architecture, Ca and PEDOT:PSS/indium tin oxide (ITO) are commonly used as a low and high work-function metal cathode and anode, respectively. However, it is well known that Ca can easily be oxidized in the presence of oxygen. In addition, the hygroscopic and acidic nature of PEDOT:PSS may degrade

the ITO electrode and active layer, which results in a stability reduction of solar cells. All of these aspects degrade the interfaces so the resulting devices are not very stable.[41] The OSCs with inverted architecture (iOSCs) reverse the layer sequence of the conventional OSCs to improve the stability and performing of devices. Thus, the charge is collected in the opposite electrodes. In conventional OSCs the holes are collected in the transparent electrode (ITO) and the electrons in the top electrode (commonly silver or aluminium).

On the contrary, in iOSCs the electrons are collected by the ITO, whereas the holes by the silver. In iOSCs, PEDOT:PSS is replaced by a transition metal oxide (i.e., MoO_3, V_2O_5 and NiO) as the hole transport layer (HTL) because their high work-functions (>5 eV) provide low resistance ohmic contacts.[42] Moreover, in this architecture the use of easily oxidized metals is avoided, and Ca is largely replaced by PFN, ZnO or TiO_x as the electron-transport layer (ETL). These materials modify the ITO's surface and improve the charge carrier extraction.[43] Figure 2.10 shows the diagram of OSC with conventional (a) and inverted (b) architecture.

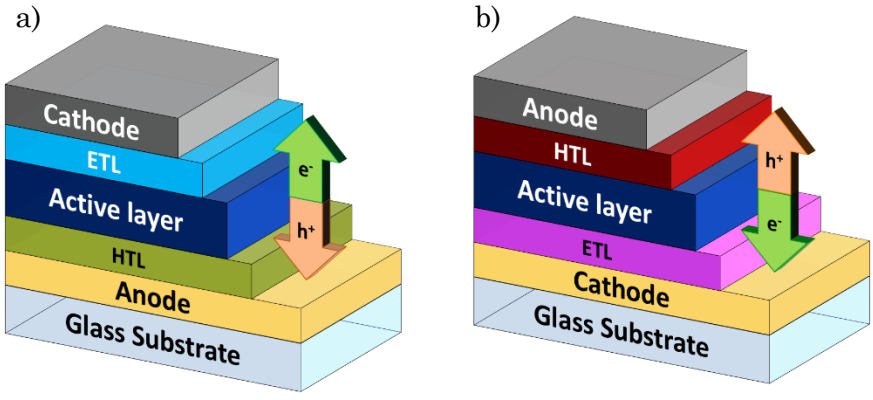

Figure 2.10 Organic solar cell with conventional (a) and inverted (b) architecture

2.5 Performance parameters of organic solar cells

The most common method to characterize the photovoltaic performance of OSCs, as well as their electrical properties, is the measurement of their current density-voltage characteristics (*J-V* curve) in the dark and under illumination conditions. To do an accurate characterization, the *J-V* measurement should be performed under standard illumination conditions (AM1.5G irradiation) and at a well-defined temperature (T = 25º C). The primary performance parameters of OSCs such open circuit voltage (V_{OC}), short circuit current density (J_{SC}), fill factor (FF) and power conversion efficiency (PCE) can be obtained from the *J-V* characteristic in the dark and under standard illumination conditions. Among these, the PCE is the most important parameter since it describes the ratio between the incident light and the maximum output power. The typical *J-V* characteristics and the photovoltaics parameters of OSCs measured in the dark and under standard illumination conditions are depicted in Figure 2.11.

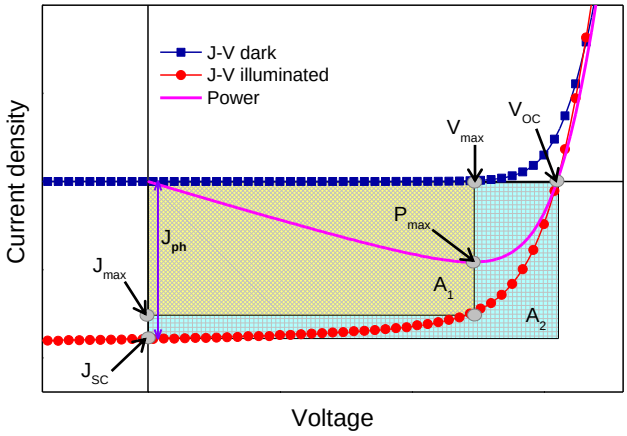

Figure 2.11 Typical *J-V* characteristic and the photovoltaics parameters of OSCs in the dark and under standard illumination at 1 Sun (100 mW cm^{-2})

The OSCs measured in dark conditions exhibit a similar current density-voltage behaviour to that of an ideal p-n junction diode. The current density can be described as follow[44]:

$$J_{dark} = J_0 \left[\exp\left(\frac{qV}{n_{id}kT}\right) - 1\right] \quad (2.1)$$

where J_0 is the saturation current density, q is electronic charge, V is the voltage, n_{id} is the ideal factor of the diode, k is the Boltzmann's constant, and T is the temperature. When the OSCs is measured under standard illumination conditions, the maximum photo-current density (J_{ph}) at $V = 0$ is equal to the current output, defined as the short-circuit current density (J_{SC}) shown in Figure 2.11.

$$J\,(V = 0) = J_{ph} = J_{SC} \quad (2.2)$$

2.5.1 Open circuit voltage (V_{OC})

The V_{OC} of OSCs under standard illumination conditions is the maximum voltage at which the net current in the device is zero. The V_{OC} is proportional to the difference between the LUMO energy level of the acceptor and the HOMO level of the donor. Nevertheless, the morphology of the blend layer, as well as the non-geminated recombination can contribute to the V_{OC} origin.[45] The equation 2.3 describes the V_{OC} with $J(V= 0)$ and for $J_{ph} >> J_0$.

$$V_{OC} = n_{id}\frac{kT}{q} ln\left(\frac{J_{ph}}{J_0} + 1\right) \quad (2.3)$$

2.5.2 Short circuit current (J_{SC})

The J_{SC} is the maximum photo-generated current of OSCs when the applied voltage is zero (see equation 2.2). The J_{SC} directly depends to optical and electrical properties of organic semiconductors such as absorption coefficient and charge carrier mobility.[46] The J_{SC} is related to the thickness and morphology of the organic semiconductors blend layer, light irradiation, and to the efficient exciton generation and dissociation.

2.5.3 Fill factor (*FF*)

The FF is a measure of the quality of OSCs in terms of power. In other words, it is the measure of the amount of power available to be extracted from the device. The FF is defined as:

$$FF = \frac{V_{max} * J_{max}}{V_{OC} * J_{SC}} \tag{2.4}$$

where $V_{max} * J_{max}$ represents the maximum power (P_{max}) produced by the device. In figure 2.11, the $V_{max} * J_{max}$ is represented as a yellow rectangle (A1), while $V_{OC} * J_{SC}$ is represented as a blue one (A2). For ideal OSCs, the fill factor is 1 (A1 = A2), nonetheless in real devices it is always lower than 1 (A1 < A2). Thus, FF can be described as:

$$FF = \frac{A1}{A2} \tag{2.5}$$

2.5.4 Power conversion efficiency (PCE)

The PCE is the main parameter of OSCs, which evaluates the capacity of a device to convert the incident photons in electrons. The PCE is directly linked to the efficiency of exciton generation and dissociation,

and to the charge extraction efficiency. Thus, the loss mechanisms involved during these processes decrease the efficiency of the devices. The PCE can be defined by the equation (2.6).

$$PCE = \frac{V_{OC} * J_{SC} * FF}{P_{In}} \quad (2.6)$$

where P_{In} is the light incident power (P_{In} = 100 mW cm^{-2}; 1 Sun AM1.5G).

2.5.5 Series and shunt resistances

The series (R_S) and shunt (R_{Sh}) resistances describe the current lost during the charge collection process. The R_S describes the resistance at the contacts, because of the partial energy level alignment between organic semiconductors and the metallic contacts, or buffer layers, which reduces the charge extraction. The charge carrier mobility through the organic semiconductors, as well as the thickness of the active layer, contribute to the origin of R_S. The main effect of high R_S on the OSCs performance is the reduction of FF, resulting in the lowering of the power output. On the other hand, the R_{Sh} describes the lost charge due to charge carriers' recombination. The low R_{Sh} in OSCs reduces their V_{OC} and FF, which results in the decrease of power output.[44] Figure 2.12a shows the effects of R_S and R_{Sh} on the *J*-*V* characteristics of OSCs.

The R_S can be calculated from the *J*–*V* curve slope at forward voltage region higher that V_{OC}. Whereas the R_{Sh} is usually calculated from the *J*–*V* curve slope at the short circuit region. The R_S and R_{Sh} are represented as two separate elements in the equivalent circuit of OSCs.[47] Figure 2.12b shows the equivalent circuit of real OSCs.

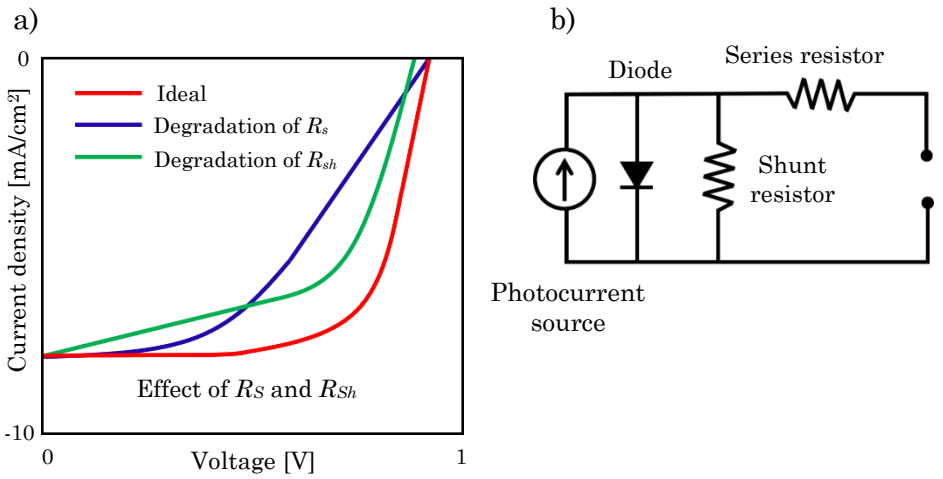

Figure 2.12 Effect of high R_S and low R_{Sh} on the *J-V* characteristics of OSCs (a). Typical equivalent circuit of organic solar cells (b)

2.6 Polymer solar cells

2.6.1 Introduction

The OSCs can be fabricated based on two type of organic semiconductor materials: organic small molecules and organic semiconducting polymers. The main difference between OSCs based on small molecules and those based on semiconducting polymers (PSCs) is the method for organic material deposition. The small molecules were commonly deposited by vapour deposition techniques under high vacuum conditions since the low solubility of these materials in common solvents. However, after a great effort in the development of high-solubility small molecules, solar cells based on solution-processed small molecule have achieved efficiencies over 10 %.[48] On the other hand, the semiconducting polymers exhibit good solubility that allows to deposit them from a solution by different coating methods. The good solubility of these materials in common solvents lies in their side chains. Semiconducting

polymers with branched side chains exhibits higher solubility than those with linear side chains of equal length and number of carbon atoms.[49,50] However, PSCs exhibit lower mobilities than devices based on small molecules since the higher molecular disorder in polymers. Despite these low mobilities, the highest efficiency of PSCs has reached 11.5%.[10]

2.6.2 Semiconducting polymers

Since the discovery of conductivity in polyacetylene[51], a great effort in the development of semiconducting polymers have done. The new approaches were focused on synthesize macromolecules with a conjugate backbone to the overcome the disadvantages of polyacetylene: its insolubility, its difficult processing, moreover it can be easily oxidized. The idea to improve the solubility of the semiconducting polyacetylene was the driving force for major research into the development of new polymer with a conjugated backbone. The new synthetized polymers such as polypyrrole, polyaniline, poly(p-phenylene), poly(phenylene vinylene), and polythiophene revealed that the control of the polymer structures induces changes in some physical properties like the solubility and the 3D arrangement.[52] The chemical structures of these conjugated polymers are depicted in Figure 2.13.

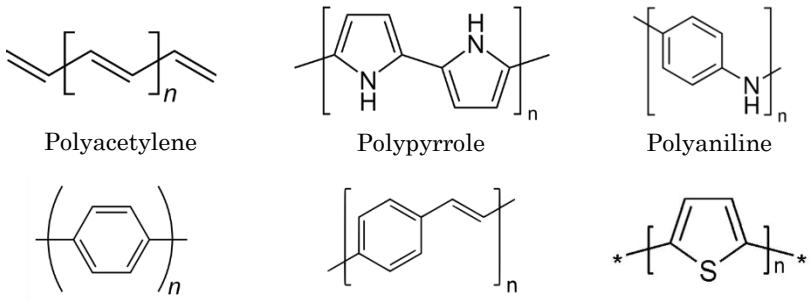

Figure 2.13 Chemical structures of some semiconducting conjugated-polymers

Among these, the polythiophenes (PTs) stood out more than others due to exhibit good electrical conductivity optical properties. The electrical and optical properties of these polymers result from the delocalized electrons in the polymer backbone. Poly (3-hexylthiophene) (P3HT) is the thiophene-based semiconductor polymer most used in the polymer solar cells fabrication due to its good stacking of the conjugated backbones. Some important milestones in the development of polymer-based organic solar cells are shown in Table 2.1.

Table 2.1 Important milestone the development of OSC

Year	Milestone
2018	Single-junction polymer solar cell (12.7%)
2017	Tandem polymer solar cell (12.8%) Non-fullerene tandem polymer solar cell (13.8%)
2016	Non-fullerene ternary polymer solar cell (12.2%)
2015	Single-junction polymer solar cell (11.7) a-Si:PDTP-DFBT hybrid tandem cell (10.5%)
2014	Triple-junction tandem polymer solar cells (12%)
2012	Tandem polymer solar cell (10.6%)
2011	Single-junction polymer solar cell (10.1%)
2009	PTB family polymer family PCE (8%)
2007	PCPDTBT:PCBM solar cells (5.5%) Tandem polymer solar cell (6.5%)
2006	Polymer solar cells with inverted architecture
2005	Bulk-heterojunction P3HT:PCBM solar cell (4-5%)
2001	Self-organised liquid crystalline solar cell of hexabenzocoronene and perylene.
1995	First bulk polymer/polymer heterojunction solar cell
1993	First polymer/C60 heterojunction solar cell

Table 2.1 Important milestone the development of OSC (continued)

1992	The photoinduced charge transfer in polymer:fullerene system is reported
1991	First dye/dye bulk heterojunction PV
1990	C60 is synthetized for the first time
1986	First heterojunction PV device
1973	Synthesis of conductive polyacetylene

2.6.3 Organic solar cells based on polymer:fullerene active layer

One of the major breakthroughs in the development of polymer-based solar cells was the introduction of the C60 fullerene as acceptor material. Since then, the interest on organic solar cells based on polymer:fullerene was rapid increase due to the growing research on the development of new semiconducting polymers and C60 derivatives. Although several blend of polymer:fullerenes (with bulk heterojunction, BHJ) were studied as active layer in PSCs[53-55], the devices based on the blend P3HT:[6,6]-phenyl-C61-butyric acid methyl ester ($PC_{60}BM$) exhibited the highest efficiency (~5%).[56, 57] This prompted to research on the synthesis of new electron donor polymers with lower band gap. However, the relatively high band-gap of P3HT (1.9 eV) restrict the photons absorbance to wavelengths below 650 nm. Moreover, the energy levels alignment between P3HT and $PC_{60}BM$ limits the V_{OC} of device to 0.6V. These issues limit the power conversion efficiency of the devices. Therefore, new electron donor polymers with lower band gap and C60 derivatives were synthetized. Thus, OSCs based on the copolymer poly [N-9′-heptadecanyl-2,7-carbazole-alt-5,5-(4′,7′-di-2-thienyl-2′,1′,3′-benzot-hiadiazole) and the [6,6]-phenylC71 butyric acid methyl ester (PCDTBT:$PC_{70}BM$) were reported with efficiencies about 6%. The

PCDTBT is a copolymer with altered structure of thiophene-benzothiadiazole-thiophene (TBT) and carbazole (Cbz) repeat units with a band gap of 1.88 eV. On the hand, $PC_{70}BM$ is a C60 derivative that exhibits higher photon collection due to its strong absorption in the visible range. Another example of low band gap polymer is the copolymer poly [2,6-(4,4-bis-(2-ethylhexyl)-4H-cyclopenta[2,1-b;3,4-b0]dithiophene)-alt-4,7-(2,1,3-benzothiadiazole)] (PCPDTBT). This copolymer exhibits a wider spectral absorption into the infrared region than that of P3HT due to its low optical bandgap (1.5 eV). The OSCs based on PCPDTBT:$PC_{70}BM$ were reported to yield an efficiency ~6%[58,59]. Besides PCDTBT and PCPDTB, polymer such as poly{[2,7-(9,9-bis-(2-octyl)-fluorene)]-alt-[5,5-(4,7-di-20-thienyl-2,1,3-benzothiadiazole)]} (PFDTBT), poly[(4,40-bis(2-ethylhexyl) dithieno[3,2-b:20,30-d]silole)-2,6-diyl-alt-(2,1,3-benzothiadia-zole)-4,7-diyl] (PSBTBT), poly[2,6-(4,4′-bis(2-ethylhexyl)dithieno[3,2-b:2′,3′-d]silo-le)-alt-5,5′-(3,6-bis[4-(2-ethylhexyl) thienyl-2-yl]-s-tetrazine] (PDTSTTz) and the fullerene derivative indene-C 60 bisadduct (ICBA), among others, were synthetized for organic solar cells applications.[60-62] The chemical structure of some conjugated polymer and fullerenes used for PSCs fabrication are shown in Figure 2.14.

2.6.4 Polymer solar cells based on PTB- family polymers

Despite great effort made to synthesize new polymers for high efficiency PSCs fabrication, these devices were not capable to exceed the barrier-efficiency of 6%. However, the first polymer solar cell with a PCE over 7% was not reported until 2010. This device was fabricated based on the polymer poly[[4,8-bis[(2-ethylhexyl)oxy]benzo[1,2-b:4,5-b']dithio-phene-2,6-diyl][3-fluoro-2-[(2-ethylhexyl)carbonyl]thieno[3,4-b]thiophene diyl]] and the fullerene $PC_{70}BM$ (PTB7:$PC_{70}BM$).[63]

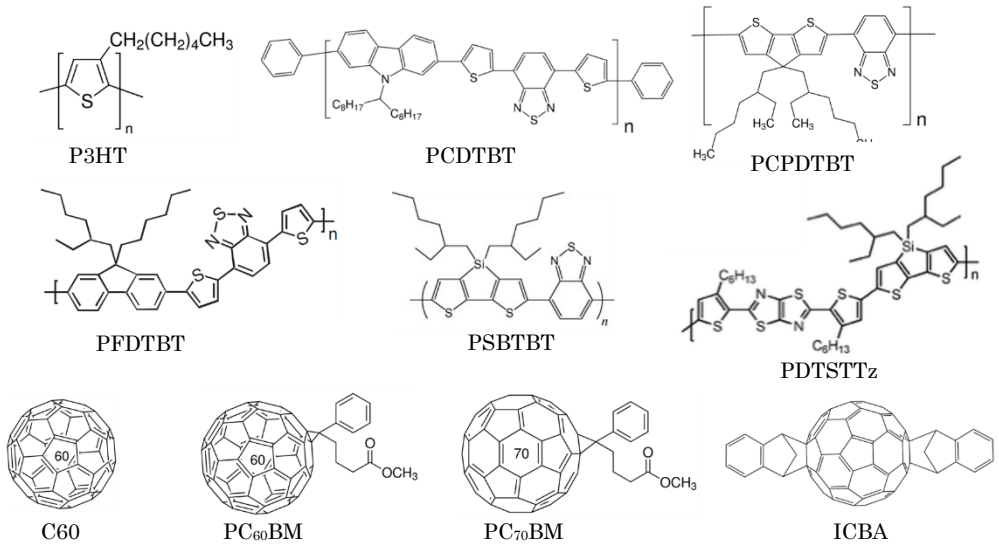

Figure 2.14 Chemical structure of some important polymers and fullerenes

PTB7 is a polymer based on altered units of thieno[3,4-b]-thiophene and benzodithiophene (PTBs) with a relative low band gap of 1.6 eV. This polymer is the result of the structural optimization progress made on the PTB-family polymers. The first devices based on a PTB-family polymer was fabricated with the poly((4,8-bis(octyloxy)benzo(1,2-b:4,5-b')dithiophene2,6-diyl)(2-(dodecyl-oxy)carbonyl)thieno(3,4-b)thioph-enediyl)) and $PC_{70}BM$ (PTB1:$PC_{70}BM$), which exhibits a power conversion efficiency of 5.6%.[64] Further PTB-based polymers (i.e. PTB2, PTB3, PTB4, PTB5 and PTB6) were developed to improve the poor solubility of PTB1 and the low V_{OC} (0.58 V) yield in devices based on it. Among these, devices made of PTB4:$PC_{60}BM$ exhibited higher V_{OC} (0.74 V) and a slightly higher PCE (6.10 %) in comparison to PTB1.[65] The differences of the physical properties among the PTB-based polymers lie on the side chains on the ester and benzodithiophene groups. The PTB-based polymers are synthesized by the Stille polycondensation reaction[66], with a varying combination of linear and branched alkyl chains[67] (see Figure 2.15).

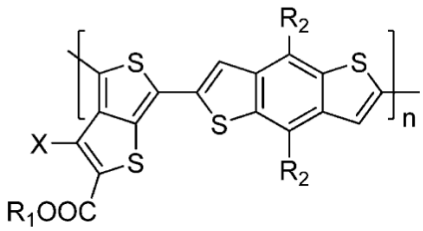

PTB1: X= H; R1= n-dodecyl; R2= n-octyloxy
PTB2: X= H; R1= 2-ethylhexyl; R2= n-octyloxy
PTB3: X= H; R1= 2-ethylhexyl; R2= n-octyl
PTB4: X= F; R1= n-octyl; R2= 2-ethylhexyloxy
PTB5: X= H; R1= n-octyl; R2= 2-ethylhexyloxy
PTB6: X= H; R1= 2-butyloctyl; R2= n-octyloxy

Figure 2.15 Chemical structure of PTB-based polymers

Currently, the highest efficiency reported for PSCs based on the PTB7:$PC_{70}BM$ is of 9.2 % using the follow inverted device architecture: ITO/PFN/PTB7:$PC_{70}BM$/MoO_3/Ag.[43] The PTB7:$PC_{70}BM$ blend was dissolved in a mixed solvent of chlorobenzene and 1,8-diiodooctane in a rate of 97:3 % by volume. One of the most highly efficient PTB-based polymer recently reported is the poly[4,8-bis(5-(2-ethylhexyl)thiophen-2-yl)ben-zo[1,2-b;4,5-b']dithiophene-2,6-diyl-alt-(4-(2-ethylhexyl)-3-fluoro-thieno[3, 4-b]thiophene-)-2-carboxylate-2-6-diyl)], so-called PTB7-Th, with a low band gap of 1.59 eV and a broad absorption up to 780 nm. Devices based on PTB7-Th:$PC_{70}BM$ with efficiency ~10 % has been reported.[68] The PTB7-Th was synthesized by replacing the alkoxy group (side chains) of the benzodithiophene group of PTB7 by an alkyl thiophene group (see Figure 2.16).

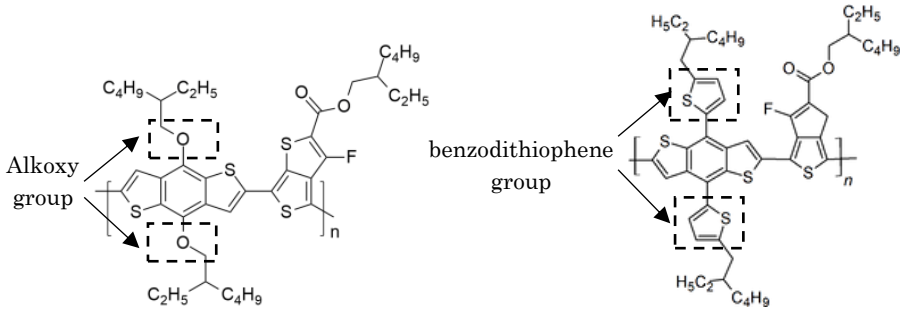

Figure 2.16 Chemical structure difference between PTB7 and PTB7-Th

Chapter 3

Fabrication and characterization of inverted polymer solar cells

3.1 Introduction

In this chapter, the donor and acceptor organic materials, the interlayer materials, as well as different thin film deposition technologies used for the fabrication of high efficiency inverted polymer solar cells are described. The fabricated devices are based on polymers of the PTB family, blended with a fullerene. Here, only the most common materials used as electron or hole transport layer for PSCs fabrication are described. In all devices, the indium tin oxide (ITO) and silver (Ag) were used as transparent contact and back contact, respectively. Although there are several techniques for thin-films deposition, only the most common techniques on lab-scale study are depicted here. The inkjet printing technique is also described and used for depositing thin-films layers. The step-by-step devices fabrication processing is described. Finally, the optical, electrical, morphological and photophysical characterization methods performed on the fabricated devices are shown.

3.2 Materials

3.2.1 Donor and acceptor materials

The inverted polymer solar cells fabricated in this thesis are based on two polymers of the PTB-family, that exhibit low band-gap, high spectral coverage of absorption and improved mobility.[65] These polymers are two of the most reported materials for OSCs, allowing to obtain high-efficiency and to improve device the stability.[69] The polymers were blended with the fullerene [6,6]-Phenyl-C71-butyric acid methyl ester ($PC_{70}BM$), due to it improved light absorption in the visible region.[70] The PTB-X:$PC_{70}BM$ is one of the best studied material combination for high

efficiency PSCs. The PTB-X:$PC_{70}BM$ materials were dissolved in 97:3 vol.% mixture of chlorobenzene (CB) and the additive diiodooctane (DIO), due to the good miscibility of these materials in CB. The additive DIO improves the fullerene solubility resulting in smaller component domain sizes, higher interfacial area and improved exciton dissociation.[71,72]

3.2.1.1 Electron donor materials

The fabricated PSCs in this thesis were based on two different donor materials, the poly(4,8-bis[(2-ethylhexyl)oxy]benzo[1,2-b:4,5-b′] dithiophene-2,6-diyl-alt-3-fluoro-2-[(2-ethylhexyl)carbonyl] thieno[3,4-b] thiophene-4,6-diyl) (PTB7) and the poly [[2,6′-4,8-di(5-ethylhexylthienyl) benzo[1,2-b;3,3-b] dithiophene] [3-fluoro-2[(2-ethylhexyl) carbonyl]thieno [3,4-b]thiophenediyl]] (PTB7-Th).

The PTB7 is a low band-gap polymer which exhibits a good photovoltaic effect resulting from the structural optimization of previously reported PTB-family polymers[65], synthetized by the Stille polycondensation[73] between the monomers 2,5-dibromothieno[3,4-b]thiophene and benzodithiophene distannane.[64] The PTB7 has a molecular weight (Mw) of 97.5 kDa with a polydispersity index (PDI) of 2.1. HOMO and LUMO energy levels are -5.15 eV and -3.31 eV, respectively. This polymer exhibits a hole mobility of about 5.8 x 10^{-4} cm^2 V^{-1} s^{-1}, and a strong absorption at the visible range from 550 to 750 nm.[63] The chemical structure of PTB7 is depicted on Figure 3.1a. On the other hand, PTB7-Th is synthetized by the reaction between the monomers 4,6-dibromo-3-fluoro thieno[3,4-b]thiophene-2-carboxylic acid-2-ethylhexyl ester and 1,1'-[4,8-bis[5-(2-ethylhexyl)-2-thienyl]benzo[1,2-b:4,5-b']dithio-phene-2,6-diyl]-bis[1,1,1-trimethyl]-Stannane. The Mw of

PTB7-Th is 125 kDa with a PDI of 2.7. PTB7-Th has a HOMO and LUMO energy levels of -5.22 eV and -3.63 eV, respectively, with an absorption onset at ~780 nm. The hole mobility of PTB7-Th (2.83×10^{-3} cm^2 V^{-1} s^{-1}) is higher than that of PTB7 polymer.[68,74] The chemical structure of PTB7-Th is shown in Figure 3.1b.

3.2.1.2 Electron acceptor material

The fullerene $PC_{70}BM$ was used as electron acceptor material in this thesis, due to its strong absorption in the visible range and good electron mobility, which results in a higher photon harvesting and charge transporting. Therefore, PSCs with $PC_{70}BM$ exhibit higher performance parameters than devices with other fullerenes, e.g. $PC_{60}BM$.[75] The $PC_{70}BM$ has a Mw of 1031 g mol^{-1}, and a HOMO and LUMO energy levels of -5.9 eV and -3.9 eV, respectively. The chemical structure of $PC_{70}BM$ is represented on Figure 3.1c.

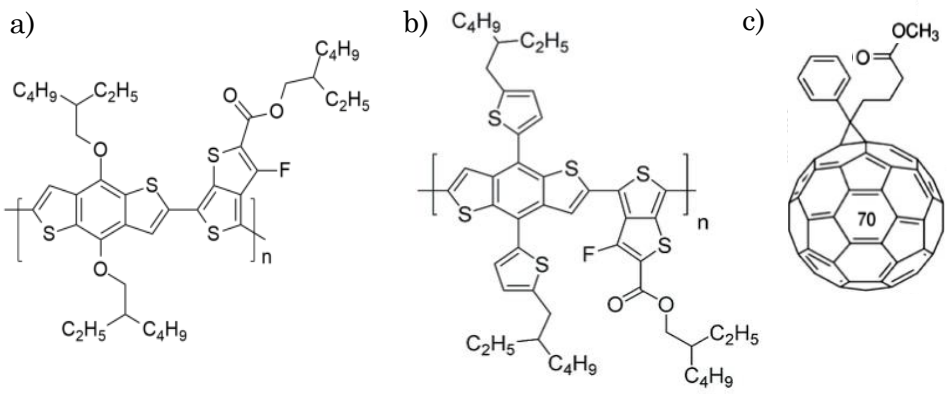

Figure 3.1 Chemical structure of electron donor materials PTB7 (a) and PTB7-Th (b), and electron acceptor material $PC_{70}BM$ (c) used in this thesis

3.2.2 Buffer layers

The buffer layers are placed between the active layer and the electrodes. These interlayers improve the energy-level alignment at the interface active layer/electrode, since they reduce the interface barrier formed by the direct contact of active layer and metal electrodes. The buffer layers work as selectively transport carrier layers to improve the charge collection and reduce the interfacial recombination. In this section, the materials used in this thesis as hole-transport layers with electron-blocking property, and electron-transport layers with hole-blocking property are described.

3.2.2.1 Electron transport layer (ETL) materials

The following materials were used as electron transport layer in the fabricated devices with conventional and inverted structures:

A) In conventional PSCs, calcium (Ca) is the most common low-work-function metal (-2.9 eV) used as cathode. However, it is well known that Ca can easily be oxidized in the presence of oxygen.[41] For this reason, Ca is covered by an additional Ag layer to protect it from oxygen residuals. Typically, a 25 nm thick Ca is evaporated on top of active layer under high vacuum conditions and serves as electron extracting interlayer.[76]

B) The poly[(9,9-bis(3'-(N,N-dimethylamino)propyl)-2,7-fluorene)-alt-2,7-(9,9–dioctylfluorene)] (PFN) is an alcohol/water soluble polymer synthesized by the palladium-catalysed Suzuki coupling reaction.[77] PFN can be used as ETL in inverted PSCs due to its highly efficient electron transporting/injection properties.[78] This

polymer exhibits a HOMO and LUMO energy levels of -5.6 eV and -2.1 eV, respectively. In iPSCs, a thin-film of PFN is deposited by spin-coating on top of ITO substrate, which results in the formation of a dipole on the ITO surface that reduce its work function from -4.7 eV to -4.1 eV.[43] Here, PFN was dissolved in methanol with a small amount of acetic acid and the PFN-solution was spin casted on top of ITO. Figure 3.2 shows the chemical structure of PFN.

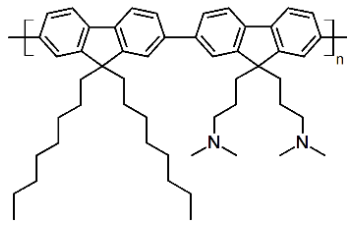

Figure 3.2 Chemical structure of PFN

C) Zinc oxide (ZnO) is one of the most common metal oxide used as ETL in iPSCs fabrication due to its high transparency, high air-stability and high electron mobility. Moreover, ZnO can be easily solution-processed on ITO substrates at room temperature by several coating methods, i.e. spin-coating[79], spray-coating[80] and inkjet printing.[81] In this thesis, several ZnO layers were deposited from different deposition techniques: thermal evaporation, inkjet printing and spin coating. For thermally evaporated-ZnO layer, ZnO nanopowder (< 100 nm particle size) was evaporated on top of ITO substrate under high vacuum conditions (1 x 10^{-6} mbar). On the other hand, ZnO nanoparticle ink (about 8-16 nm nanoparticle size) was inkjet printed on the top of ITO substrate using a piezoelectric inkjet printer. In the case of spin coating, a solution-

processed ZnO film was deposited on top of ITO substrate. The ZnO-solution was prepared by sol-gel process[82] dissolving the zinc precursor (zinc acetate dihydrate) in 2-metoxylethanol with ethanolamine as stabilizer.

D) Titanium oxide (TiO_x) has been widely investigated as ETL in iPSCs, because presents good transparency as thin films, high stability and high electron mobility.[83] TiO_x is used as an interlayer between the cathode and the active layer, because it can act as both an electron-collecting and hole-blocking layer. Moreover, it can also act as an optical spacer and redistribute the light intensity into the active layer to improve the exciton formation efficiency.[84-86] Here, TiO_x was deposited from a solution on top of ITO substrate by spin coating technique. The TiO_x-solution was prepared by sol-gel method, where titanium isopropoxide (Titanium-precursor) was dissolved in 2-methoxy-ethanol with ethanolamine as stabilizer.

3.2.2.2 Hole transport layer (HTL) materials

The two next materials were used as hole transport layer in the devices fabricated with conventional and inverted structures:

A) The poly(3,4-ethylenedioxythiophene)-poly(styrenesulfonate), well known as PEDOT:PSS, is a water-soluble polyelectrolyte with high transparency, high conductivity (~10 S cm^{-1}), and a work function of about -5.2 eV.[87,88] In conventional PSCs, PEDOT:PSS is used as HTL because of its aforementioned properties. Nevertheless, the hygroscopic and acidic nature of PEDOT:PSS are detrimental to

PSCs due to degrade the ITO electrode and active layer, which reduce the lifetime of devices.[89] Here, PEDOT:PSS was spin-cast onto the ITO substrate to fabricated conventional PSCs used as control devices. The chemical structure of PEDOT:PSS is depicted in Figure 3.3.

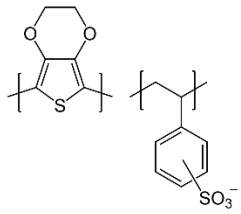

Figure 3.3 Chemical structure of PEDOT:PSS

B) Vanadium oxide (V_2O_5) is a transition metal oxide used to replace the PEDOT:PSS as HTL in PSCs, due to its high stability to ambient conditions. In this thesis, V_2O_5 was used as a hole-selective contact, since its high work function of (> 5 eV) laying close to the HOMO energy level of donor polymers, allows to form a good ohmic contact.[42,90] Here, an ultra-thin film (5 nm) of V_2O_5 was thermally evaporated under high vacuum conditions on top of the active layer to improve the hole collection.

3.3 Thin-film deposition techniques

Although there are several thin-film deposition techniques used to lab-scale based studies and large- scale fabrication, only the technologies for thin-film deposition used in this thesis are described. The spin coating, inkjet printing and thermal evaporation technologies were used for the fabrication of PSCs with conventional and inverted structures.

3.3.1 Spin coating

Spin coating is the standard method of thin-films deposition from a solution for lab-scale studies. This technique yields films with relatively high uniformity and well-controlled thickness. Nevertheless, spin-coating is not a compatible method with large-scale continuous process such as roll-to-roll (R2R) processing. In this spin coating, the solution-processed material is dropped on a rotating substrate, where the centrifugal forces spreads the solution on whole substrate surface and the volatile solvent is simultaneously evaporated due to the speed spinning.[91] The thickness of film is highly depend of the concentration and viscosity of solution, the volatility of solvent, and the angular speed of spinning.[92] In this thesis the active layers, TiO_x, ZnO, PFN and PEDOT:PSS layers were deposited by spin coating using the spin coaters (also called spinners) model WS-400B-6NPP/LITE and WS-650MZ-23NPP, both from Laurell Technologies Corporation. Figure 3.4 shows the spin coater machine (a) and the work principle of spin coating (b).

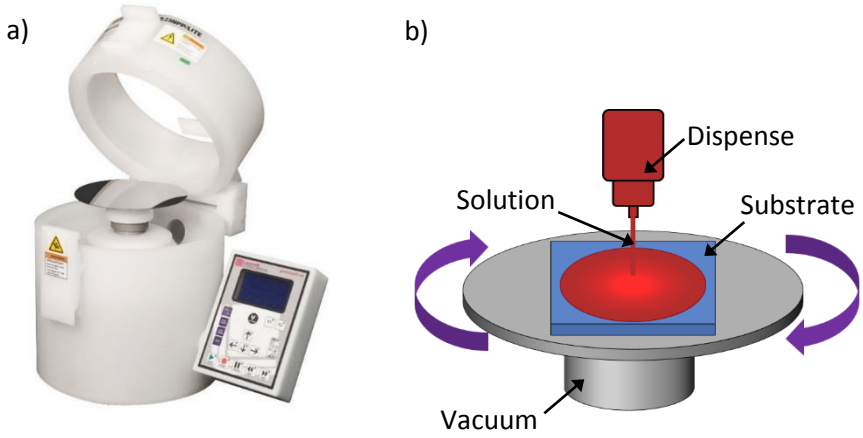

Figure 3.4 Spin coater machine from Laurell Technologies Corporation[93] (a); Work principle of spin coating (b)

3.3.2 Inkjet printing

Inkjet printing (IJP) is a very promising technique for the large-scale production of PSCs and commercialization due to its compatibility with R2R process and the reduction of material wasting. IJP is an anisotropic deposition process that allows patterning without any chemical processes (i.e. wet etching of photoresist). This technique allows avoiding the use of masks and lithography steps in patterning applications, which reduce the process cost. In inkjet printing, a fixed quantity of ink, in the form of a droplet, is ejected from a nozzle by a piezoelectric action. To do so, a voltage is applied to the piezo-injector to induce a pressure pulse and contract the chamber, filled with ink, and overcome the threshold pressure at the nozzle to eject a drop.[94] The thickness and resolution of the film are dependent of the printing speed, surface tension and viscosity of the ink, the spreading distance and the overlapping of drops on the substrate surface, and on the applied voltage. This technique has already been used for the manufacture of organic electronics devices.[95-97] Here, ZnO layers were deposited by IJP using a Fujifilm DIMATIX DMP-2800 printer with 16 nozzles at 254 µm. Figure 3.5 shows the printer[98] (a) and the working principle of IJP (b).

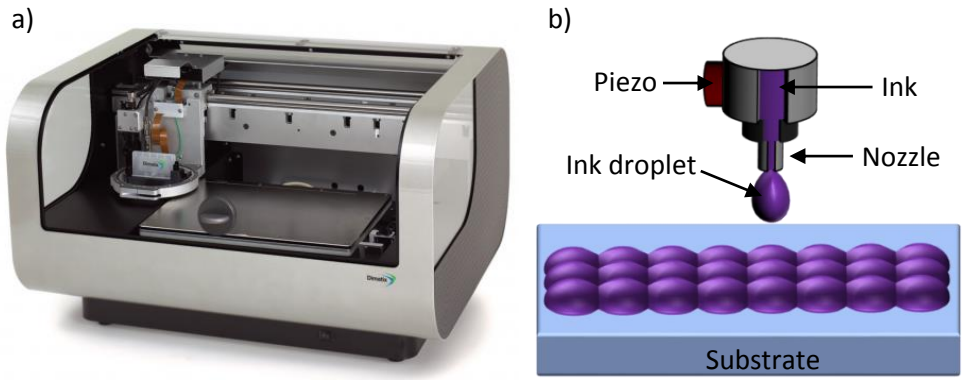

Figure 3.5 DIMATIX DMP-2800 printer (a); Working principle of inkjet printing (b)

3.3.3 Thermal evaporation

Thermal evaporation technique is a vacuum technology for thin-films deposition of pure solid materials such as metals, non-metals, oxides, nitrides, and organic materials. In thermal evaporation, a high-current flow through a resistive evaporation source (so-called filament or boat) made of metals, commonly tungsten or molybdenum.[99] The evaporation source is located at the bottom of vacuum chamber, whereas the target (substrate) is held inverted on the top. The materials are heated to overcome their melting point and form a vapour stream, which is deposited on the surface of substrate. To do so, the evaporated particles in the vacuum chamber must reach the substrate. In this thesis, the ZnO, V_2O_5 and Ag layers were thermally evaporated under high vacuum by an evaporator located in a Glove-box, model MB20/MB200 from MBRAUN. The schema of the evaporator machine from MBRAUN and the working principle of thermal evaporation are depicted on Figure 3.6.

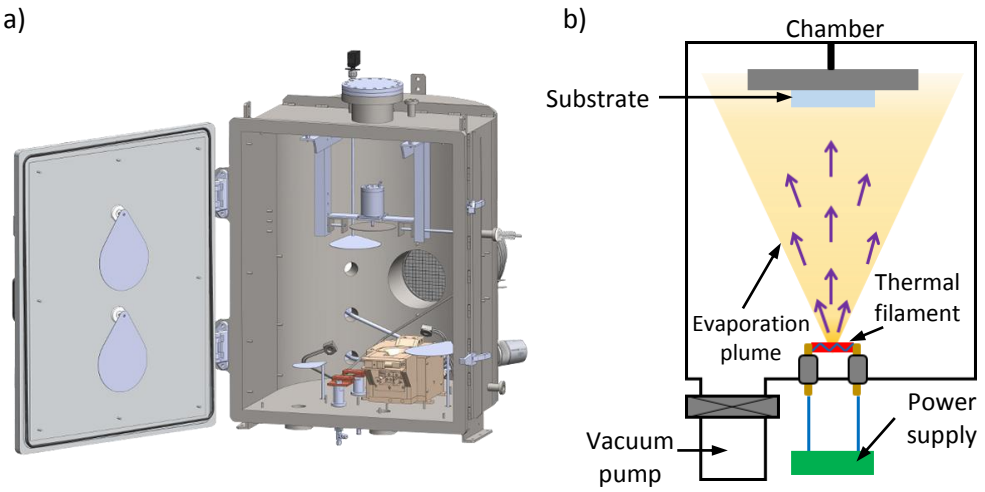

Figure 3.6 Schema of evaporator chamber from MBRAUN (a); Working principle of thermal evaporation (b)

3.4 Fabrication process

3.4.1 ITO substrate cleaning

All the polymer solar cells with conventional and inverted structure were fabricated on patterned ITO-coated glass substrates with nominal sheet resistance of 10 Ω sq^{-1}, purchased from PsiOTec Ltd. ITO substrates were cleaned using a surface-active cleaning agent diluted in deionized water. Then, the substrates were rinsed with deionized water and blow dried with high purity nitrogen gas. Subsequently, ITOs were sonicated in acetone, methanol and isopropanol anhydrous solvents for 10 min each, after which they were dried at 120 ºC in an oven for 20 min and transferred to UV/ozone cleaning for 15 min to eliminate the organic materials from their surface.

3.4.2 Interlayer deposition on ITO substrate

Since the analysed PSCs in this thesis were fabricated with an inverted structure, the electron transport layer was deposited on top of ITO substrate. As aforementioned, here several materials were used as ETL. The deposition parameters of materials used as ETL are described below.

3.4.2.1 Titanium oxide

TiO_x layers were deposited from a solution via spin coating. The TiO_x-solution was prepared by sol-gel method. The starting materials were 2 mL of titanium isopropoxide (99.999 % purity), 10 ml of 2-methoxyethanol (99.9 % purity) and 1 mL of ethanolamine (99 % purity). All these materials were acquired from Sigma-Aldrich. The reagents were mixed in a hermetically amber glass vial inside a glove box. The mixture

was stirred for 3 h at 120 ºC to obtain a clear solution. Then, the TiO_x-solution was diluted in methanol (anhydrous, 99.8 %) from Sigma-Aldrich with a volume ratio of 1:6, respectively. The diluted solution was stirred for 1 h. All reactions were carried out under dry nitrogen. The diluted TiO_x-solution was filtered through 0.2 μm PTFE filter. Subsequently, 100 μL of TiO_x-solution were spin coated on top of ITO-substrates at 6000 rpm for 45 s under nitrogen atmosphere in order to obtain a TiO_x layer 15 nm thick. In order to convert the precursor in TiO_x by hydrolysis, samples were left in ambient conditions for 1 h and heated at 400 ºC. The temperature was increased with heating rate of 20 ºC min^{-1}.

3.4.2.2 Zinc Oxide

In this thesis, ZnO layers were deposited by three different coating techniques, spin coating, inkjet printing and thermal evaporation.

A) ZnO was deposited by spin coating from a solution using sol-gel method. ZnO-solution was prepared by dissolving 4.5 g of zinc acetate dihydrate (99 % purity) in 30 mL of 2-methoxyethanol (99.9 % purity) and 1 mL of ethanolamine (99 % purity). All materials were acquired from Sigma-Aldrich. The reagents were mixed in a hermetically amber glass vial inside a glove box. The mixture was vigorously stirred during 1 h at 70 ºC to obtain a clear solution. This solution was diluted in anhydrous methanol from Sigma-Aldrich with a volume ratio of 1:1, respectively. The diluted ZnO-solution was filtered through a 0.2μm PTFE filter. Subsequently, 100 μL of ZnO-solution were spin coated on top of ITO-substrates at 3000 rpm for 30 s under ambient conditions. The resulting ZnO films were heated at 110 ºC for 1 h in air. The final thickness of the ZnO layers was about 45 nm.

B) ZnO nanoparticle ink (crystalline ZnO dispersed in isopropanol and propylene glycol, 2.5 wt%) purchased from Sigma-Aldrich was used for ZnO deposition by inkjet printing. The ZnO-ink, with a viscosity of about 8-14 cp and nanoparticle size around 8-16 nm, was sonicated during 10 min and was filtered through 0.2 μm PTFE filter. The ZnO-ink was deposited on patterned ITO-coated glass substrate, using a DIMATIX DMP-2800 printer. The printing parameters are as follows: drop spacing of 10 μm, drop velocity of 8 m/s, 15 nozzles at 16V and jetting frequency of 5 kHz. Subsequently, the samples were heated at 115°C during 10 min in air into a conventional oven. The final thickness final thickness of the ZnO layers was about 45 nm.

C) For thermal evaporation, ITO substrates were transferred to a vacuum chamber, where 45 nm of ZnO nanopowder (<100 nm particle size, acquired from Sigma-Aldrich) were thermally evaporated under high vacuum conditions ($9x10^{-7}$ mbar). The evaporation rate ranged from 0.01 to 0.03 nm s^{-1}.

3.4.2.3 PFN

The PFN was deposited by spin coating from a solution. The PFN solution was prepared by dissolving 5.5 mg of PFN (from 1-material) in 3 mL of methanol (anhydrous 99.8 %, from Sigma-Aldrich) and 6 μL of glacial acetic acid (≥99.85 % from Sigma-Aldrich) under nitrogen atmosphere. The PFN solution was stirred and heated at 40 ºC for 18 h. The solution was filtered through a 0.2 μm PTFE filter. Afterwards, 70 μL of this solution were spin-cast on top of the pre-cleaned ITO substrate at

3500 rpm, under inert atmosphere, to obtain a thickness of 10 nm. The resulting layers were dried in the vacuum chamber for 2 h.

3.4.2.4 PEDOT:PSS

In conventional PSCs, the hole transport layer is deposited on ITO substrates. Here, PEDOT:PSS was used as interlayer to improve the hole collection by the ITO. PEDOT:PPS (Clevios P VP.AL 4083) was acquired from Heraeus Group. To form a uniform layer of about 30 nm, PEDOT:PSS was filtered through a 0.2 μm PTFE filter. 100 μL were deposited by spin coating, under ambient conditions, at 3500 rpm for 45 s. The resulting layers were annealed at 110 ºC for 20 min.

3.4.3 Active layer deposition

The active layer was deposited on the top of the previously deposited layer, i.e. in iPSCs the active layer was deposited on top of ETL, whereas it was deposited on top of HTL for conventional PSCs. Here, the active layers of the fabricate PSCs were based on PTB7:$PC_{70}BM$ and PTB7-Th:$PC_{70}BM$ (see section 3.2.1). The electron donor polymers, PTB7 and PTB7-Th, were purchased from 1-material, while the fullerene $PC_{70}BM$ was acquired from Ossila. The PTB7:$PC_{70}BM$ blend solution was prepared by dissolving PTB7 and $PC_{70}BM$ (1:1.5 w/w) in chlorobenzene (anhydrous 99.8 %, from Sigma-Aldrich) and 1,8-diiodooctane (97 % stabilized with copper, from Alfa Aesar), with a volume ratio of 97:3. The final concentration of PTB7:$PC_{70}BM$-solution was 25 mg mL^{-1}. The solution was left stirring and heated at 40 ºC overnight. Further, the blend-solution was aged for 48h in the dark in order to improve the active layer morphology. After ageing time, the blend solution was filtered through a 0.2 μm PTFE filter. 70 μL of the solution were spin-coated on

top of the interlayer (ETL o HTL, depending on the devices architecture), at 800 rpm for 30 s, to obtain an active layer 100 nm-thick. The PTB7-Th:$PC_{70}BM$ layer was deposited with the same parameters as the PTB7:$PC_{70}BM$ layer deposition (i.e. same solvents, solution concentration, ageing time, and spin speed). All the process steps for active layer deposition (PTB7:$PC_{70}BM$ and PTB7-Th:$PC_{70}BM$) were carried out under nitrogen atmosphere.

3.4.4 Deposition of top interlayer and electrode

Since the top interlayer and electrode are deposited by thermal evaporation, both layers were evaporated together in a vacuum chamber on top of the active layer. For iPSCs, 5 nm of V_2O_5 (from Sigma-Aldrich) were evaporated on top of active layer through a shadow mask with an evaporation rate of ~0.01 nm s^{-1}. Subsequently, 100 nm of Ag (high-purity 99.99% silver wires purchased from Testbourne Ltd.) were evaporated with an evaporation rate, ranging from 0.01 to 0.05 nm s^{-1}. The V_2O_5 acts as the hole transport interlayer and Ag as the cathode. On the other hand, for conventional PSCs, Ca was used as electron transport interlayer and Ag as the anode. In these devices, 25 nm of Ca (99.99% purity calcium pellets were purchased from Kurt J. Lesker) were evaporated on top of the active layer, through a shadow mask, with an evaporation ratio from 0.1 to 0.2 nm s^{-1}. Subsequently, 100 nm of Ag were evaporated with an evaporation rate ranging from 0.01 to 0.05 nm s^{-1}. All the thermal evaporations were carried out under high vacuum conditions ($\leq 1 \times 10^{-6}$ mbar). The effective area for all devices was 0.09 cm^2, which is defined by the overlapping area between the cathode and anode. Figure 3.7 shows the process sequence for iPSCs fabrication.

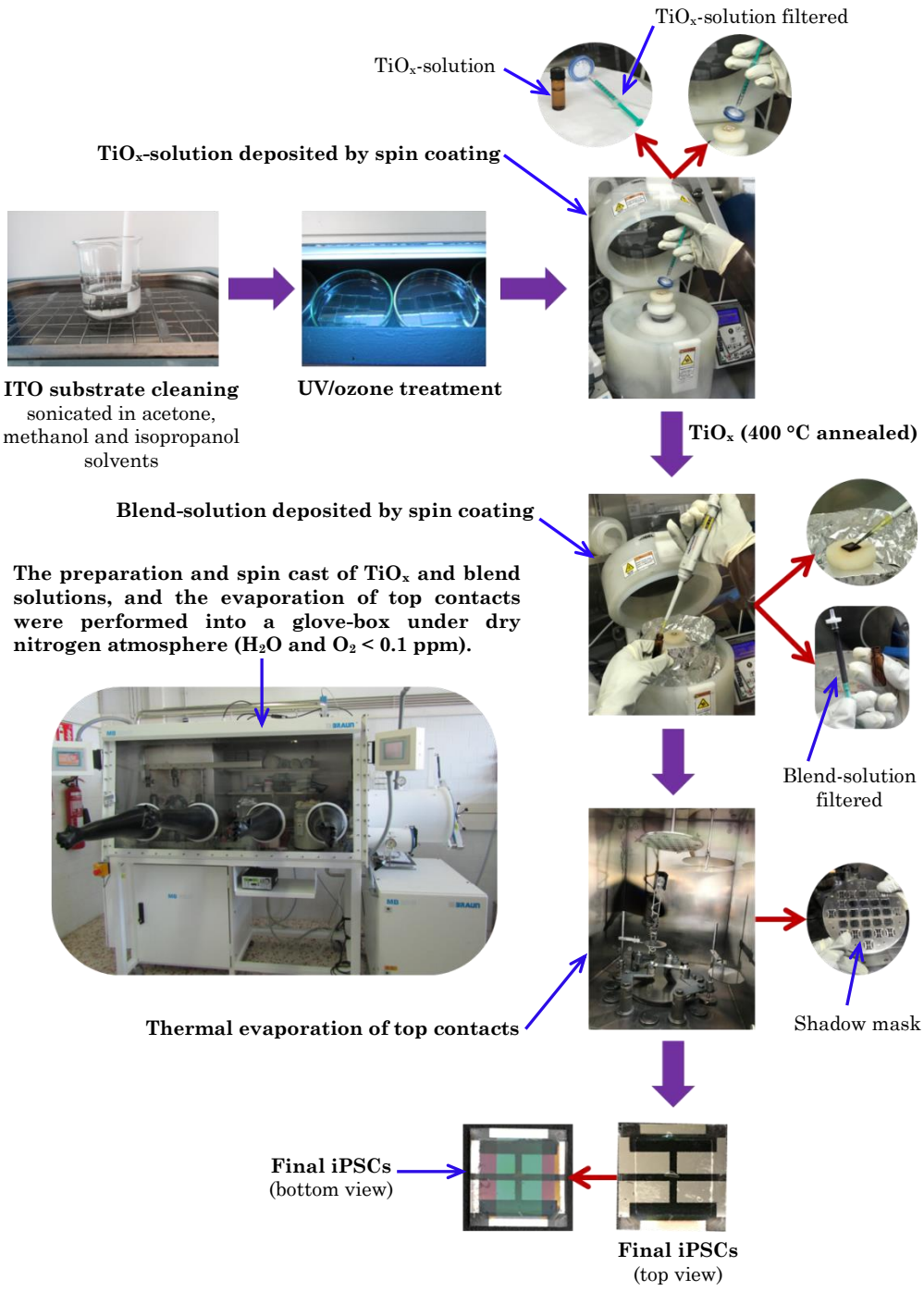

Figure 3.7 Step-by-step process for iPSCs fabrication

3.5 Devices characterization

All the characterization measurements were carried out under nitrogen conditions (H_2O < 0.1 ppm and O_2 < 0.1 ppm), excluding some characterization measurements for degradation analysis performed under environmental conditions. Since all the characterization systems work under environmental conditions, the samples were set in a sealed samples-holder (from Ikerlan) under nitrogen condition into the glove-box. For degradation analysis measurements, samples were set in the samples-holder under environmental conditions. Figure 3.8 shows the samples-holder used for devices characterization measurements.

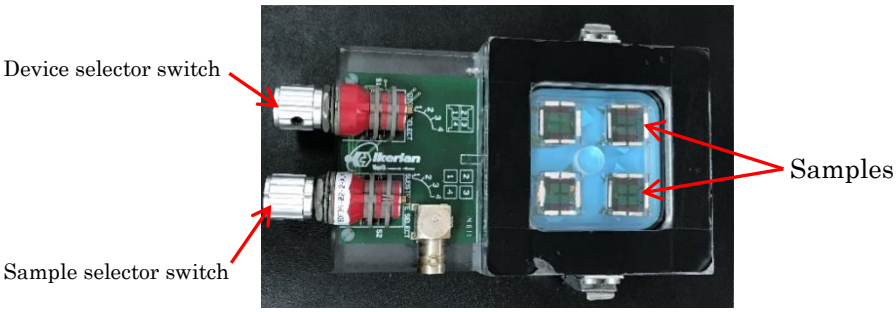

Figure 3.8 Samples-holder used for the transporting and characterization measurements of devices

3.5.1 Photovoltaics measurements

The electrical properties of PSCs fabricated in this thesis were characterized by current-density vs. voltage (*J-V*) measurements in dark and under illumination. All *J–V* characteristics were performed at room temperature. The *J-V* measurements under illumination were carried out with a solar simulator (Abet Technologies model 11000 class type A, Xenon arc) and a Keithley 2400 Source-Measure Unit. The light intensity

was calibrated by a NREL certified monocrystalline silicon photodiode. All the *J–V* measurements were taken under forward voltage sweep direction from -1 V to 1 V. The experimental setup for *J-V* measurements is shown in Figure 3.9.

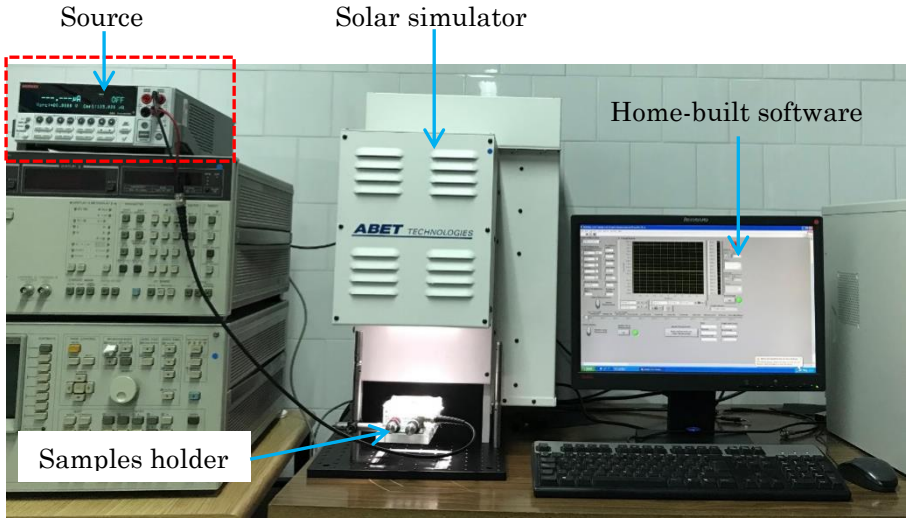

Figure 3.9 Experimental setup for current density-voltage (*J-V)* measurements

3.5.2 External quantum efficiency

The external quantum efficiency (EQE) is defined as the ratio of the number of incident photons to the number of charge carriers extracted by the solar cell. The EQE depends on the light absorption, the charge carriers' transport, and the trapping and recombination of charge carriers. Here, the EQE was measured using a homemade set up, consisting of a 150 W Oriel Xenon lamp, a motorized monochromator and a Keithley 2400 digital source meter. The photocurrent and irradiated light intensity were measured simultaneously and processed with a home-built Labview© software. All the EQE measurements were carried out under forward wavelength sweep direction from 300 nm to 800 nm. The experimental setup for EQE measurements is shown in Figure 3.10.

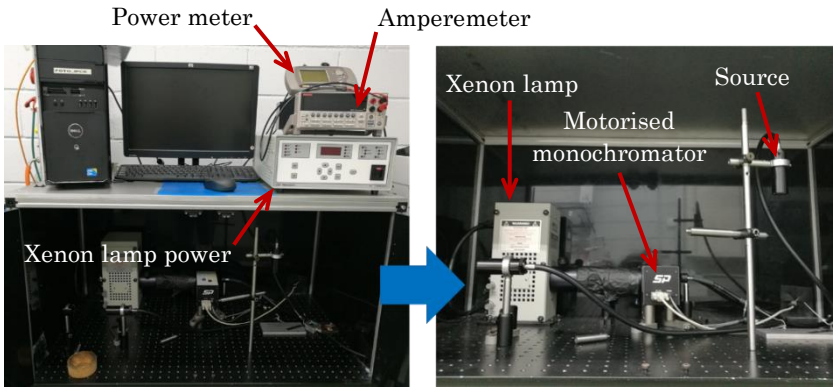

Figure 3.10 Experimental setup for EQE measurements

3.5.3 Photophysical measurements

The charge carrier recombination kinetics analysis was performed, to obtain more insight on how the band structure affects the *J-V* characteristics of the devices. To do so, charge extraction and transient photovoltage measurement (CE/TPV) were done. The charge extractions measurements were carried out in open circuit voltage equilibrium by illuminating the devices, using a white light LED ring from LUXEON® Lumileds. Devices are connected to a DC power supply and a function generator TGP110. The light is turned off and the circuit closed to force the charge to pass through an oscilloscope TDS 2022 from Tektronix. In this step, the drop-in voltage across a resistance of 50 ohms is recorded by the oscilloscope. The recorded voltages by the oscilloscope can be converted to the amount of charge by the equation (3.1).

$$Q(C) = \frac{1}{R}\int_{t=0}^{t=t} V(t)dt \qquad (3.1)$$

where *Q(C)* is the accumulated charge, *R* is the 50 ohm resistance and *V(t)* is the recorded voltage by the oscilloscope at each time. In CE

measurements, electron density (e^- cm^{-3}) defines the *Q(C)* in the bulk, since it depends on the volume of active layer. The electron density is defined by the exponential distribution on the form of equation (3.2).

$$e^-_{density}(V) = A_0 + A_1 \cdot e^{(V/m_c)} \tag{3.2}$$

where A_0 and A_1 are constants and m_c is the energy that describes the curvature distribution.

In TPV measurements, the background illumination was provided by a ring with 6 white LED's from LUXEON®, while samples are connected to 1 MΩ input terminal of an oscilloscope Tektronix© TDS2022. A small perturbation was applied by a light pulse excited at 650 nm (PTI GL-3300 Nitrogen Laser, <100 ns pulses), with a range intensity from 0.1 sun to 1 sun. The excess charge generated recombines, since the device is being held at open-circuit condition. The transient decay of the charge carriers is recorded by the oscilloscope. The data from TPV measurements follows a single exponential decay of the form of equation (3.3).

$$V(t) = V_0 + V_1 \cdot e^{-(t/\tau)} \tag{3.3}$$

where V_0 is the open circuit voltage (V), V_1 is the voltage amplitude generated (V) by the pulse, and τ is the recombination mean lifetime (s). Figure 3.11 shows the schematic diagram for charge extraction (a) and for transient photovoltage (b) measurements. Figure 3.12 shows the experimental setup for charge extraction (a) and for transient photovoltage (b) measurements.

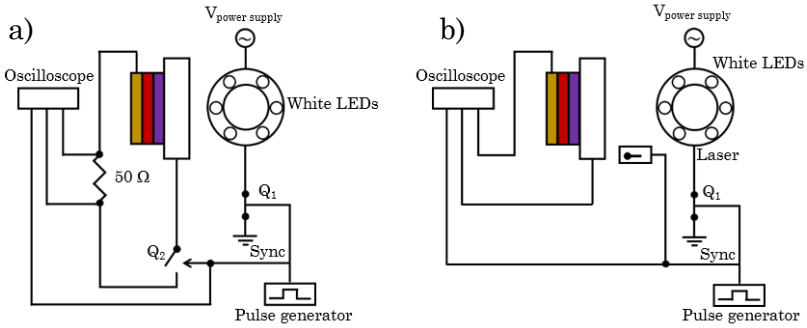

Figure 3.11 Schematic diagram for charge extraction (a) and transient photovoltage (b) measurements

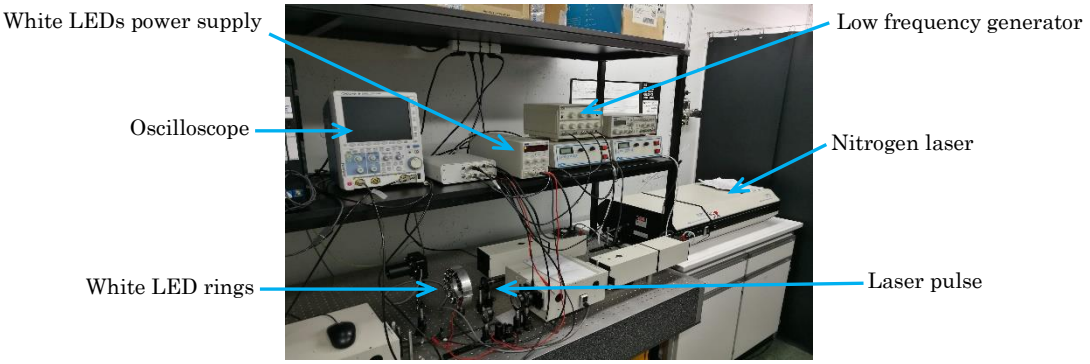

Figure 3.12 Experimental setup for charge extraction and transient photovoltage measurements

3.5.4 Impedance spectroscopy measurements

Impedance spectroscopy (IS) is one of the most frequent technique used to study the losses and carrier transport mechanisms involved on the charge extraction in PSCs. Here, IS measurement were used to distinguish the loss mechanisms, which take place at the active-layer/HTL and active-layer/ETL interfaces. Impedance spectroscopy measurements were performed using a HP-4192A impedance analyser. Several voltage perturbations were applied at frequency range from 1 kHz to 1 MHz with an AC signal and 15 mV amplitude. The IS measurements

were carried out in dark and under AM1.5 illumination calibrated by a certified monocrystalline silicon photodiode. IS measurements were performed with a frequency sweep from 5 Hz to 1 MHz. Figure 3.13 shows the experimental setup for IS measurements under AM1.5 illumination.

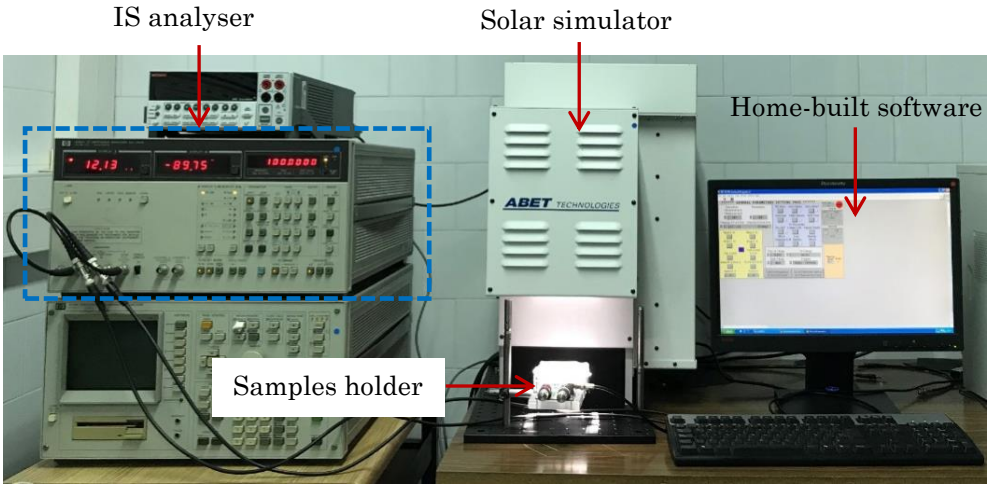

Figure 3.13 Experimental setup for impedance spectroscopy measurements

3.5.5 UV-Vis spectroscopy analysis

The UV-Vis spectroscopy was used to obtain the reflection (%R) and transmittance (%T) spectra of monolayers (e.g. active layer or buffer layer) and bilayers (e.g. layer/buffer layer). The %R and %T spectra were recorded on a Perkin Elmer UV-Visible-NIR Lambda 950 spectrophotometer using an integrator sphere. The absorbance of monolayers and bilayers were calculated by the equation (3.4).

$$1 = \rho + \tau + \alpha \tag{3.4}$$

by Kirchoff's radiation law, where ρ is the reflectance, τ the transmittance and α the absorbance.

Figure 3.14 shows the UV-Vis spectrophotometer used for the UV-Vis spectroscopy analysis.

Figure 3.14 Experimental setup for UV-Vis spectroscopy analysis

3.5.6 Atomic Force Microscopy measurements

Atomic Force Microscopy (AFM) measurements were used to analyse the morphology of layers deposited by different techniques. AFM measurements were performed in tapping mode on a Molecular Imaging model Pico SPM II (pico +). Images were collected, in air using silicon probes, with typical spring constant of 1–5 nN/m and at resonant frequency of 75 kHz.

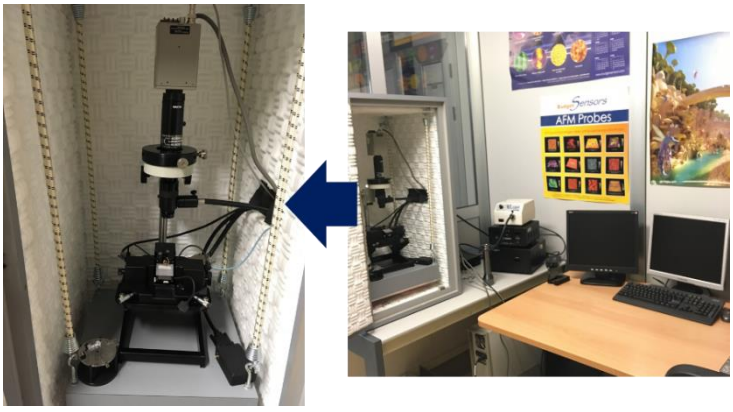

Figure 3.15 Experimental setup for atomic force microscopy measurements

Chapter 4

Stability and degradation analysis of iPSCs with TiO_x as ETL

4.1 Introduction

Nowadays, the PSCs must exhibit high efficiency, long lifetime, low-cost fabrication, and environmentally friendly qualities for their large-scale commercialization. Among these, the lifetime of PSCs is linked to both intrinsic and extrinsic stability. The intrinsic stability for a PSCs is related to the intrinsic properties of organic materials e.g. morphology, disorder, defect density, trap concentration.[100,101] The extrinsic stability for PSCs is associated to the electrodes corrosion and active layer oxidation driven by external agents such as oxygen, water, light, or heat. [76,102,103] A good example of extrinsic instability for conventional PSCs is the oxidation of the calcium/Aluminium cathode by the environmental oxygen, as well as the degradation of the ITO and active layer due to the hygroscopic and acid nature of PEDOT:PSS.[41,89] Some of the strategies used to improve the stability of PSCs include an accurate selection of donor and acceptor materials, modifying the arrangement of stacked-layers, changing the contact electrodes, and using hermetic encapsulations to reduce the degradation of metal electrodes and organic materials.[104-106] Based on the aforementioned, PSCs with an inverted architecture (iPSCs) have been developed. In iPSCs, PEDOT:PSS is commonly replaced by MoO_3, V_2O_5 or NiO as the hole transport layer (HTL) because their high work-functions (>5 eV) provide low resistance ohmic contacts.[42,107] Ca is also largely replaced by PFN, ZnO or TiO_x as the ETL. These materials modify the ITO's surface and improve the charge carrier extraction.[43,105,108] Several reports have demonstrated that efficiency and stability of iPSCs can be improved using V_2O_5 as HTL and TiO_x as ETL.[109-112] TiO_x has been widely investigated because presents good transparency as thin films, high stability and high

electron mobility. In iPSCs, TiO_x is used as an interlayer between the cathode and the active layer because it can act as both an electron-collecting and hole-blocking layer. It can also act as an optical spacer and redistribute the light intensity into the active layer to improve the exciton formation efficiency.[84-86]

In this chapter, the stability and degradation of conventional and inverted PSCs based on PTB7:$PC_{70}BM$ as the active layer are analysed. The conventional PSCs were fabricated with the architecture ITO/PEDOT:PSS/PTB7:$PC_{70}BM$/Ca/Silver (Ag), where ITO/PEDOT:PSS and Ca/Ag were used as the anode and cathode, respectively. The iPSCs were fabricated using the architecture ITO/TiO_x/PTB7:$PC_{70}BM$/V_2O_5/Ag, (TiO_x-iPSCs) where V_2O_5/Ag were used as anode and ITO/TiO_x were used cathode. In addition, for comparison purposes, a third set of inverted devices with the same architecture using PFN instead of TiO_x was fabricated (PFN-iPSCs). Figure 4.1 shows the inverted and conventional architectures (a), the chemical structure of photoactive materials used in PSCs. as well as, the energy level of TiO_x-iPSCs (b), PFN-iPSCs (c) and conventional (d) PSCs. Note that a dipole is formed on the ITO surface after the deposition of 10 nm of PFN, which reduces the work function of ITO from -4.7 eV to -4.1 eV.[43,103,108,113] In order to analyse the stability of TiO_x-iPSCs, their PCEs were compared with those of PFN-iPSCs and conventional PSCs over time under nitrogen. For a better long-term stability and degradation analysis of PSCs, the performance parameters of several samples were measured over time under three conditions: dry nitrogen, non-encapsulated and encapsulated in accordance with ISOS) D-1 protocols.[114,115] Moreover, electron mobility was calculated by the Mott-Gurney space-charge-limited current *(SCLC)* equation for samples

under the three conditions at different times. Finally, impedance spectroscopy measurements were carried out to analyse the degradation of encapsulated and non-encapsulated TiO_x-iPSCs.

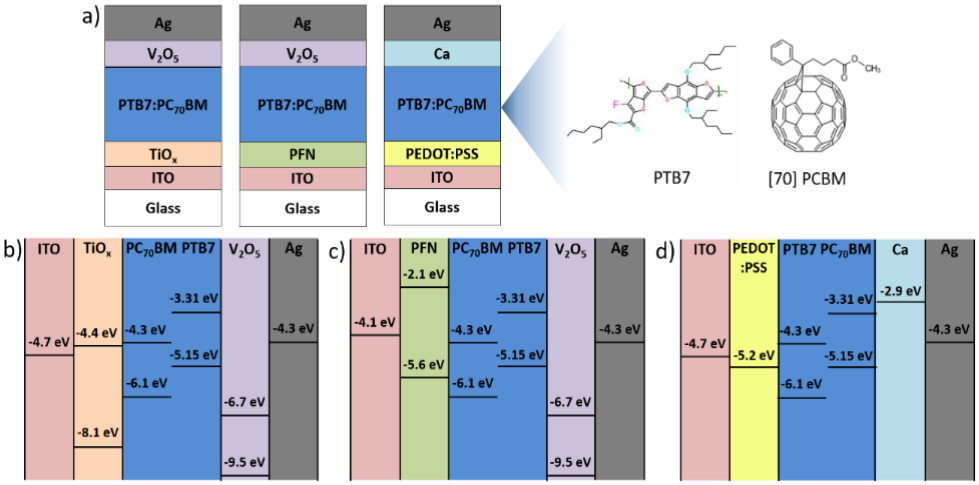

Figure 4.1 Inverted and conventional structures of fabricated BHJ-PSCs and the chemical structure of photoactive materials (a). Energy band diagram of iPSCs with TiO_x as ETL (b), PFN as ETL (c) and conventional PSCs (d)

4.2 Experimental details

4.2.1 TiO_x, PFN and blend solutions preparation

The TiO_x solution was prepared via sol-gel methods as follows[113]: The starting reagents were titanium (IV) isopropoxide ($Ti[OCH(CH_3)_2]_4$, 2mL), 2-methoxyethanol ($CH_3OCH_2CH_2OH$, 10mL) and ethanolamine ($H_2NCH_2CH_2OH$, 1mL). The reagents were stirred for 3 hours at 120ºC to obtain a clear solution. The clear solution was diluted in anhydrous methanol with a volume ratio of 1:6, respectively. The diluted solution was stirred for 1 hour. All reactions were carried out under dry nitrogen.

To prepare a solution with a concentration of 2 mg mL^{-1}, PFN powder was dissolved in methanol and a small amount of acetic acid (2 µl mL^{-1}). The PFN solution was stirred and heated at 40ºC overnight.

The blended solution was prepared by dissolving PTB7 and $PC_{70}BM$ with a weight ratio of 1:1.5 in chlorobenzene (CB) and 1,8-diiodooctane (DIO) (97:3 v/v) to obtain a solution concentration of 25 mg mL^{-1}. The blend solution was stirred and heated at 40ºC overnight.

4.2.2 Device fabrication

Inverted PSC with a thin-film TiO_x as ETL were fabricated on ITO-coated glass substrates previously cleaned with detergent, and ultra-sonicated in acetone, methanol and isopropanol. Subsequently, ITO substrates were dried in an oven at 120°C for 20 min and transferred to UV/ozone cleaning for 15 min to eliminate the organic materials from their surface. Diluted TiO_x-precursor was spin-cast in air on top of the ITO substrates at 6000 rpm. In order to convert the precursor in TiO_x by hydrolysis, samples were left in ambient conditions for 1 hour and heated at 400°C. The final temperature was reached by increasing the temperature at a heating rate of 20°C min^{-1}. The final thickness of the TiO_x layer was about 15 nm (see Figure 4.2). Subsequently, a blended solution of PTB7:$PC_{70}BM$ was deposited on top of the TiO_x layer by spin coating at 800 rpm for 30 s, to obtain an active layer with a thickness of about 100 nm.

Finally, 5 nm of V_2O_5 and 100 nm of Ag were thermally evaporated onto the photoactive layer in a vacuum chamber. The PFN-iPSCs were fabricated by replacing only TiO_x by PFN as ETL. The PFN solution was

spin-cast on top of the pre-cleaned ITO substrate at 3500 rpm, to obtain a thickness of 10 nm. In addition, a third set of conventional PSCs were fabricated using PEDOT:PSS and Ca as HTL and ETL, respectively. PEDOT:PSS was deposited on top of the ITO layer by spin-coating at 4500 rpm and annealed at 120°C for 20 min. Afterwards, 25 nm of calcium were thermally evaporated on the photoactive layer in a vacuum chamber. In all cases, the effective device area of the sample was 0.09 cm^2. The devices were encapsulated under nitrogen with a UV-curing liquid acrylic adhesive.

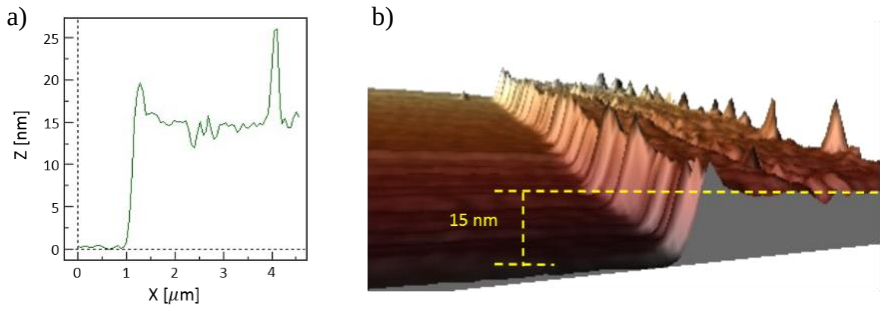

Figure 4.2 Thickness measurement of TiO_x by AFM scanning: Profile (a) and 3D rendering (b)

4.3 Results and discussion

4.3.1 Electrical characterization

The current density-voltage (*J-V*) characteristics of conventional and inverted PSC were measured in dark and under simulated AM1.5G illumination (100 mW cm^{-2}). Figure 4.3 shows best *J-V* characteristics of conventional PSCs, TiO_x-iPSCs and PFN-iPSCs measured in dark (a) and under simulated AM1.5G illumination (b). From Figure 4.3b, the short circuit current density (J_{SC}) improves significantly in both TiO_x-iPSCs and PFN-iPSCs. Moreover, the open circuit voltage (V_{OC}) of TiO_x-iPSCs is as

good as conventional PSCs and higher than PFN-iPSCs. Table 4.1 summarizes the average and standard deviation of performance parameters of conventional PSCs, TiO_x-iPSCs and PFN-iPSCs: *Voc*, *Jsc*, fill factor (FF), power conversion efficiency (PCE) and both series and shunt resistances (R_S and R_{Sh}). The average and standard deviation were calculated over ten devices. All the *J-V* measurements were carried out under light and nitrogen conditions (O_2 < 0.1 ppm and H_20 < 0.1 ppm). The best PCE of devices is also shown in Table 4.1.

TiO_x-iPSCs showed the highest J_{SC} and PCE (8.43 %), and the lowest FF. These devices exhibit higher R_S and R_{Sh} than those of PFN-iPSCs, but lower than those of conventional PSCs. Meanwhile, PFN-iPSCs showed higher PCE (7.7%) than conventional PSCs (7.57%) and the lowest R_S and R_{Sh}. Conventional PSCs showed higher V_{OC} and FF than TiO_x- iPSCs.

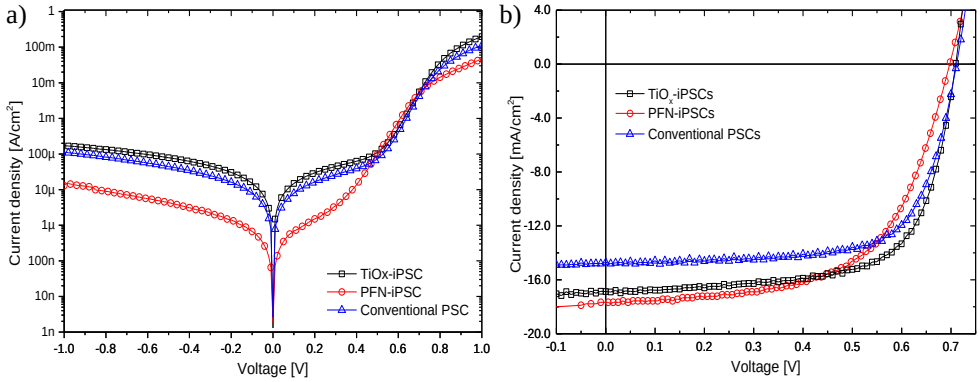

Figure 4.3 Current density-voltage characteristics of TiO_x-iPSCs (black squares), PFN-iPSCs (red circles) and conventional PSCs (blue triangles), based on PTB7-$PC_{70}BM$ in dark (a) and under AM 1.5G irradiation (b)

Table 4.1 Performance of conventional and inverted PSCs under AM1.5

Devices	V_{OC} [mV]	J_{SC} [mA cm^{-2}]	FF [%]	PCE [%]		R_S [Ω cm^2]	R_{Sh} [Ω cm^2]
				Best	Average		
TiO_x-iPSCs	705±5	16.44±0.45	67.45±1.19	8.43	8.25±0.16	0.85±0.02	532±150
PFN-iPSCs	694±6	17.28±0.46	68.33±1.73	8.08	7.71±0.32	0.55±0.07	320±177
Conventional	704±5	14.59±0.19	69.85±0.85	7.57	7.43±0.07	1.47±0.02	1050±330

4.3.2 Intrinsic stability analysis

Since the intrinsic stability of PSCs is linked to the intrinsic properties of materials, the devices must be characterized under nitrogen conditions in a well-packed holder to minimize the external agents' effects. The intrinsic stability of fabricated devices was analysed by measuring their PCE overtime under light and nitrogen conditions (O_2 < 0.1 ppm and H_20 < 0.1 ppm). Figure 4.4 shows the PCE behaviour over time of three PTB7:$PC_{70}BM$-based fabricated solar cells under nitrogen conditions. The PCEs of PFNs and TiO_x-iPSCs were very similar until 214h of storage (nearly 90% of the original PCE).

Nevertheless, TiO_x-iPSCs show the best PCE intrinsic stability over time and maintain 80% of their original PCE after 6048h stored under nitrogen conditions. It has been previously reported that iOSCs stability can be improved by using a TiO_x layer.[116-118] The TiO_x layer reduces the photo-degradation of the active layer since it can act as UV filter. Moreover, TiO_x is also used as scavenging layer in order to prevent the intrusion of oxygen and water into the active layer.[84,119] PFN-iPSC and conventional PSCs reduced it PCE to 80 %, after 1300h and 1200h, respectively.

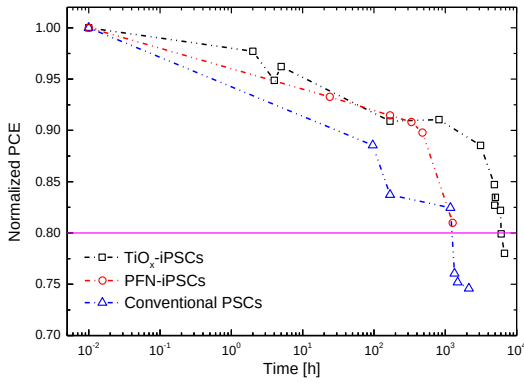

Figure 4.4 Stability of power conversion efficiency over time under nitrogen for TiO_x-iPSCs (black squares), PFN-iPSCs and conventional PSC (blue triangles)

4.3.3 Extrinsic stability analysis

Since TiO_x-iPSCs showed good performance characteristics and good intrinsic stability over time, these devices were used to study the extrinsic stability of iPSCs based on PTB7:$PC_{70}MB$ under different conditions. Encapsulated and non-encapsulated iPSCs were exposed to ambient conditions (23 ±2ºC and 45 ±5 %RH, ISOS D-1 protocols). For a better analysis, the stability of these devices was compared with TiO_x-iPSCs stored under nitrogen. Figure 4.5 shows the *J-V* characteristics of TiO_x-iPSCs under three different conditions (encapsulated, non-encapsulated and nitrogen) measured under simulated AM 1.5G illumination. Figure 4.5a shows that after 72 h of exposure to ambient conditions, the encapsulated devices slightly reduced J_{SC} and V_{OC}. Nevertheless, after 214h, V_{OC} decreased from 736 to 723 mV and J_{SC} decreased significantly, from 18.7 to 17.1 mA cm^{-2}. On the other hand, as expected, the J_{SC} and V_{OC} of non-encapsulated iPSCs exposed to ambient conditions, decreased faster than encapsulated iPSCs (see Figure 4.5b), but with a similar trend.

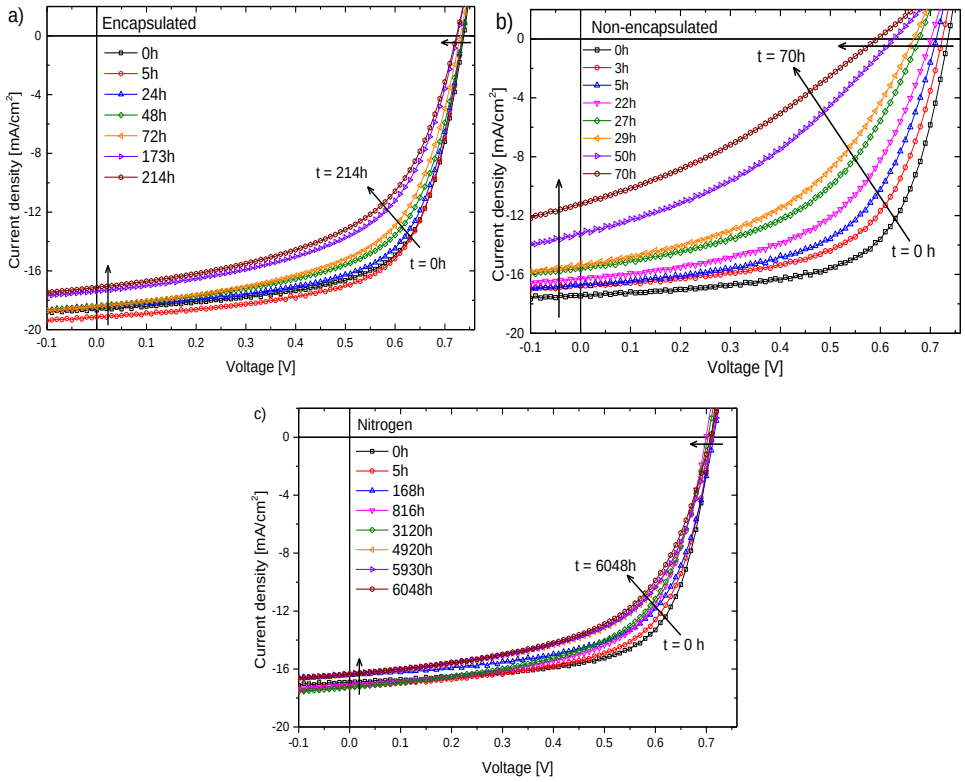

Figure 4.5 Current density-voltage characteristics of TiO_x-iPSCs under AM 1.5G irradiation exposed to ambient conditions: encapsulated (a), non-encapsulated (b) and under nitrogen (c)

The J_{SC} decreased from 17.7 to 11.4 mA cm^{-2} and V_{OC} from 734 to 590 mV after 72 h. In addition, an s-shape began to emerge in the *J-V* characteristics after 5 h of exposure to ambient conditions. After that, the PCE decreased to the 80%. However, after exposure to UV light the R_S decreased, J_{SC} increased and the s-shape disappeared. Several authors have reported that the s-shape in the *J-V* characteristics could be caused by barriers at charge extraction interfaces and the space charge limited current.[120,121] It has also been reported that the s-shape is not present in the *J-V* curves in TiO_x-iPSC because the TiO_x conductance increases after UV light soaking.[122,123] Figure 4.5c shows that the V_{OC} of TiO_x-iPSCs

stored under nitrogen was between 700 and 715 mV after 6744h of analysis. Meanwhile, J_{SC} remained at about 17 mA cm^{-2} for the first 3000h. Subsequently, J_{SC} decreased to 16.3 mA cm^{-2} after 6744 h. It is important to remark, that the s-shaped *J-V* curves of encapsulated TiO_x-iPSCs or TiO_x-iPSCs, stored under nitrogen, were not noticed in any measurement during their analysis for 214 h and 6744 h, respectively. Additionally, TiO_x-iPSCs *J-V* curves show similar degradation over time under different conditions, but the speed at which this occurs is usually related to atmospheric conditions. Since the V_{OC}, J_{SC}, FF and PCE are used to test the stability of iPSCs, these parameters were monitored over time for encapsulated, non-encapsulated under ambient conditions (23 ±2°C and 45 ±5 %RH), as well as for devices under nitrogen conditions (O_2 < 0.1 ppm and H_20 < 0.1 ppm). Figure 4.6 shows the V_{OC} (a), J_{SC} (b), FF (c) and PCE (d) as a function of the exposure time for the three sets of iPSCs. The non-encapsulated iPSCs exhibit the lowest extrinsic stability because their performance parameters decrease rapidly after a short exposure time. These devices lose 20% of their initial PCE after only 5 hours under ambient conditions.

On the other hand, encapsulated TiO_x-iPSCs only show small variations in V_{OC} and J_{SC}, which remained above 90% after 214 h of exposure to ambient conditions. Nevertheless, the PCE of these devices reduced to 80% of its initial value after 120 h. This can be attributed to oxygen and water diffusing across the encapsulating acrylic adhesive, which degrades the active layer and metal electrodes. Moreover, after 6744 h the stability of the V_{OC} of TiO_x-iPSCs stored under nitrogen remained high (98%), while the J_{SC} (95%) and FF (85%) decreased slightly, reaching 80% of PCE after 6048 h. The observed behaviour in ambient

conditions, has been attributed also, to water and oxygen degrading the electrical properties of the active layer and the electrode interfaces of PSCs.[102,124,125]

The behaviour of series and shunt resistances over time was also analysed (Figure 4.7). As shown in Figure 4.7a, the R_S of all TiO_x-iPSCs, under different conditions, increased with a similar trend to the PCE decay. The R_S in non-encapsulated iPSCs increased rapidly, although in encapsulated iPSCs, it remained stable for the first 48h and then increased slowly.

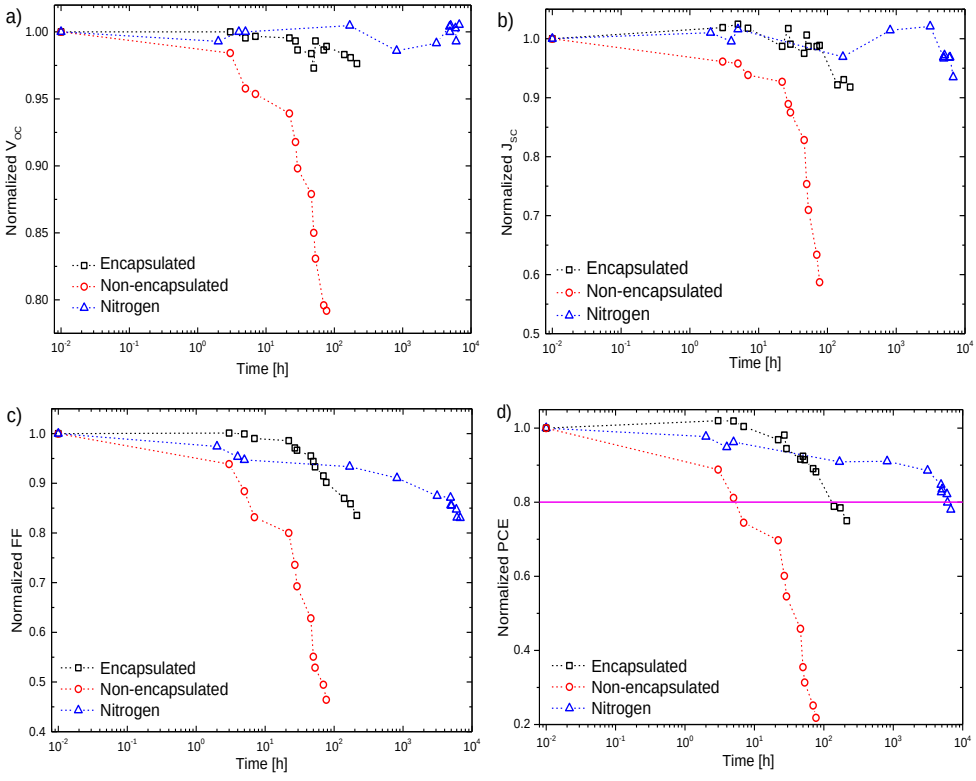

Figure 4.6 Normalized performance parameters V_{OC} (a), J_{SC} (b), FF (c) and PCE (d) of TiO_x-iPSCs under different conditions: encapsulated (black squares), non-encapsulated (red circles) and nitrogen (blue triangle)

Furthermore, the R_S of devices stored under nitrogen, increased rapidly at the beginning, remained stable for 3000 h, and then increased slowly. Moreover, the R_{Sh} of all the TiO_x-iPSCs (Figure 4.7b) showed a decrease trend similar to that of PCE. As all performance parameters, the R_{Sh} of non-encapsulated devices degraded rapidly. However, in encapsulated devices, R_{Sh} was stable for the first 24 h, after which it decreased slowly. The iPSCs stored under nitrogen showed a rapid decrease in R_{Sh} during the first 10 h and then a slower decrease for 3000 h, after which their behaviour became more disordered.

Since PCE of TiO_x-iPSCs decreased as the R_S increased and R_{Sh} decreased, the stability of TiO_x-iPSCs exposed to ambient conditions can be mainly attributed to interfaces electrodes degradation. Meanwhile, the degradation of the interface electrodes of the TiO_x-iPSCs stored under nitrogen is due to intrinsic chemical reactions between the polymer and metal materials, as well as to UV exposition.[41,105]

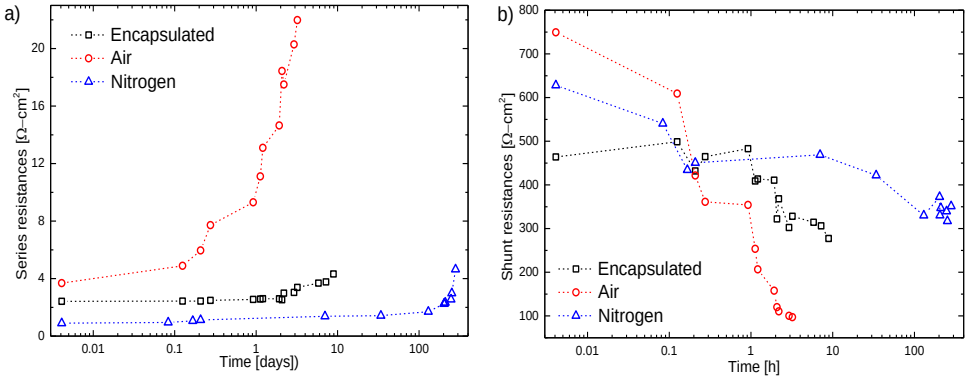

Figure 4.7 Series resistance (a) and shunt resistance (b) of TiO_x-iPSC under different conditions: encapsulated (black squares), non-encapsulated (red circles) and nitrogen (blue triangle)

4.3.4 Electron mobility

The electron mobility in the active layer of the TiO_x-iPSCs analysed above was determined, using the Mott-Gurney space-charge-limited current *(SCLC)* equation[126]:

$$J_{SCLC} = \frac{9}{8}\mu_{eff}\varepsilon_0\varepsilon_r\frac{{V_d}^2}{d^3} \tag{4.1}$$

where μ_{eff} is the effective charge carrier mobility, ε_0 the permittivity of free space ($8.85\text{x}10^{-12}$ F m^{-1}), ε_r the relative permittivity of the medium (3.5 F m^{-1})[127], J_{SCLC} the dark current density term due to the *SCLC* mechanism, calculated from an equivalent circuital model[128], d the thickness of the active layer (~100 nm), and V_d is the drop voltage in the active layer with thickness d. The V_d is the difference between the applied voltage *(V)* and the built-in potential (V_{bi}), $V_d = V\text{-}V_{bi}$.

Figure 4.8 shows the equivalent circuital model for a PSC. It includes two diodes (D1 and D2), where J_{D1} and J_{D2} are the current densities of two ideal diodes with their respective exponential factors n_{D1} and n_{D2}. The equivalent circuit also include series resistance (R_S), shunt resistance (R_{Sh}) and a *SCLC* term.

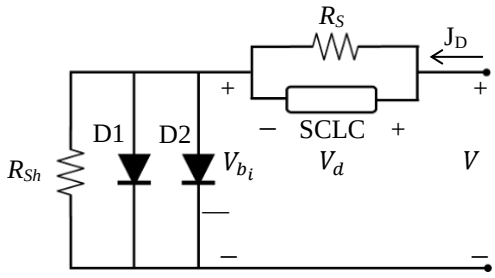

Figure 4.8 Electrical equivalent circuit of a PSC

The J_{SCLC} is defined by the parameters k and m, as show in equation:

$$J_{SCLC} = kV_d{}^m \tag{4.2}$$

Figure 4.9 shows the experimental and fitted, using the equivalent circuit in Figure 4.8, of the dark *J-V* characteristics, as well as the SCLC current density of encapsulated (a and b), non-encapsulated (c and d) and under nitrogen (e and f) TiO_x-iPSCs, for values of their PCE of 100, 90 and 80%. The experimental and fitted dark *J-V* characteristics and the J_{SCLC} of non-encapsulated devices with PCE of 100, 80 and 50% are depicted in Figure 4.9c and d, respectively. Table 4.2 summarizes the values of fitting parameters used in dark *J-V* curves of encapsulated, non-encapsulated devices and PSCs under nitrogen atmosphere. The electron mobilities calculated from equation 2 of those devices are also shown in Table 2.

4.3.5 Impedance spectroscopy

In order to investigate the degradation of encapsulated and non-encapsulated TiO_x-iPSCs, impedance spectroscopy (IS) measurements were performed under AM 1.5G illumination and ambient conditions. The IS measurements were carried out using a frequency sweep from 5 Hz to 1 MHz at three different DC bias: 0 V (short circuit current density point), 0.5 V (near to the maximum power point), and 0.8 V (near to the open circuit voltage). The IS measurements were taken over time from 24 h up to 77 h. Between measurements, the encapsulated and non-encapsulated devices were stored in dark under ambient conditions according to the ISOS standard D-1. Figure 4.10 shows the Cole-Cole plots measured in ambient conditions under illumination over time at different voltage bias.

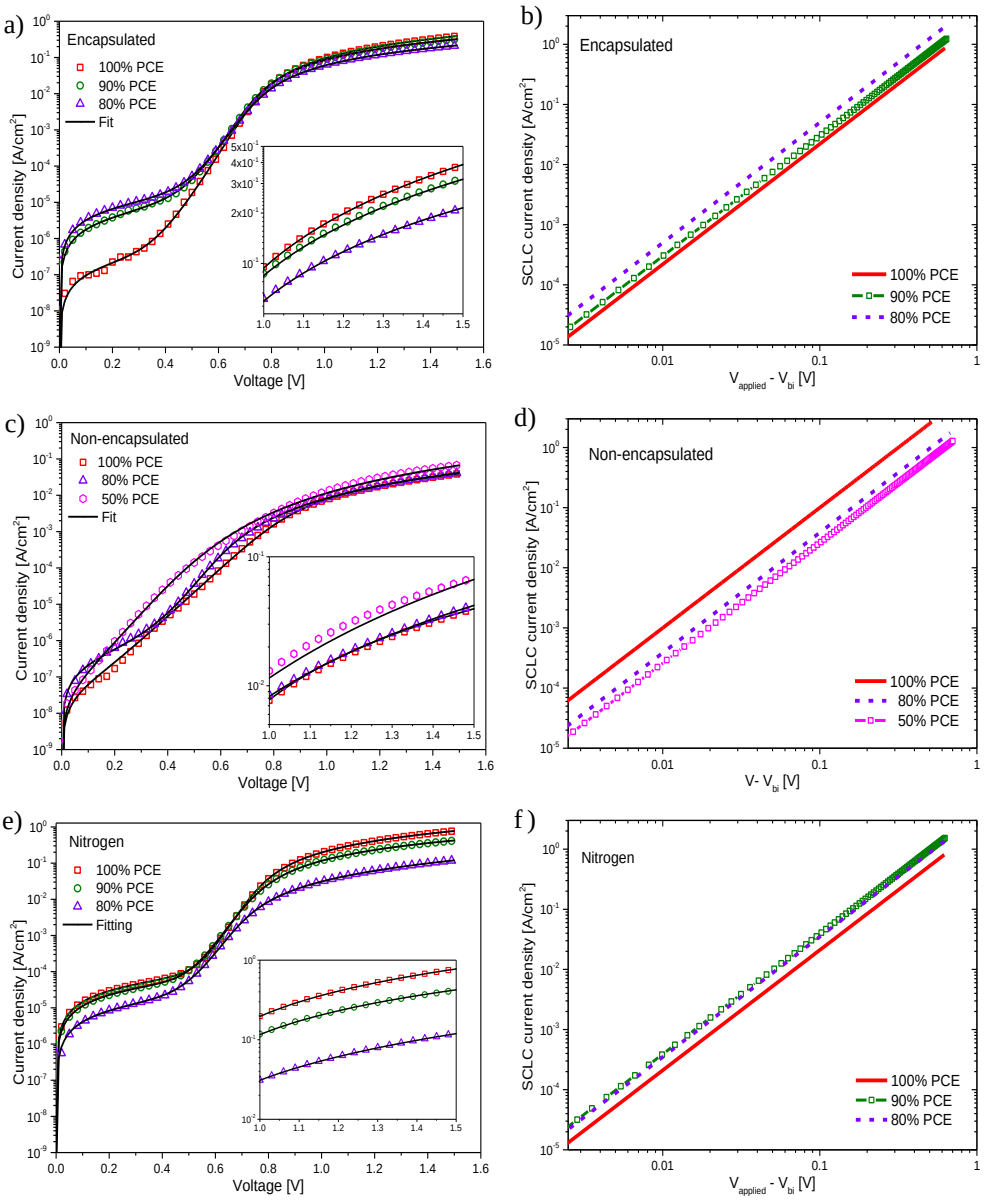

Figure 4.9 Experimental (symbols) and fitting (red solid line) of dark current density-voltage characteristics, and space-charge limited current density *vs.* voltage curves of encapsulated (a and b), non-encapsulated (c and d) exposed to ambient conditions, and under nitrogen (e and f) TiO_x-iPSCs with different PCE percentages. Inset: high forward voltages region

Table 4.2 Fitting parameters and electron mobilities values of dark *J-V* curves fit of encapsulated, non-encapsulated and nitrogen PSCs

Sample	Encapsulated			Non-encapsulated			Nitrogen		
PCE [%]	100	90	80	100	80	50	100	90	80
J_{D1} [A cm^{-2}]	1.00×10^{-11}	2.15×10^{-11}	5.00×10^{-11}	9.00×10^{-12}	4.00×10^{-10}	1.00×10^{-10}	4.50×10^{-11}	2.75×10^{-10}	1.65×10^{-11}
n_{D1}	1.37	1.41	1.49	1.90	1.71	2.50	1.43	1.58	1.41
J_{D2} [A cm^{-2}]	1.00×10^{-9}	4.00×10^{-8}	2.30×10^{-8}	1.00×10^{-8}	5.00×10^{-8}	1.50×10^{-8}	4.00×10^{-8}	7.00×10^{-9}	6.00×10^{-9}
n_{D2}	2.25	3.15	2.85	2.50	4.00	2.00	3.45	3.00	2.30
R_S [Ω]	2.03	2.35	3.20	15.00	60.00	250.00	0.90	1.57	8.00
R_{Sh} [Ω]	1.10×10^{6}	6.00×10^{4}	3.20×10^{4}	4.00×10^{6}	8.00×10^{5}	1.00×10^{7}	6.9×10^{3}	8.9×10^{3}	2.45×10^{4}
k	2.20	3.00	5.00	10.00	3.85	2.60	2.10	3.90	3.50
m	2.00	2.00	2.00	2.00	2.00	2.10	2.00	2.00	2.00
μ_{eff} [cm^2 V^{-1} s^{-1}]	6.30×10^{-5}	8.60×10^{-5}	1.40×10^{-4}	2.80×10^{-4}	1.10×10^{-4}	7.45×10^{-5}	6.00×10^{-5}	1.12×10^{-4}	1.03×10^{-4}

All plots show the typical arc behaviour, with some deviation from the perfect semicircle shape corresponding to an RC circuit. The radius of the arcs increases as time increases, at a faster rate for the non-encapsulated devices. For all cases, the arc shape does not reach zero impedance at very high frequencies. Moreover, the radii of the arcs decrease as the applied bias voltage increase in encapsulated and non-encapsulated devices. All the experimental IS spectra were fitted using an equivalent electrical model with three resistor/capacitor circuits in series (3RC circuit model). The RC circuits were associated to the resistance and capacitance of TiO_x, active layer and V_2O_5 (see Figure 4.11) by calculating the theoretical capacitance using the equation:

$$C = \varepsilon_0 \varepsilon_{layer} \frac{A}{d_{layer}} \tag{4.3}$$

where ε_0 is the vacuum dielectric permittivity, ε_{layer} is the relative dielectric permittivity ($\varepsilon_{bulk}, \varepsilon_{V_2O_5}, \varepsilon_{TiO_x}$), A is the area (0.09 cm^2) and d_{layer} is the thickness of each layer ($d_{bulk}, d_{V_2O_5}, d_{TiO_x}$).

Table 4.3 shows the thickness, dielectric permittivity taken from literature[129-131] and the theoretical capacitance calculated for each layer.

Table 4.3 Dielectric permittivity, thickness and the capacitance for each layer

Layer	Permittivity [F m^{-1}]	Thickness [nm]	Capacitance [nF]
Bulk	3.9	100	3.0
V_2O_5	5.0	5.0	79
TiO_x	50	15	200

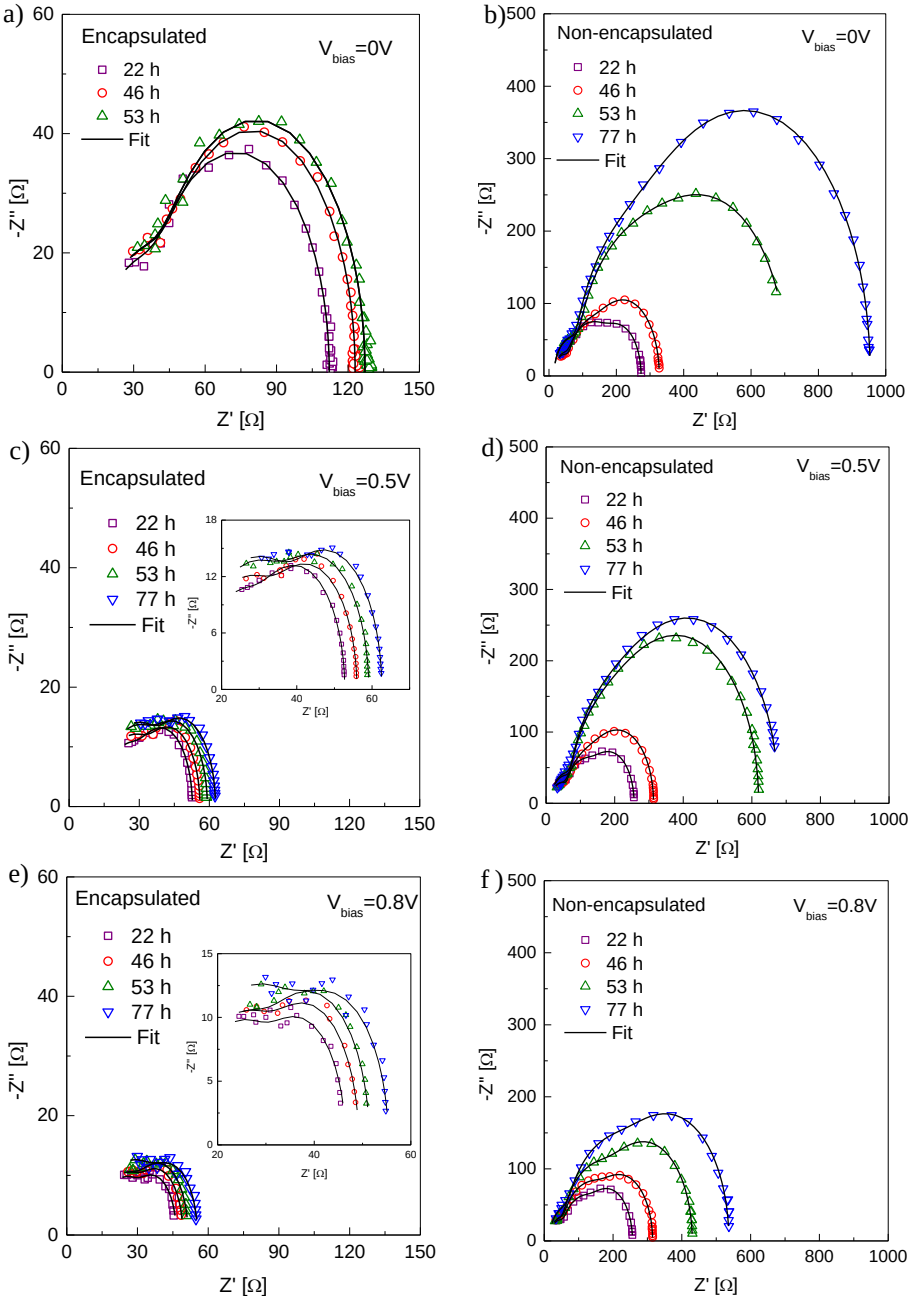

Figure 4.10 Cole–Cole plots of the encapsulated (a, c and e) and non-encapsulated (b, d and f) TiO_x-iPSCs. The IS measurements were taken at three different V_{bias}: 0V (a and b), 0.5 V (c and d), and 0.8 V (e and f). The experimental data (symbols) were fitted using the 3RC circuit model (lines)

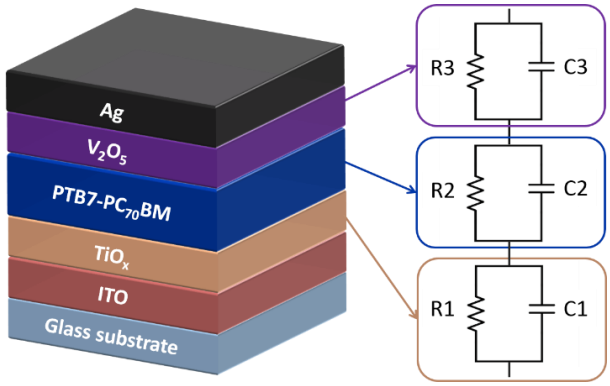

Figure 4.11 Equivalent electrical circuit with three resistor/capacitor circuits in series. The R1C1 was associated to the TiO_x (ETL), R2C2 to the bulk (active layer) and R3C3 to the V_2O_5 (HTL)

Thereby, the capacitance C1 was related to the TiO_x (ETL), C2 to the bulk (active layer) and C3 to the V_2O_5 (HTL). Figure 4.12 shows the capacitances extracted from impedance modelling over time, of encapsulated (a, c and e) and non-encapsulated (b, d and f) TiO_x-iPSCs, at three applied bias voltages. Since C1, C2 and C3 are components of the RC circuits, the three associated resistances were related to each layer. Figure 4.13 shows the resistances extracted from impedance modelling over time of encapsulated and non-encapsulated devices at 0 V (a and b), 0.5 V (c and d) and 0.8 V (e and f), respectively.

As aforementioned, the TiO_x-iPSCs are highly stable under nitrogen (in term of intrinsic stability), because the TiO_x layer reduces the photo-degradation of the active layer and the oxygen vacancies at TiO_x-active layer interface are low. Nevertheless, non-encapsulated TiO_x-iPSCs exhibit poor extrinsic stability when they are exposed to ambient condition (oxygen and water).

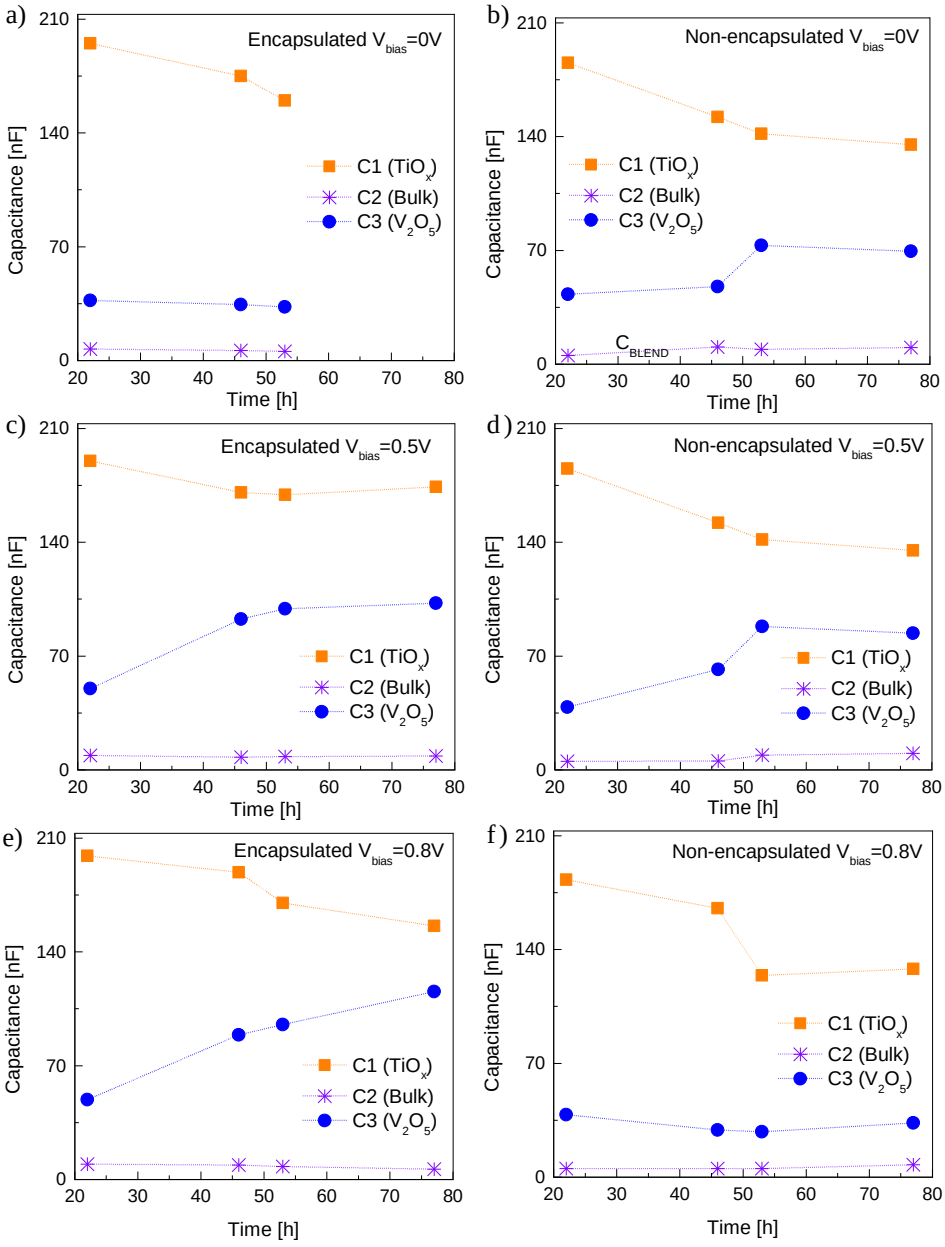

Figure 4.12 Capacitance of TiO_x (orange square), bulk (violet cross), and V_2O_5 (blue circle) over time. The values were extracted from modelling of IS measurements of the encapsulated (a, c and e) and non-encapsulated (b, d and f) TiO_x-iPSCs. The IS measurements were taken at three different V_{bias}: 0 V (a and b), 0.5 V (c and d), and 0.8 V (e and f)

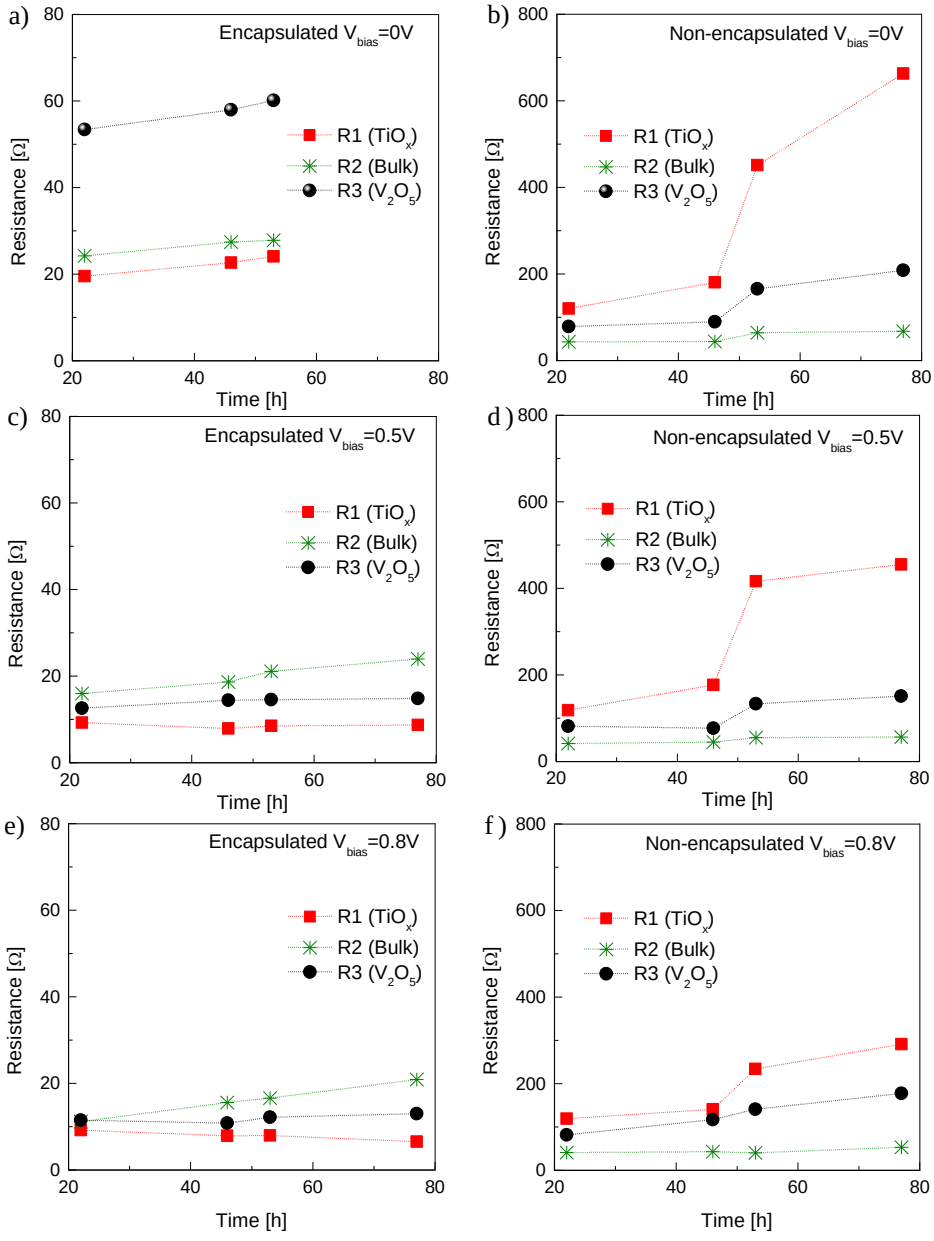

Figure 4.13 Resistances of TiO_x (red square), bulk (green cross), and V_2O_5 (black circle) over time. The values were extracted from modelling of IS measurements of the encapsulated (a, c and e) and non-encapsulated (b, d and f) TiO_x-iPSCs. The IS measurements were taken at three different V_{bias}: 0 V (a and b), 0.5 V (c and d), and 0.8 V (e and f)

The degradation process in encapsulated TiO_x-iPSCs is slower than that in non-encapsulated devices. The resistance of TiO_x, V_2O_5, and bulk layers in encapsulated devices, exhibit a slightly variation over degradation time at the different applied voltages. The TiO_x layer shows the lowest resistance over degradation time at the three-different applied voltage. The bulk layer exhibits the highest resistance over time at 0.5 V. The resistance of all layers, in encapsulated devices, remained below 20 Ω excluding the resistance of V_2O_5 layer at zero voltage. Despite being sheltered by the acrylic adhesive, the water and oxygen present in ambient, diffused across the encapsulating adhesive to reach and degrade the device. This water and oxygen diffusion occurs sooner than expected, thus the encapsulated devices degrade slower than non-encapsulated one with the same degradation mechanism. The low stability of encapsulated TiO_x-iPSCs is ascribed to the simple encapsulation methodology used. To reach a long-term stability, more complex encapsulation process must be applied.

In non-encapsulated TiO_x-iPSCs, the resistance of the TiO_x layer increases from 119 Ω up to 662 Ω at 0 V, from 114 Ω up to 455 Ω at 0.5 V, and from 115 Ω up to 285 Ω after 77 h of exposure to ambient conditions. The V_2O_5 and bulk layers showed lower resistance values that increased at smaller rates. V_2O_5 layer exhibits a maximum resistance of about 200 Ω and a minimum of 80 Ω during all the exposure time, while the resistance of bulk layers remained below 75 Ω during the time of exposure to ambient. Note that resistance decreases when the applied bias voltage increases. The results of impedance spectroscopy analysis indicate that the poor stability of non-encapsulated TiO_x-iPSCs is mainly related to degradation of TiO_x/bulk interface. Carp et al., have reported the

photoinduced superhydrophilicity phenomenon, where trapped holes at the TiO_x surface can induce a high wettability.[132] This photoinduced superhydrophilicity and the thin thickness of TiO_x layer allow the absorption of oxygen and water from the ambient. For this reason, the poor extrinsic stability of TiO_x-iPSCs is attributed to the fast degradation of TiO_x/bulk layer interface.

4.4 Influence of Pd-doped TiO_x on iPSCs performance

Herein, the TiO_x thin-films used as ETL has demonstrated to improve the performance and stability under nitrogen atmosphere of PSCs. However, TiO_x-iPSCs under ambient conditions still exhibit poor stability. To improve the stability and performance of TiO_x-iPSCs, the optimization of the TiO_x layer is required to reduce losses at the TiO_x/organic blend interface. Doping the TiO_x layer by introducing a small amount of a well-chosen dopant is a promising approach, due to the possibility of modifying the grain size, orientation, the electrical conductivity and Fermi level position.[133,134] One of the most attractive advantage of TiO_x doping is the reduction of the number of oxygen vacancies and deep trap states which reduce the recombination losses. Several authors have reported that TiO_x doped with several materials (e.g. cesium[135], tin[133], zinc, polyethylene oxide[136], flour[137], iron[111] and gold[138]) can be used as ETL to improve the PCE of PSCs. The doping of TiO_x with palladium (Pd-doped TiO_x) has been reported for photocatalytic applications, however, to the best of knowledge, Pd-doped TiO_x has not been yet reported for PSCs fabrication. Here, iPSCs based on PTB7:$PC_{70}BM$ were fabricated using Pd-doped as ETL. Some iPSCs with pristine TiO_x were fabricated as control. The fully architecture of devices

is as follows: ITO//TiO_x or Pd-doped TiO_x/PTB7:$PC_{70}BM$/V_2O_5/Ag. All the devices were fabricated with the same procedure than TiO_x-iPSCs described above in this chapter (see section 4.2).

4.4.1 Pd-doped TiO_x solution synthesis

Pd-doped TiO_x layer were synthetized via sol–gel methods using the spin coating technique. Pd-doped TiO_x solution was prepared by mixing Titanium(IV) isopropoxide $Ti[OCH(CH_3)_2]_4$, 0.68M) and Palladium(II) acetylacetonate ($Pd(C_5H_7O_2)_2$) in 2-methoxyethanol ($CH_3OCH_2CH_2OH$). Ethanolamine ($H_2NCH_2CH_2OH$, 1.6M) was added as stabilizer. Pd-doped TiO_x solutions with several palladium(II) acetylacetonate concentration (0.125 mM, 0.25 mM, 0.5 mM, 1mM, 3.5 mM, 7mM, 14mM, 28 mM and 56 mM) were synthetized. All the mixtures were stirred and heated at 120 °C under inert atmosphere. Subsequently, the solutions were diluted in anhydrous methanol with a volume ratio 1:6, respectively, and stirred at room temperature for 1 hour. Diluted TiO_x-precursor was spin-cast in air on top of the ITO substrates at 6000 rpm. In order to convert the precursor in TiO_x by hydrolysis, samples were left in ambient conditions for 1 hour and heated at 400°C. For the synthesis of pristine TiO_x refer section 4.2.1. The name of the samples and their Pd concentration used to dope the TiO_x are showed in Table 4.3. The lowest Pd concentration used was 0.125 millimolar (mM) and the highest 56 mM.

Table 4.4 Name of samples and Pd-concentration in Pd-doped TiO_x

Sample	A	B	C	D	E	F	G	H	I	J
Pd [mM]	0	0.125	0.25	0.50	1.0	3.5	7	14	28	56

4.4.2 Electrical characterization of iPSCs with Pd-doped TiO_x

The current density-voltage (*J-V*) characteristics of PSC with pristine and Pd-doped TiO_x layer were measured in dark and under simulated AM1.5G illumination (100 mW cm^{-2}). The samples were classified in low Pd concentration (B, C, D and E) and high Pd concentration (F, G, H, I and J) devices depending on whether they exhibited or not the s-shape in the *J-V* characteristic. Figure 4.14 shows best *J-V* characteristics of samples with high (a) and low (b) Pd concentration. The devices made with pristine TiO_x is plotted in both curve as reference. The Figure 4.14c shows the process to remove the s-shape from *J-V* characteristic of samples I (28 mM Pd). The s-shape was removed from all devices with high Pd concentration after several measurements under light illumination. The number of measurements to remove the s-shape as increases as the Pd concentration. Importantly, in samples with pristine TiO_x and low Pd concentration, the s-shape was not observed.

From Figure 4.14a, samples A and F exhibited the highest V_{OC}. Moreover, the V_{OC} is slightly reduced as the Pd concentration increased in samples G, H and I. Nevertheless, sample J showed the lowest V_{OC}. In addition, sample A showed the highest J_{SC}. On the other hand, in samples with Pd-doped TiO_x layer, J_{SC} decreased as the Pd concentration increases, excluding sample F and G. On the other hand, the *J-V* curves of samples with low Pd concentration (Figure 4.14b) exhibited similar trend among them and sample A. The J_{SC} of samples with low Pd concentration are slightly higher than that of samples with pristine TiO_x. On the other hand, all samples exhibited similar V_{OC}.

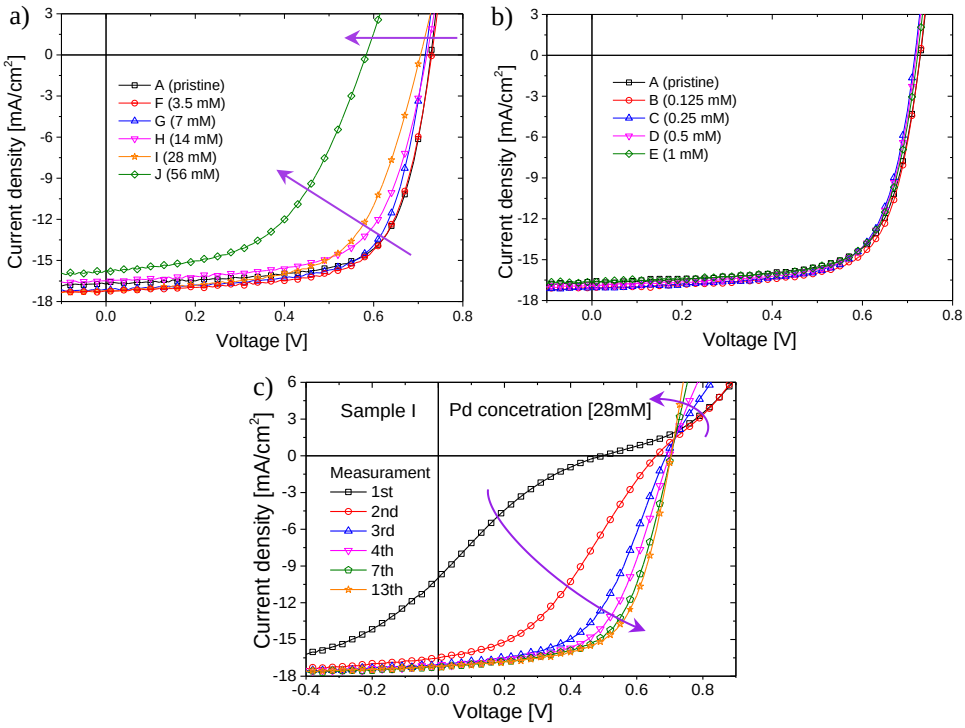

Figure 4.14 *J-V* characteristic of devices with Pd-doped TiO_x with high (a) and low (b) Pd concentration; s-shape removing from *J-V* characteristics of sample I (c)

The V_{OC} is slightly affected by using low Pd concentration from 0.125 mM up to 14 mM, while using higher Pd concentration V_{OC} decreases 20% with respect to the sample with pristine TiO_x. The J_{SC} is improved in samples B, C, F, G and I, while in samples D, E, H, and J the J_{SC} decreases as the Pd concentration increases. Samples with low PD concentration exhibited similar FF and PCE, while in samples with high Pd concentration the FF and PCE decreases as the Pd concentration increases (excluding the PCE of sample F that is similar to that of low Pd concentration samples). Samples with low Pd concentration exhibited similar R_S and higher R_{Sh} than that of samples with pristine TiO_x.

On the other hand, both the R_S and R_{Sh} of devices with high Pd concentration get worse by increasing the Pd concentration. The samples with TiO_x doped with a Pd concentration of 0.125 mM exhibited the best performing than samples with different Pd concentration. Moreover, this sample improved the PCE by ~4% in comparison to samples with pristine TiO_x.

Doping the TiO_x with Pd concentrations up to 1 mM allows to improve the shunt resistances of the iPSCs that use TiO_x as ETL. On the other hand, the TiO_x doped with concentrations of Pd higher than 1 mM are detrimental to the iPSCs performing.

Table 4.5 Performance parameter of iPSCs with pristine and Pd-doped TiO_x

Sample	V_{OC} [mV]	J_{SC} [mA cm^{-2}]	FF [%]	PCE [%]	R_S [Ω cm^{-2}]	R_{Sh} [Ω cm^{-2}]
A	730	16.72	69.62	8.50	1.50	909
B	**730**	**17.10**	**70.59**	**8.81**	**1.50**	**1309**
C	720	17.11	69.43	8.52	1.50	1100
D	720	16.92	70.00	8.52	1.50	1362
E	720	16.58	71.00	8.49	1.61	1133
F	729	17.21	68.34	8.59	2.20	875
G	719	17.06	65.62	8.21	2.88	950
H	719	16.51	65.31	7.75	3.52	770
I	709	17.30	64.23	7.63	5.40	601
J	579	15.71	52.41	4.81	7.73	408

4.5 Conclusions

In this chapter an inverted solar cell based on PTB7:$PC_{70}BM$, using TiO_x as the ETL that enhances stability and efficiency under nitrogen storage, is presented. The PCE of TiO_x-iPSCs (8.43%) increased by ~5% and ~11% compared to PFN-iPSCs and conventional PSCs, respectively. J_{SC} also increased by ~16%, while the V_{OC} and FF showed no significant improvement. The lifetime of TiO_x-iPSCs under nitrogen was about 5 times longer than that of PFN-iPSCs and conventional PSCs (6048 h, 1300 h and 1200 h, respectively). These results show an improvement of the long-term stability of PSCs when a TiO_x interlayer is added between the active layer and the cathode. In contrast, under ambient conditions, non-encapsulated TiO_x-iPSCs showed low stability with a lifetime of about 5 h. Their electron mobility was also reduced by 75% from 2.8 x 10^{-4} to 7.45 x 10^{-5} cm^2 V^{-1} s^{-1} after 24h. Upon encapsulation, the lifetime of TiO_x-iPSCs increased to 120 h and their electron mobility was not reduced. IS analysis allowed to separately analyse the influence of TiO_x, V_2O_5 and bulk layers on the degradation inside of the cells. On the basis of impedance spectroscopy and electron mobility results, the poor stability of non-encapsulated TiO_x-iPSCs is strongly attributed to the degradation of TiO_x/bulk interface and the reduction of electron mobility in active layer by effect of oxygen and moisture. With the purpose of improving the lifetime of TiO_x-iPSCs, more complex and efficient encapsulation process must be performed. The iPSCs fabricated with Pd-doped TiO_x as ETL with low Pd concentration show a significantly improvement of the PCE. Devices with Pd-doped TiO_x exhibit reduction of the shunt losses compared to cells with pristine TiO_x. Moreover, TiO_x with low Pd concentration could be used as ETL to improve the performance of iPSCs.

Nevertheless, Pd concentrations higher than 3.5 mM are detrimental for the performance of devices. Finally, these results demonstrate that the use of TiO_x as an electron transport layer is crucial for improving the efficiency and the stability of future organic and hybrid solar cells.

Chapter 5

Impact of inkjet printed ZnO electron transport layer on the characteristics of inverted polymer solar cells

5.1 Introduction

In the last decade, the performance of PSCs has increased rapidly, mainly due to the development of new polymers with improved light absorption, charge carrier mobility and crystallinity.[43,76,139,140] As such, efficiencies over 11% have been reported for lab-scale studies.[141,142] However, despite these spectacular figures, these efficiencies has not be yet reached in large-scale processes.[143] In this respect, roll-to-roll (R2R) processes have been shown to be the most promising alternative for large-scale PSCs fabrication. Most of the printing and coating techniques (i.e. screen printing, inkjet printing, gravure printing, spray coating, and blade coating) are compatible with R2R process for large-scale PSCs fabrication. Among these, the inkjet printing (IJP) is a very promising technique towards large-scale production of PSCs and commercialization. Although spin coating is the most common techniques for lab-scale PSCs fabrication, it is not compatible with R2R process.[144] IJP has already been used for the manufacture of organic electronics devices.[95-97]

This chapter describes the fabrication and characterization of iPSCs using zinc oxide deposited by IJP (ZnO-IJP) as electron transport layer (ETL). ZnO was selected as ETL, because of it can be easily solution-processed on ITO substrates at room temperature. Moreover, several authors have reported ZnO-IJP layers on the fabrication of thin film transistors, micro photodetectors and iPSCs.[145-147] The iPSCs were fabricated based on active layers composed of PTB7:Th and $PC_{70}BM$ using vanadium oxide (V_2O_5) as hole transport layer and silver (Ag) as anode. Similar devices were fabricated with ZnO as ETL, deposited by spin coating (ZnO-SC), and thermal evaporation (ZnO-TE) as control. Figure

5.1 shows the architecture (a) and the energy level diagram for materials used in the devices (b), taken from the literature.[43, 108,140,148] A qualitative charge carrier recombination kinetics analysis was carried out using the charge carrier extraction (CE) and transient photovoltage (TPV) methods. The results of CE/TPV, combined with ideality factor analysis, demonstrated that recombination kinetics are governed by different mechanisms in IJP-made devices with respect to SC and TE–made devices. Additionally, Impedance Spectroscopy (IS) results reveal that devices made from ZnO-IJP exhibit a similar charge transport resistance as devices with ZnO-SC, while devices with ZnO-TE show the highest charge transport resistance.

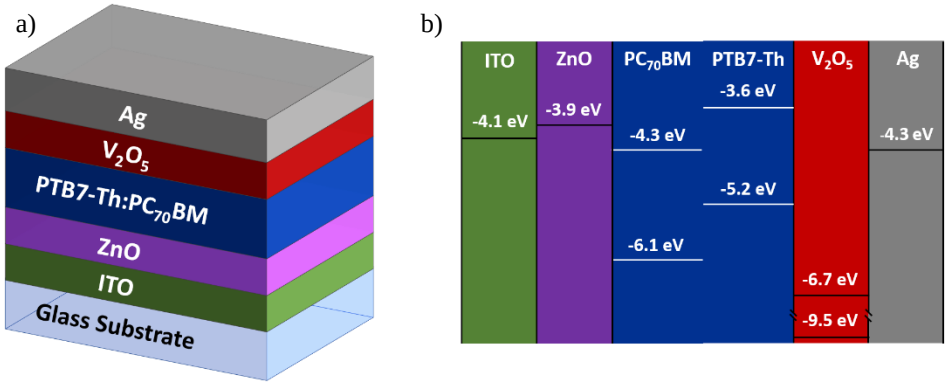

Figure 5.1 Inverted architecture of the fabricated devices (a). Energy level diagram for materials used for device fabrication taken from the literature (b)

5.2 Experimental details

5.2.1 ZnO-IJP layer

First, the ZnO nanoparticle ink (ZnO-ink) with a viscosity of about 8-14 cp and nanoparticle size around 8-16 nm was sonicated during 10 min and filtered through 0.2 μm PTFE filter. The ZnO-ink was deposited

on pre-cleaned patterned ITO-coated glass substrate, using a DIMATIX DMP-2800 printer. The printing parameters are as follows: drop spacing of 10 μm, drop velocity of 8 m/s, 15 nozzles at 16 V and jetting frequency of 5 kHz. Subsequently, the samples were sintered at 115 °C, during 10 min in air, in a conventional oven.

5.2.2 ZnO-SC layer

The ZnO precursor was prepared by dissolving zinc acetate dihydrate ($Zn(CH_3COO)_2 \cdot 2H_2O$ 0.68M and ethanolamine 0.46M in 2-methoxyethanol ($CH_3OCH_2CH_2OH$), leaving them under vigorous stirring for 1 h at 70 °C. Subsequently, the precursor solution of ZnO was diluted in methanol in 1:1 ratio. This solution was spin coated on pre-cleaned patterned ITO-coated glass substrate at 3000 rpm for 30 s. The resulting ZnO film was heated at 110 °C for 1 h in air.

5.2.3 ZnO-TE layer

The pre-cleaned patterned ITO-coated glass substrates were transferred to a high vacuum chamber and 45 nm of ZnO were thermally evaporated at $9x10^{-7}$ mbar with an evaporation rate ranging from 0.04 to 0.08 nm s^{-1}.

5.2.4 Blend solution preparation

The blend solution was prepared by dissolving PTB7-Th and $PC_{70}BM$ (1:1.5 w/w) in chlorobenzene and 1,8-diiodooctane (97:3 by volume) with a concentration of 25 mg mL^{-1}. The blend solution was left stirring and heating at 40 °C overnight, and further aged for 48 h in dark under nitrogen atmosphere.

5.2.5 Solar cells fabrication

The solar cells were fabricated on indium tin oxide (ITO) patterned glass substrates. The ITO substrates (10 Ω/□) were cleaned in acetone, ethanol and isopropanol using an ultrasonic bath. Subsequently, ITO was dried at 100 °C followed by UV-ozone treatment. Subsequently, the ITO substrates were coated with ZnO (~40 nm) by either inkjet printing, spin coating or thermal evaporation as described above. The blend solution was spin-coated on top of the ZnO interlayer at 800 rpm for 30 s to obtain an active layer 100 nm-thick. The samples were transferred to a vacuum chamber and 5 nm of V_2O_5 and 100 nm of Ag were deposited by thermal evaporation on top of the active layer at 8 x 10^{-7} mbar. The active area for all devices was 0.09 cm^2.

5.3 Results and discussion

5.3.1 Electrical characterization

The current density-voltage (*J-V*) characteristics of iPSCs were measured in dark and under simulated AM1.5G illumination (100 mW cm^{-2}). Figure 5.2 shows the current density-voltage *(J–V)* characteristics of the best-performing iPSCs in dark (a) and under simulated AM 1.5G illumination (b), as well as, the external quantum efficiency (EQE) of the devices with ZnO deposited by the three different techniques (c). Interestingly, the devices made from ZnO-IJP exhibit higher open circuit voltage *(V_{OC})* than that of devices with ZnO-SC and ZnO-TE. However, the trend of short circuit current density *(J_{SC})* is opposite to that of the V_{OC}, where devices made from ZnO-SC show the highest J_{SC}. Those made from ZnO-IJP show the lowest J_{SC} of all. Devices with ZnO-TE exhibit the lowest V_{OC}, while J_{SC} is higher than for devices with ZnO-IJP.

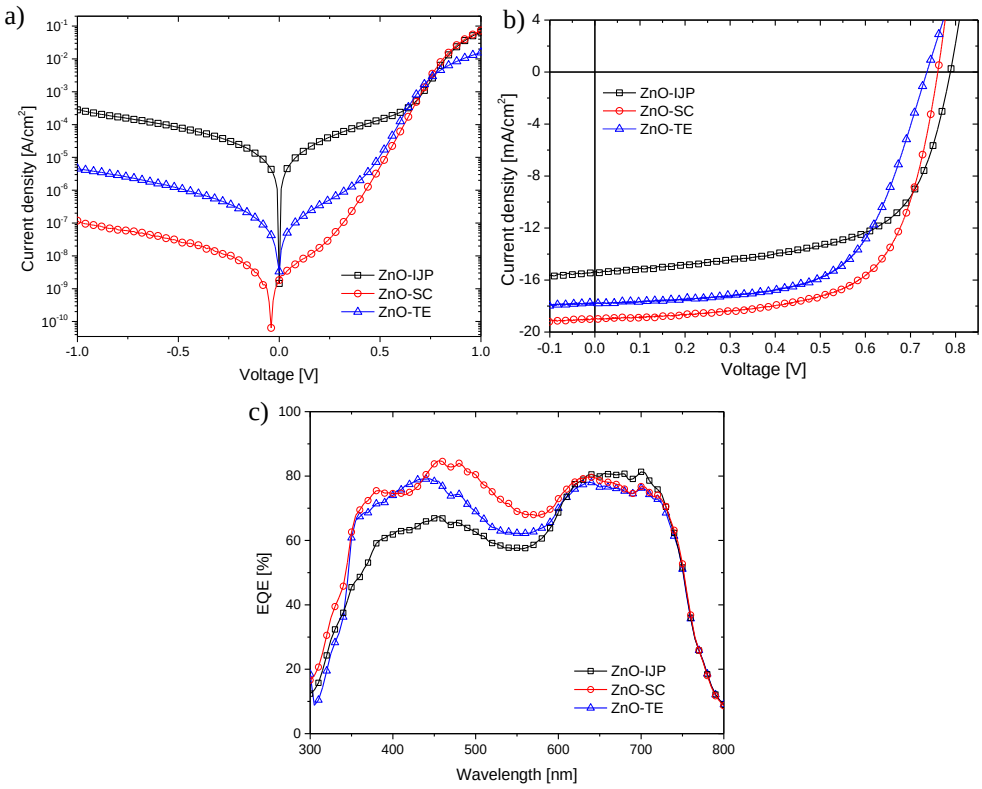

Figure 5.2 Current density versus voltage *(J–V)* characteristics of the best-performing iPSCs with ZnO-IJP (black squares), ZnO-SC (red circles) and ZnO-TE (blue triangles) in dark (a) and under simulated AM 1.5G illumination (b); EQE spectra of the best-performing devices

Table 5.1 summarizes the features of the best-performing devices. The standard deviation for all parameters of iPSCs was calculated over eight devices and is depicted in parentheses in Table 1. The devices made from ZnO-IJP show a power conversion efficiency (PCE) of 7.47%, a V_{OC} of 0.789 V, a J_{SC} of 15.35 mA cm^{-2} and a fill factor (FF) of 61.59%. The devices made from ZnO-IJP and ZnO-SC have similar V_{OC} and series resistances (R_S), while devices with ZnO-TE have the lowest V_{OC} and highest R_S. The PCE of the devices made from ZnO-IJP is ~20% and ~9% lower than that of devices with ZnO-SC and ZnO-TE, respectively. All the devices have

similar FF. These results are similar to those reported from devices based on PTB7-Th:$PC_{70}Bm$ with ZnO as ETL deposited by spin-coating[43,79,149], spray coating[80] and sputtering[150] techniques. The devices made from ZnO-IJP exhibit somewhat higher dispersion, which can be attributed to the non-optimum homogeneity of the ZnO layer. The EQE curves are seen to corroborate the trend observed for the J_{SC}, as seen by the calculated J_{SC} from EQE in Table 5.1. All the devices exhibit similar spectral response from 600 nm to 800 nm, however the devices made from ZnO-IJP show a significant decrease in photon conversion efficiency from 300 nm to 600 nm with respect to the other devices. This behaviour has been previously observed in iPSCs, when ZnO nanoparticles were used as ETL.[151,152] Figure 5.3 shows the UV-Vis spectroscopy analysis of ZnO-IJP, ZnO-SC and ZnO-TE layers (a and b), as well as of PTB7-Th:$PC_{70}BM$ layer on top of ZnO-IJP, ZnO-SC and ZnO-TE layers (c, d and e). This analysis shows that the decrease in EQE is the result of an increase in reflectance together with a slight decrease in absorption of the active layer in the case of the device made from ZnO-IJP.

Table 5.1 Parameters of iPSCs based on PTB7-Th:$PC_{70}BM$ under 100 mW cm^{-2} AM1.5G illumination with ZnO-IJP, ZnO-SC and ZnO-TE as ETL

Device	V_{OC} [mV]	J_{SC} [mA cm^{-2}]	J_{SC} (EQE) [mA cm^{-2}]	FF [%]	PCE [%]	R_S [Ω-cm^2]	R_{Sh} [Ω-cm^2]
ZnO-IJP	789 (26)	15.35 (1.57)	14.85	61.59 (3.56)	7.47 (0.66)	2.11 (0.81)	376 (48)
ZnO-SC	761 (4)	18.94 (0.35)	18.62	65.31 (1.41)	9.42 (0.16)	1.97 (0.28)	751 (105)
ZnO-TE	737 (14)	17.79 (0.26)	16.94	62.29 (0.52)	8.17 (0.24)	8.69 (0.68)	850 (195)

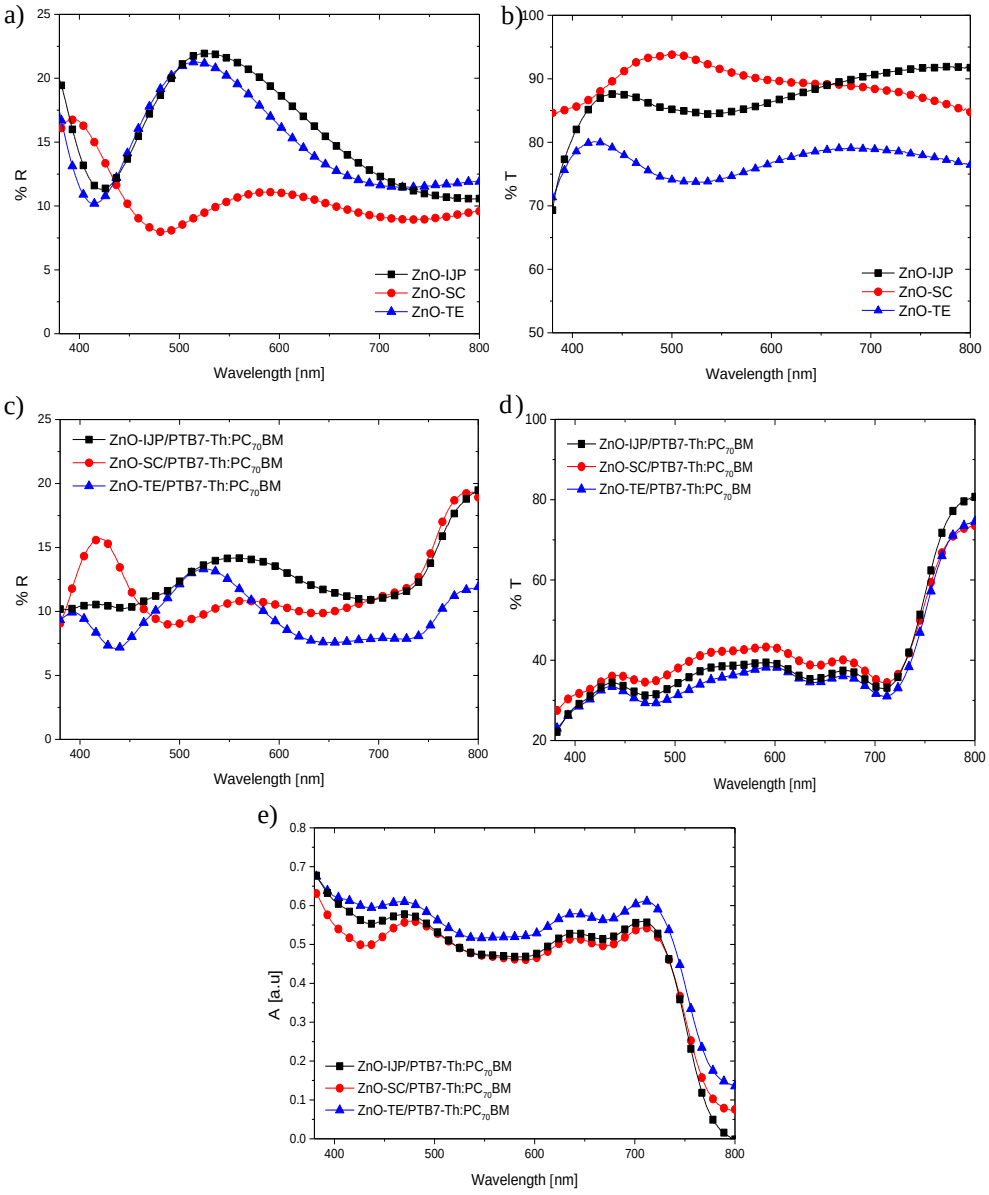

Figure 5.3 Reflectance (a) and transmittance (b) spectra of ZnO-IJP (black squares), ZnO-SC (red circles) and ZnO-TE (blue triangles) layers. Reflectance (c) and transmittance (d) and absorbance (e) spectra of ZnO-IJP/PTB7-Th:$PC_{70}BM$ (black squares), ZnO-SC/PTB7-Th:$PC_{70}BM$ (red circles) and ZnO-TE/PTB7-Th:$PC_{70}BM$ (blue triangles) layers

5.3.2 Morphological characterization

To understand how the morphology of the ZnO affects the properties of the active layers, an AFM analysis on all three types of ZnO layers was carried out. All the films were deposited on ITO-coated glass substrates in identical conditions as in solar cell devices. Topography images (5x5 μm and 1x1 μm) of ZnO film deposited by IJP (Figure 5.4a and d), spin coating (Figure 5.4b and e) and thermal evaporation (Figure 5.4c and f), were recorded.

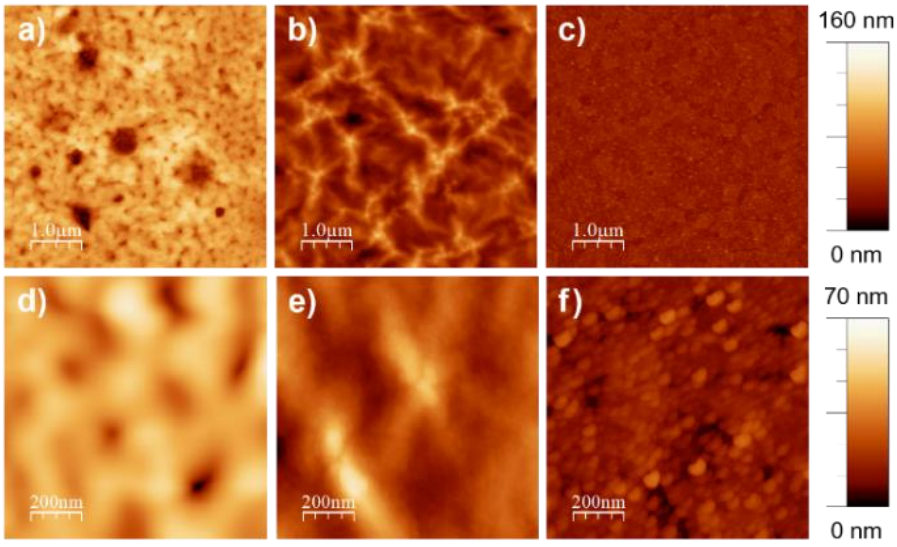

Figure 5.4 AFM (5x5 μm) topographical images using tapping mode: a) ZnO-IJP film, b) ZnO-SC film and c) ZnO-TE film. AFM (1x1 μm) topographical images using tapping mode: d) ZnO-IJP film, e) ZnO-SC film and f) ZnO-TE film

Table 5.2 shows the root-mean-square (RMS) roughness and the maximum peak to peak height of each ZnO film. Interestingly, all three deposition techniques lead to very rough surfaces with RMS roughness values over 7 nm for both IJP and SC layers. The peak to peak height is higher than 30 nm in all cases. The evaporated ZnO layer shows a marked

granular topography with grains size in the range of 30 nm, while the other two types of ZnO layers show a much less homogenous topography. The ZnO-SC has more of a "mountain and valley"-like aspect, while the ZnO-IJP layers shows clear aggregates of ZnO nanoparticles. Additionally, it should be noted that the ZnO-IJP layer forms an "isle"-like pattern at macroscopic scale, a result of the nozzle- injection process (see micrograph in Figure 5.5a).

Table 5.2 RMS and peak to peak roughness of iPSCs with ZnO-IJP, ZnO-SC and ZnO-TE calculated from AFM topography (5x5 µm and 1x1 µm) measurements

AFM tapping	ZnO layer	Roughness	
		RMS [nm]	peak to peak [nm]
5x5 µm	ZnO-IJP	16.82	134.77
	ZnO-SC	16.19	116.61
	ZnO-TE	5.08	100.95
1x1 µm	ZnO-IJP	7.18	60.88
	ZnO-SC	8.62	58.74
	ZnO-TE	4.26	31.81

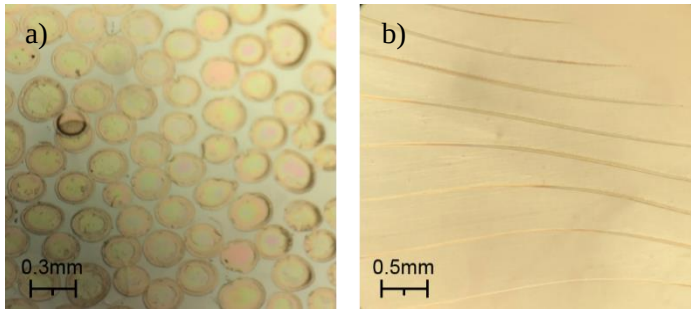

Figure 5.5 Micrograph of ZnO-IJP layer on ITO (a) and on glass (b)

5.3.3 Photophysical characterization

To assess the extent to which the morphology of the ZnO layer affects the energetics of the active layer of the solar cell devices, we carried out a comparative analysis of their ideality factors (n_{id}). To do so, the *J-V* characteristics of the devices were recorded at different light intensities under simulated AM 1.5G illumination as shown in Figure 5.6 (a, b and c). The plot of V_{OC} as a function of the light intensity (LI) is depicted in Figure 5.6d. To calculate the n_{id}, the plot V_{OC} vs LI was fitted to the equation (5.1):

$$V_{OC} = n_{id}\left(\frac{kT}{q}\right) ln\,(light\ intensity) + b \qquad (5.1)$$

where k is the Boltzmann constant, T is the temperature, and q is the elementary charge. The values of n_{id} obtained for devices with ZnO-IJP, ZnO-SC and ZnO-TE were 1.5, 1.2 and 1.0, respectively. These values lie within the range of expected values ($1 \leq n_{id} \leq 2$) for OPV devices. Interestingly, the high value of n_{id} (1.5) of the ZnO-IJP-made devices suggests the presence of a high concentration of deep trap states in the bulk. On the other hand, the devices made from ZnO-SC and ZnO-TE show very low n_{id}. Devices made from ZnO-SC with a n_{id} of 1.2 are in the range of devices in which recombination occurs between a free charge carrier and one carrier trapped in a band tail. For ZnO-TE, the exceptionally low n_{id}, may be evidence of a more tail to tail-like recombination mechanism.[153] Figure 5.6e shows the plot J_{SC} vs LI and was fitted to the power law of the form of equation (2), where b = 0.95, 1.0 and 0.98 for devices with ZnO-IJP, ZnO-SC and ZnO-TE, respectively. These b values indicate that non-geminate recombination is not significant near to short circuit and that no space charge is present.[154]

$$J_{SC} = A\,(light\ intensity)^{b} \tag{5.2}$$

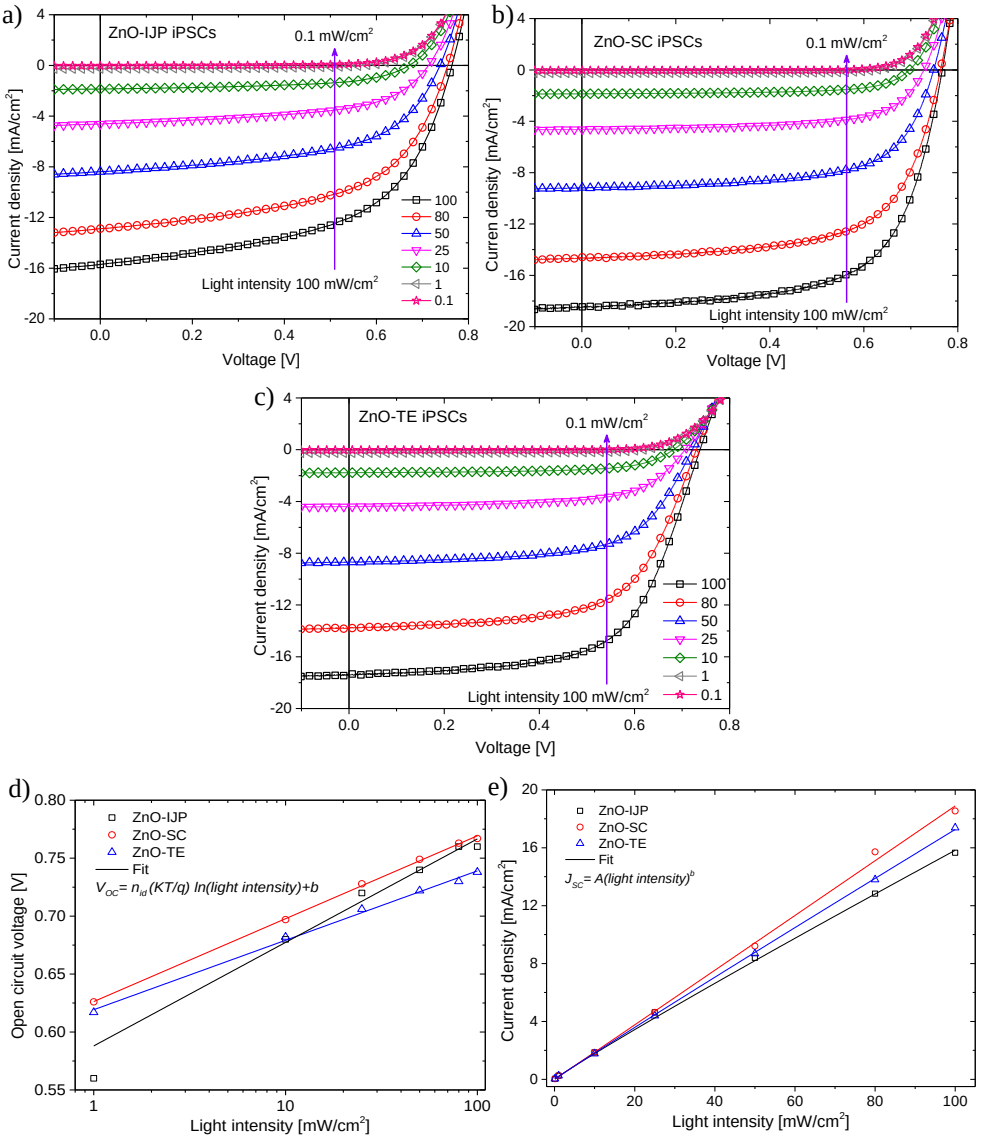

Figure 5.6 Current density versus voltage characteristics of iPSCs with ZnO-IJP (a), ZnO-SC (b) and ZnO-TE (c) under AM 1.5G illumination measured at several light intensities; Open circuit voltage as a function of light intensity (d); Current density as a function of light intensity (e). The curves d and e were fitted (lines) on the form of equations 1 and 2, respectively

To gain more insight on how the band structure affects the *J-V* characteristics of the devices, particularly the V_{OC}, we carried out a charge carrier recombination kinetics study of the ZnO-based devices, using charge extraction/transient photovoltage techniques (CE/TPV).[155-164] The CE measurements allow measuring the average charge density under open circuit conditions.[154-156,165,166] Figure 5.7a shows the charge carrier density as a function of light bias, resulting in a V_{OC} ranging from 100 to 750 mV. The charge density for all devices close to 1 Sun, is in the range of 10^{16} cm^{-3}, being in good agreement with the reported values for similar organic materials.[157] The density of charge in the region from 0.65 V to 0.76 V exhibits an exponential dependency and is related to the accumulated charge within the bulk of the device, analogously to the splitting of the quasi-Fermi levels in intrinsic semiconductors. The curve was fitted using equation (5.3) and the γ values for samples are shown in Table 5.3.

The rather low value of γ of devices with ZnO-IJP (4.3) is lower than that expected for ideal semiconductors, an effect that has been attributed to the presence of an exponential tail of trap states extending into the band gap of the active layer. Figure 5.7b shows the carrier lifetime ($\tau_{\Delta n}$) as a function of the V_{OC} of devices. The curve was fitted using a single exponential decay in the form of equation (5.4). The β value for each device is shown in Table 5.3.

$$n = n_0 \, e^{(\gamma V_{OC})} \tag{5.3}$$

$$\tau_{\Delta n} = \tau_{\Delta n_0} \, e^{(-\beta V_{OC})} \tag{5.4}$$

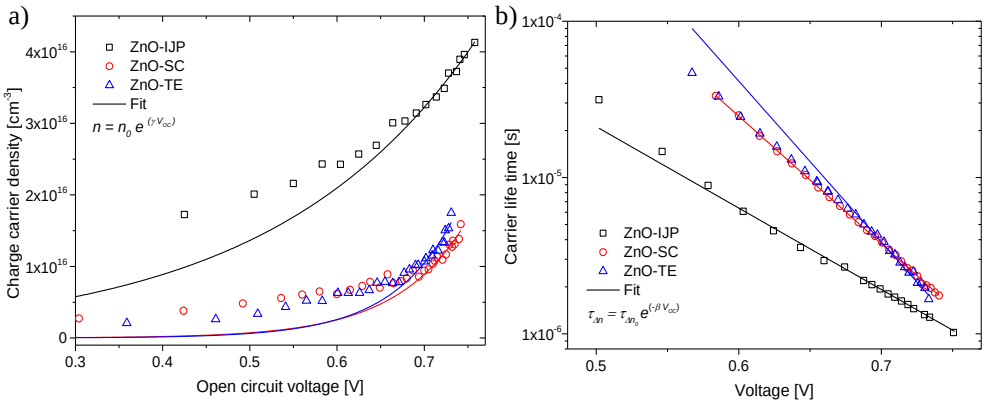

Figure 5.7 Charge carrier density (n) as a function of the V_{OC} determined from CE measurements (a). The curves were fitted (lines) on the form of equation (5.3). Carrier lifetime ($\tau_{\Delta n}$) as a function of device V_{OC}. For TPV measurements (b), the transients were induced by a low intensity, pulsed excitation at 650 nm with the devices at open circuit conditions. The curves were fitted (lines) on the form of equation (5.4)

Figure 5.8 shows the recombination dynamics of the small perturbation lifetimes combined with the density of charges obtained from CE, allowing determining the overall order of recombination (ϕ) defined by equation (5.5), where, ϕ can be calculated using equation (5.6) assuming $\Delta n << n$ in the experimental TPV conditions. The value of ϕ can also be calculated using equation (5.7).[156] The β was calculated by fitting the curve $\tau_{\Delta n}$ vs n using equation (5.8). The calculated values of λ and ϕ of all devices are summarized in Table 5.3.

$$\frac{dn}{dt} = -kn^{\Phi} \tag{5.5}$$

$$\Phi = \lambda + 1 \tag{5.6}$$

$$\phi = (\beta/\gamma) + 1 \tag{5.7}$$

$$\tau_{\Delta n} = \tau_{\Delta n_0} n^{-\lambda} \tag{5.8}$$

Table 5.3 Values of recombination parameters derived from CE/TPV measurements for devices with ZnO layer deposited by IJP, spin coating and thermal evaporation

Parameter	ZnO-IJP	ZnO-SC	ZnO-TE
n_0	1.6x10^{15}	1.4x10^{12}	5.8x10^{11}
γ	4.30	12.5	14.0
β	12.7	18.8	23.7
λ	3.0	1.5	1.7
ϕ (Eqn. 5.6)	4.0	2.5	2.7
ϕ (Eqn. 5.7)	4.0	2.5	2.7

The devices made from ZnO-SC and ZnO-TE exhibit similar recombination orders (2.5 and 2.7, respectively), while those from ZnO-IJP-made devices are significantly higher (~4). Such a high value, as opposed to a value of 2, have been measured several times in earlier reports[153], and are to be expected in devices in which recombination is mediated by deep trap states, as corroborated by the high n_{id}. Additionally, the low surface coverage at the macroscopic scale of the ZnO-IJP substrates (see micrograph in Figure 5.5a) is consistent with the high ϕ being indicative of significant surface recombination. The low recombination orders measured for the ZnO-SC and ZnO-TE devices are consistent with recombination occurring from traps in the band tails, or with tail to tail-like recombination, as suggested by the extremely low n_{id}.

Surface recombination is less significant in these two cases, indicating that the high peak to peak height of the ZnO films does induce a notably lower surface coverage. Most importantly, the significantly slower perturbation lifetimes measured from ZnO-IJP are consistent with the significantly higher V_{OC} observed for these devices with respect to those made from the other two ZnO deposition techniques. The opposite trend is observed between the ZnO-SC and ZnO-TE devices. Their relative difference in V_{OC} is, therefore, likely the result of difference in DOS distribution. That is, the device with broader DOS (qualitatively estimated through the parameter γ in the n vs. applied bias plot), i.e. ZnO-SC-made devices, have a higher V_{OC} than ZnO-TE-made devices, despite the fact that their corresponding small perturbation lifetimes are slightly faster that the latter.[166-170]

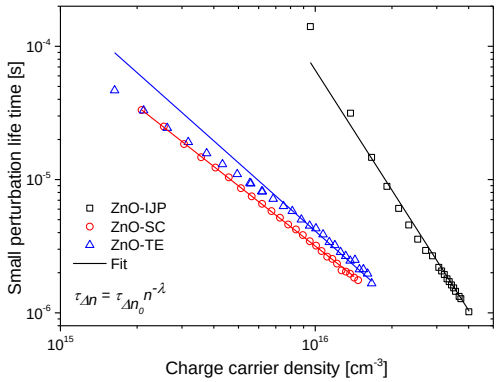

Figure 5.8 Carrier lifetime ($\tau_{\Delta n}$) vs. carrier density (n) plot for iPSCs with ZnO-IJP (black squares), ZnO-SC (red circles) and ZnO-TE (blue triangles) as ETL. The curves were fitted (lines) to a power law decay of the form of equation (5.8)

5.3.4 Impedance spectroscopy

To quantify the effect of the ZnO-IJP layer on charge transport properties, impedance measurements (IS) were carried out on all the

devices at different voltage biases. IS provides valuable information on carrier transport mechanisms involved in the charge extraction on PSCs.[89,108,171-175] Figure 5.9 shows the Nyquist plots for ZnO-IJP (a), ZnO-SC (b) and ZnO-TE (c) as ETL taken at different voltages under AM1.5 illumination. The Nyquist plots show mainly one semicircle for all applied voltages (medium frequency from 10 to 1×10^5 Hz), which is associated with charge transfer at the electrode/active layer interface.[176]

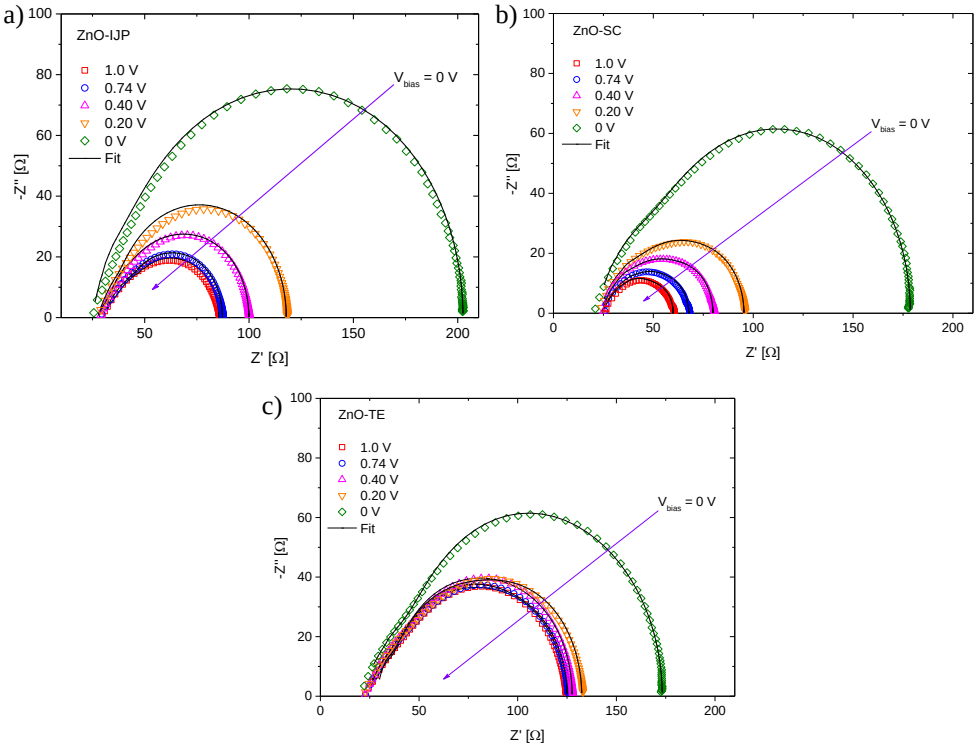

Figure 5.9 Experimental (markers) and fitted (line) IS response for iPSCs using ZnO-IJP (a), ZnO-SC (b) and ZnO-TE (c) measured under 1 sun conditions at several applied voltages: 0, 0.2, 0.4, 0.74 and 1V

The experimental impedance spectra were fitted using an equivalent electrical model with three resistor/capacitor circuits (3RC) in

series[108,174,177] (see Figure 5.10). Each element of the circuit is associated to the capacitance and resistance of the three different layers of the iPSC devices.[108,175,176] The fitting was performed in Matlab (R2014a) using custom computational methods and literature algorithms[178], yielding R and C values for the different applied voltage biases. The capacitances of the three RC circuit at the different applied voltages were calculated from the fitting of the IS measurements of devices made from ZnO-IJP, ZnO-SC and ZnO-TE. The capacitances were linked to the layers involved in the charge transport process by the theoretical capacitance calculation using the equation 4.3 (see section 4.3.4):

$$C = \varepsilon_0 \, \varepsilon_{layer} \, \frac{A}{d_{layer}} \tag{4.3}$$

where ε_0 is the vacuum dielectric permittivity, ε_{layer} is the relative dielectric permittivity ($\varepsilon_{bulk}, \varepsilon_{V_2O_5}, \varepsilon_{ZnO}$), A is the area (0.09 cm^2) and d_{layer} is the thickness of each layer ($d_{bulk}, d_{V_2O_5}, d_{ZnO}$). The values used for calculating the capacitance of each layer by equation (4.3) are shown in Table 5.4. Thus, the capacitance C1 to the ZnO, C2 to the bulk and C3 to the V_2O_5. Since C1, C2 and C3 are a component of the RC circuits, the three associated resistances were related to each layer (see Figure 5.10). The dielectric permittivity for each layer was taken from literature.[129-131]

Table 5.4 Dielectric permittivity, thickness and the capacitance for each layer

Layer	Permittivity [F m^{-1}]	Thickness [nm]	Capacitance [nF]
Bulk	3.9	100	3.0
V_2O_5	5.0	5.0	79.0
ZnO	4.0	40.0	8.0

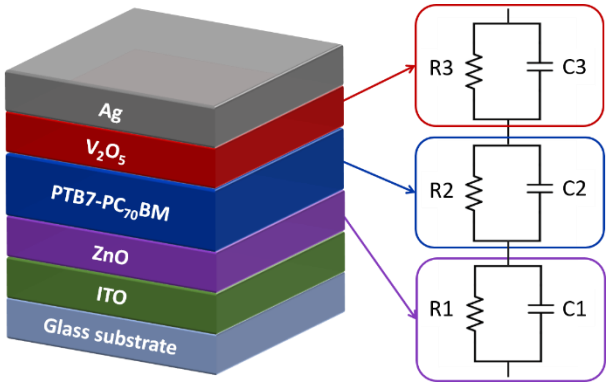

Figure 5.10 Equivalent electrical circuit with three resistor/capacitor circuits in series. The R1C1 was associated to the ZnO (ETL), R2C2 to the bulk (active layer) and R3C3 to the V_2O_5 (HTL)

Figure 5.11 shows the capacitances and the resistance extracted from impedance modelling for devices using ZnO-IJP (a and b), ZnO-SC (c and d) ZnO-TE (e and f) as ETL, respectively. The resistances values of ZnO and V_2O_5 layers are similar in iPSCs with ZnO-IJP and ZnO-SC. In both devices, the resistance of ZnO and V_2O_5 layers decreases as the applied voltage increases. The resistances of ZnO and V_2O_5 layers decrease from ~80 Ω (ZnO-IJP) and ~60 Ω (ZnO-SC) at 0 V to ~20 Ω at 1 V. These high values of resistance at low voltages (from 0 V to 0.2 V) suggest that shunt resistance losses are mainly caused by the hole- and electron-transport layers.

In devices with ZnO-TE the resistances of V_2O_5 is lower than that of ZnO. Moreover, at high voltages (from 0.7 V to 1 V) the ZnO and V_2O_5 layers of iPSCs with ZnO-IJP and ZnO-SC exhibit lower resistance values that that of devices with ZnO-TE. These results corroborate the values of series resistances of the devices calculated from *J-V* characteristics.

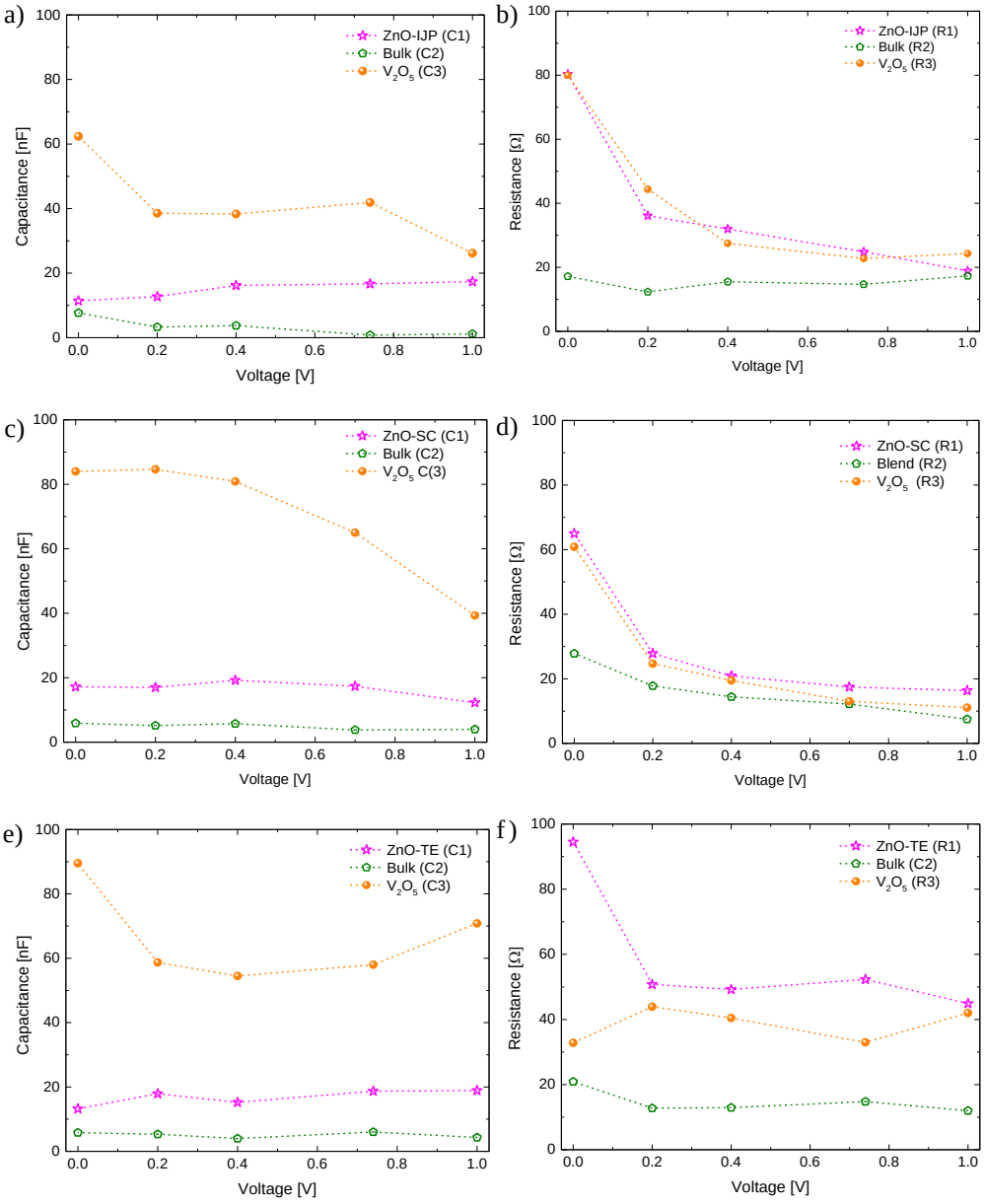

Figure 5.11 Capacitance and resistance data extracted from the fitting of IS measurements for devices using ZnO-IJP (a and b), ZnO-SC (c and d) ZnO-TE (e and f), respectively

5.4 Conclusions

This chapter describes the use of an inkjet printed ZnO layer as ETL in iPSCs based on PTB7-Th:$PC_{70}BM$. The iPSCs devices showed a maximum power conversion efficiency of 7.47%, which compares very favourably to that obtained on similar iPSCs using ZnO-SC and ZnO-TE layers. Combined results from ideality factor and non-geminate recombination studies has brought substantial evidence of a modification of the band structure properties of the active layer, triggered by the ZnO type of under-layer the active layer is deposited on to. As such, the active layer deposited on top of ZnO-IJP shows a higher density of deep trap states, than those deposited on top of ZnO-SC and ZnO-TE. The difference in band structure energetics and recombination dynamics has been shown to follow the trend in V_{OC} measured experimentally from the three types of devices. Additional IS measurements have demonstrated that electron injection and extraction have an impact on the shunt and series resistances of the ZnO-IJP-made and ZnO-TE-made devices, thus lowering the FF of both devices slightly. The main parameter limiting the PCE of the ZnO-IJP devices with respect to ZnO-SC and ZnO-TE devices is the lower J_{SC}, which is, to some extent, the result of a lower spectral photon conversion efficiency in the visible range of the solar spectrum. This effect, was shown to be due to an increase in reflectance together with a slight decrease in absorption of the active layer. The morphological aspects of the ZnO layer are not seen to induce an increase in recombination kinetics. On the contrary the higher V_{OC} of ZnO-IJP is the result of slower recombination kinetics with respect to the other two deposition techniques. These results demonstrated that ZnO-IJP layer can be successfully used for the fabrication of highly efficient iPSCs.

Chapter 6

General conclusions

6.1 Summary and conclusions

Herein the fabrication, modelling and characterization of polymer-based organic solar cells with inverted architecture (iPSCs) were described. The thesis was focused on the study of the simultaneously improvement of efficiency and long-term stability of iPSCs based on polymer:fullerenes. The polymers PTB7 and PTB7-Th were used as the electron donor materials, whereas the fullerene $PC_{70}BM$ was used as the electron acceptor. The zinc oxide (ZnO) and titanium oxide (TiO_x) were used as electron transport layers (ETL), moreover PFN was used for comparison purpose. All iPSCs were characterized by optical, electrical and photophysical methods in order to understand the loss mechanisms involved in the degradation process of these devices. Equivalent circuit models were used to analyse the dark *J-V* characteristics and the impedance spectroscopy data to identify the origin of the loss mechanisms.

In Chapter 3, the polymers and fullerene materials that conform the active layer were described. Subsequently, the materials used as buffer layer, ETL or hole transport layer (HTL), for the fabrication of PSCs with conventional and inverted architecture were presented. The materials used as buffer layers for conventional PSCs fabrication were also presented. Afterward, the thin-film deposition techniques (i.e. spin coating, inkjet printing and thermal evaporation), as well as the step-by-step process for the polymer solar cells fabrication with conventional and inverted architecture were described. Finally, the methodology for the current vs voltage, external quantum efficiency, charge carrier extraction, transient photovoltage, and impedance spectroscopy measurements used for the characterization of iPSCs were discussed.

In chapter 4, the stability study of high efficiency iPSCs was described. The devices were fabricated based on PTB7:$PC_{70}BM$ using an ultra-thin film of TiO_x as ETL. The performing and stability of TiO_x-iPSCs were compared to that of conventional PSCs and iPSCs using PFN as ETL. TiO_x-iPSCs exhibited an efficiency 5% and 11% higher than that of PFN-iPSCs and conventional PSCs. Under dry nitrogen (N_2) atmosphere, TiO_x-iPSCs shown a lifetime (PCE = 80 %) of 6048 h, that is five times longer than that of conventional PSCs (1200 h) and PFN-iPSC (1300 h). TiO_x-iPSCs stability was analysed by exposing encapsulated and non-encapsulated TiO_x-iPSCs to ambient conditions (23 °C and 45% humidity). The non-encapsulated devices exhibited a lifetime of several hours and an electron mobility 75% lower than that of devices under N_2 atmosphere. This low stability is attributed to the degradation of the contact interfaces driven by ambient oxygen and water. On the other hand, encapsulated TiO_x-iPSCs exhibited a lifetime of about 120 h with no observed loss in electron mobility. Moreover, it was demonstrated that the shunt losses of iPSCs can be reduced by using TiO_x doped with a small amount of palladium [0.125 mM]. Therefore, the efficiency of devices with Pd-doped TiO_x was up to 4% higher than that of iPSCs with pristine TiO_x.

In Chapter 5, the effects of ZnO layers deposited by inkjet printing (ZnO-IJP) as ETL on the performance of iPSCs based on PTB_7-Th:$PC_{70}BM$ were explored. The main motivation was to demonstrate that ZnO-IJP layers can be successfully applied to the fabrication of high efficient iPSCs. The morphology of the ZnO-IJP layer was analysed by AFM and compared to that of ZnO layers deposited by spin coating (ZnO-SC) and thermal evaporation (ZnO-TE). The study shown that the band structure and non-geminate recombination kinetics of PTB7-Th:$PC_{70}BM$ layer is

affected by the morphology of the ZnO underlayer. In addition, charge carrier and transient photovoltage measurements reveal that non-geminate recombination is governed by deep trap states in iPSCs with ZnO-IJP, whereas trapping is less significant for devices with ZnO-SC and ZnO-TE. It was found that the efficiency of iPSCs made with ZnO-IJP is mainly limited by their slightly lower J_{SC} since the low photon conversion efficiency in the visible part of the solar spectrum. Despite this current limitation, the performance of iPSCs with ZnO-IJP compares very favourably with that of devices made with ZnO-SC and ZnO-TE.

In conclusion, high efficient and stable organic solar cells based on PTB7:$PC_{70}BM$ and PTB7-Th:$PC_{70}BM$ with inverted architecture were demonstrated in this thesis. Moreover, TiO_x used as an electron transport layer is crucial for improving the efficiency and the stability of iPSCs. Finally, it was also demonstrated that ZnO layers deposited by inkjet printing can be successfully applied to the fabrication of high efficiency iPSCs at laboratory scale.

6.2 Future works

In spite of the good results obtained in this thesis, several experiments could not be done due to lack of time, e g. the iPSCs fabrication and their characterization are time consuming, moreover the stability experiments are carried out as longer as possible. For these reasons, future works concern deeper analysis of loss mechanism, stability under different conditions, new materials for active and buffer layers. The further work that could be tested is as follows:

- Optimization the synthesis of Titanium-doped to improve the stability and charge extraction in iPSCs.

- Optimization of encapsulation process to improve the long-term stability of iPSCs under real operational conditions.

- Optimization of the depositing parameters of the ZnO-ink by the inkjet printing to obtain a high uniform layer.

- Fully inkjet printed polymer solar cell fabrication in a flexible substrate.

- Optical, electrical and photophysical characterization of fully printed iPSCs, as well as the study of their stability over time.

- Fabrication, characterization and modelling of iPSCs based on new polymers and non-fullerenes materials.

- Fabrication, characterization and modelling of iPSCs based on ternary blends (polymer:fullerene:non-fullerenes).

References

[1] A. E. Becquerel, *Compt. Rend. Acad. Sci*., 1839, 9, 145.

[2] C. E. Fritts, *Am. J. Sci.,* 1883, 26, 156, 465–472.

[3] D. M. Chapin, C. S. Fuller, G. L. Pearson, *J. Appl. Phys*., 1954, 25, 676.

[4] C. W. Tang, *Appl. Phys. Lett.*, 1986, 48, 183.

[5] K. Yoshikawa, H. Kawasaki, W. Yoshida, et al., *Nat Energy*., 2017, 2, 5, 17032.

[6] T. Magorian, Friedlmeier, P. Jackson, A. Bauer, D. Hariskos, O. Kiowski, R. Menner, R. Wuerz, M. Powalla, *Thin Solid Films*, 2017, 633, 13-17.

[7] R. Komiya, A. Fukui, N. Murofushi, N. Koide, R. Yamanaka, H. Katayama, *Technical Digest, 21st International Photovoltaic Science and Engineering Conference, Fukuoka,* 2011; 2C- 5O- 08.

[8] M. Liu, O. Voznyy, R. Sabatini, F. Pelayo García de Arquer, R. Munir, A. Hesham Balawi, X. Lan, F. Fan, G. Walters, A. R. Kirmani, S. Hoogland, F. Laquai, A. Amassian, E. H. Sargent, *Nat. Mater*., 2017, 16, 258–263.

[9] W. S. Yang, J. H. Noh, N. J. Jeon, Y. C. Kim, S. Ryu, J. Seo, S. Seok, *Science*., 2015, 348, 6240, 1234- 1237.

[10] S. Mori, H. Oh- oka, H. Nakao, T. Gotanda, Y. Nakano, H. Jung, A. Iida, R. Hayase, N. Shida, M. Saito, K. Todori, T. Asakura, A. Matsui, M. Hosoya, *MRS Proceedings*, 2015, 1737.

[11] C. J. Brabec, *Sol. Energy Mater. Sol. Cells*, 2004, 83, 2–3, 273–292.

[12] M. C. Scharber and N. S. Sariciftci, *Prog. Polym. Sci*., 2013, 38, 12, 1929–1940.

[13] H. Klauk, Organic Electronics Materials, Manufacturing and Applications, *Edit. WILEY-VCH Verlang GmbH & Co. KGaA*, first edition, 2006.

[14] W. R. Salaneck, R. H. Friend, J. L. Brédas, *Phys. Rep. -Rev. Sec. Phys. Lett.,* 1999, 319, 231-251.

[15] W. Brütting, C. Adachi, Physics of organics semiconductors, *WILEY-VCH*, Weinheim, second edition, 2005.

[16] A. Miller and E. Abrahams, *Phys. Rev*, 1960, 120, 745.

[17] R. A. Marcus, *ReV. Mod. Phys.*, 1993, 65, 599.

[18] K. Colladet, S. Fourier, T. J. Cleij, L. Lutsen, J. Gelan, D. Vanderzande, L. H. Nguyen, H. Neugebauer, S. Sariciftci, A. Aguirre, *Macromolecules*, 2007, 40, 65-72.

[19] I. G. Hill, A. Kahn, G. Soos, R. A. Pascal, *Chem. Phys. Lett.*, 2000, 327, 181.

[20] Y. J. Cheng, S. H. Yang, C. S. Hsu, *Chem. Rev.*, 2009, 109, 5868-5923.

[21] J. L. Brédas, J. E. Norton, J. Cornil, V. Coropceanu, *Acc. Chem. Res.*, 2009, 42, 1691-1699.

[22] E. A. Silinsh, V. Capek, Organic molecular crystals - interaction, localization and transport phenomena, *American Institue of Physics*, 1994.

[23] C. Guo, W. Hong, H. Aziz, Y. Li, *Reviews in Advanced Sciences and Engineering*, 2012, 1, 3, 200.

[24] T. M Clarke, J. R. Durrant, *Chem. Rev.* 2010, 110, 6736-6767.

[25] D. Moses, J. Wang, G. Yu, A. Heeger, *Physical review letters,* 1998, 80, 2685.

[26] C. Deibel, T. Strobel, V. Dyakonov, *Adv. Mater.*, 2010, 22, 4097-4111.

[27] P. Heremans, D. Cheyns, B.P. Rand, *Acc. Chem. Res.*, 2009, 42, 1740−1747.

[28] H. Hoppe, N.S. Sariciftci, *J. Mater. Res.,* 2004, 19 1924-1945.

[29] S. M. Sze, K. K. Ng, Physics of Semiconductor Devices, Wiley, third edition, 2006.

[30] J. J. M. Halls, K. Pichler, R. H. Friend, S. C. Moratti, A. B. Holmes, *Appl.Phys.Lett.*, 1996, 68, 3120-3122

[31] C. W. Tang, *Appl. Phys. Lett.*, 1986, 48, 183.

[32] H. Kim, S. Nam, J. Jeong, S. Lee, J. Seo, H. Han, Y. Kim, *Korean J. Chem. Eng.*, 2014, 31, 1095–1104.

[33] G. Yu, J. Gao, J. C. Hummelen, F. Wudl, A. J. Heeger, *Science*, 1995, 270, 1789.

[34] M. T. Dang, L. Hirsch, G. Wantz, J. D. Wuest, *Chem. Rev.*, 2013, 113, 3734-3765.

[35] V. Dyakonov, *Physica*, 2002, E 14, 53.

[36] P. Schilinsky, C. Waldauf, C. J. Brabec, *Appl. Phys. Lett.*, 2002, 81, 3885.

[37] H. L Yip, A. K.-Y.Jen, *Energy & Environmental Science*, 2012, 5, 5994-6011.

[38] R. Po, C. Carbonera, A. Bernardi, N. Camaioni, *Energy & Environmental Science*, 2011, 4, 285-310.

[39] T.-H. Lai, S.-W. Tsang, J. R. Manders, S. Chen, F. So, *Materials Today,* 2013, 16, 11.

[40] Z. Yin, J. Wei, Q. Zheng, *Adv.Sci.*,2016, 3, 1500362.

[41] M. Jørgensen, K. Norrman, F. C. Krebs, *Sol. Energy Mater. Sol. Cells*, 2008, 92, 7, 686–714.

[42] M. T. Greiner, M. G. Helander, W.-M. Tang, Z.-B. Wang, J. Qiu, Z.-H. Lu, *Nat. Mater.*, 2012, 11, 1, 76–81.

[43] Z. He, C. Zhong, S. Su, M. Xu, H. Wu, Y. Cao, *Nat. Photonics*, 2012, 6, 9, 593–597.

[44] J. Nelson, The Physics of Solar Cells, *Imperial College Press*, First edition, 2003.

[45] W. J. Potscavage Jr., A. Sharma, B. Kippelen, *Acc. Chem. Res.*, 2009, 42, 1758-1767.

[46] S. Günes, H. Neugebauer, N. S. Sariciftci, *Chem. Rev.*, 2007, 107, 1324-1338.

[47] A. Checknane, H. S. Hilal, F. Djeffal, B. Benyoucef, J. P. Charles, *Microelectron. J.*, 2008, 39, 173–1180.

[48] B. Kan, M. Li, Q. Zhang, F. Liu, X. Wan, Y. Wang, W. Ni, G. Long, X. Yang, H. Feng, Y. Zuo, M. Zhang, F. Huang, Y. Cao, T. P. Russell, Y. Chen, *J. Am. Chem. Soc.*, 2015, 137, 11, 3886–3893.

[49] R. L. Uy, S. C. Price, W. You, *Macromol. Rapid Commun.*, 2012, 33, 14, 1162–1177.

[50] G. H. L. Heintges, P. J. Leenaers, and R. A. J. Janssen, *J. Mater. Chem. A*, 2017, 5, 26, 13748–13756.

[51] H. Shirakawa, E. J. Louis, A. G. MacDiarmid, C. K. Chiang, A. J. Heeger, *Chem. Commun.*, 1977, 578.

[52] C. K. Chiang, C. R. Fincher, Jr., Y. W. Park, A. J. Heeger, H. Shirakawa, E. J. Louis, *Phys. Rev. Lett.*, 1977, 39, 1098.

[53] S. E. Shaheen, C. J. Brabec, N.S. Sariciftci, *Appl Phys Lett.*, 2001, 78, 841–3.

[54] A. C. Arias, J. D. MacKenzie, R. Stevenson, J. J. M. Halls, M. Inbasekaran, E. P. Woo, *Macromolecules*, 2001, 34, 6005–13.

[55] N. Camaioni, G. Ridolfi, G. Casalbore-Miceli, G. Possamai, M. Maggini, *Adv Mater*, 2002, 14, 1735–8.

[56] W. Ma, C. Yang, X. Gong, K. Lee, A. J. Heeger, *Adv. Funct. Mater.*, 2005, 15, 10, 1617–1622.

[57] G. Li, V. Shrotriya, J. Huang, Y. Yao, T. Moriarty, K. Emery, Y. Yang, *Nat. Mater.*, 2005, 4, 11, 864–868.

[58] P. Boland, K. Lee, G. Namkoong, *Sol. Energy Mater. Sol. Cells*, 2010, 94, 5, 915–920.

[59] J. Peet, J. Y. Kim, N. E. Coates, W. L. Ma, D. Moses, A. J. Heeger, G. C. Bazan, *Nat. Mater.*, 2007, 6, 7, 497–500.

[60] Y. Yuan, T. J. Reece, P. Sharma, S. Poddar, S. Ducharme, A. Gruverman, Y. Yang, J. Huang, *Nature materials*, 2011, 10.

[61] Z.-G. Zhang, J. Min, S. Zhang, J. Zhang, M. Zhang, and Y. Li, Chem.

Commun., 2011, 47, 33, 9474.

[62] G. J. Zhao, Y. J. He, Y. Li, *Adv. Mater.*, 2010, 22, 39, 4355–4358.

[63] Y. Liang, Z. Xu, J. Xia, S. T. Tsai, Y. Wu, G. Li, C. Ray, L. Yu, *Adv. Mater.*, 2010, 22, 20, 135–138.

[64] Y. Liang, Y. Wu, D. Feng, S. Tsai, H. Son, G. Li, L. Yu, *J. Am. Chem. Soc.*, 2009, 131, 1, 56–57.

[65] Y. Y. Liang, *J. Am. Chem. Soc.*, 2009, 131, 7792–7799.

[66] Z. N. Bao, W. K. Chan, L. P. Yu, *J. Am. Chem. Soc.*, 1995, 117, 12426.

[67] Y. Liang, L. Yu, *Acc. Chem. Res.*, 2010, 43, 9, 1227–1236.

[68] Z. He, B. Xiao, F. Liu, H. Wu, Y. Yang, S. Xiao, C. Wang, T. P. Russell, Y. Cao, *Nat. Photonics*, 2015, 9, 3, 174–179.

[69] T. M. Abdel-Fattah, E. M. Younes, G. Namkoong, E. M. El-Maghraby, A. H. Elsayed, A. H. Abo Elazm, *Synth. Met.*, 2015, 209, 348–354.

[70] P. Boland, S. S. Sunkavalli, S. Chennuri, K. Foe, T. Abdel-Fattah, G. Namkoong, *Thin Solid Films*, 2010, 518, 6, 1728–1731.

[71] F. Liu, W. Zhao, J. R. Tumbleston, C. Wang, Y. Gu, D. Wang, A. L. Briseno, H. Ade, T. P. Russell, *Adv. Energy Mater.*, 2014, 4, 5, 1–9.

[72] S. Guo, E. M. Herzig, A. Naumann, G. Tainter, J. Perlich, P. Müller-Buschbaum, *J. Phys. Chem. B*, 2014, 118, 1, 344–350.

[73] B. Carsten, F. He, H. J. Son, T. Xu, L. Yu, *Chem. Rev.*, 2011, 111, 3, 1493–1528.

[74] Y. Lin, J. Wang, Z.-G. Zhang, H. Bai, Y. Li, D. Zhu, X. Zhan, *Adv. Mater.*, 2015, 27, 7, 1170–1174.

[75] F. Zhang, Z. Zhuo, J. Zhang, X. Wang, X. Xu, Z. Wang, Y. Xin, J. Wang, J. Wang, W. Tang, Z. Xu, Y. Wang, *Sol. Energy Mater. Sol. Cells,* 2012, 97, 71–77.

[76] V. S. Balderrama, M. Estrada, P. L. Han, P. Granero, J. Pallarés, J. Ferré-Borrull, L. F. Marsal, *Sol. Energy Mater. Sol. Cells*, 2014, 125, 155–163.

[77] N. Miyaura, A. Suzuki, *Chem. Rev.*, 1995, 95, 7, 2457–2483.

[78] Z. He, C. Zhong, X. Huang, W. Y. Wong, H. Wu, L. Chen, S. Su, Y. Cao, *Adv. Mater*., 2011, 23, 40, 4636–4643.

[79] R. Kang, Y. J. Noh, J. M. Yun, H. Kim, N. Myoung, E. H. Lee, T. W. Kim, S. I. Na, S. H. Oh, *RSC Adv.*, 2017, 7, 43, 26689-26696.

[80] D. Zheng, W. Huang, P. Fan, Y. Zheng, J. Huang, J. Yu, *ACS Appl. Mater. Interfaces*, 2017, 9, 5, 4898-4907.

[81] J. G. Sánchez, V. S. Balderrama, S. I. Garduño, E. Osorio, A. Viterisi, M. Estrada, J. Ferré-Borrull, J. Pallarès, L. F. Marsal, *RSC Adv*., 2018, 8, 24, 13094–13102.

[82] L. L. Hench, J. K. West, *Chem. Rev.*, 1990, 90, 1, 33–72.

[83] T. Kuwabara, T. Nakayama, K. Uozumi, T. Yamaguchi, K. Takahashi, *Sol. Energy Mater. Sol. Cells*, 2008, 92, 11, 1476–1482.

[84] J. Li, S. Kim, S. Edington, J. Nedy, S. Cho, K. Lee, A. J. Heeger, M. C. Gupta, J. T. Yates, *Sol. Energy Mater. Sol. Cells*, 2011, 95, 4, 1123–1130.

[85] Y. C. Yeh, S. S. Li, C. C. Wu, T. W. Shao, P. C. Kuo, C. W. Chen, *Sol. Energy Mater. Sol. Cells*, 2014, 125, 233–238.

[86] J. Y. Kim, S. H. Kim, H. H. Lee, K. Lee, W. Ma, X. Gong, A. J. Heeger, *Adv. Mater.,* 2006, 18, 5, 572–576.

[87] Bayer AG, Eur. Patent 440 957, 1991.

[88] F. Jonas, W. Krafft, B. Muys, *Macromol. Symp*., 1995, 100, 169.

[89] B. Ecker, J. C. Nolasco, J. Pallarès, L. F. Marsal, J. Posdorfer, J. Parisi, E. Von Hauff, *Adv. Funct. Mater.*, 2011, 21, 14, 2705–2711.

[90] J. Meyer, S. Hamwi, M. Kröger, W. Kowalsky, T. Riedl, A. Kahn, *Adv. Mater*., 24, 40, 5408–5427.

[91] P. C. Sukanek, *J. Imag. Technol.*, 1985, 11(4): 184–190.

[92] L. E. Scriven, *MRS proceedings*, 1988, 121.

[93] Laurell Technologies. Spin coater. Information obtained from: http://www.laurell.com/spin-coater/?model=400B-6NPP/LITE

[94] E. Tekin, P. J. Smith, U. S. Schubert, *Soft Matter,* 2008, 4, 4, 703–713.

[95] M. Singh, H. M. Haverinen, P. Dhagat, G. E. Jabbour, *Adv. Mater.*, 2010, 22, 6, 673-685.

[96] T. M. Eggenhuisen, Y. Galagan, A. F. K. V. Biezemans, T. M. W. L. Slaats, W. P. Voorthuijzen, S. Kommeren, S. Shanmugam, J. P. Teunissen, A. Hadipour, W. J. H. Verhees, S. C. Veenstra, M. J. J. Coenen, J. Gilot, R. Andriessen, W. A. Groen, *J. Mater. Chem. A*, 2015, 3, 14, 7255-7262.

[97] F. Villani, P. Vacca, G. Nenna, O. Valentino, G. Burrasca, T. Fasolino, C. Minarini, D. della Sala, *J. Phys. Chem. C*, 2009, 113, 30, 13398-13402.

[98] Fujifilm. Dimatix Materials Printer. Information obtained from: http://www.fujifilmusa.com/products/industrial_inkjet_printheads/deposition-products/dmp-2800/

[99] Thin Film Processes II Book, 1st Edition, 1991, Part II-2.

[100] X. Yang, J. K. J. van Duren, R. A. J. Janssen, M. A. J. Michels, J. Loos, *Macromolecules,* 2004, 37, 2151.

[101] A. Guerrero, H. Heidari, T. S. Ripolles, A. Kovalenko, M. Pfannmöller, S. Bals, L.-D. Kauffmann, J. Bisquert, G. Garcia-Belmonte, *Adv. Energy Mater.*, 2015, 5, 7, 1401997.

[102] H. Bin Yang, Q. L. Song, C. Gong, and C. M. Li, *Sol. Energy Mater. Sol. Cells,* 2010, 94, 5, 846–849.

[103] A. Seemann, T. Sauermann, C. Lungenschmied, O. Armbruster, S. Bauer, H. J. Egelhaaf, J. Hauch, *Sol. Energy,* 2011, 85, 6, 1238–1249.

[104] W. Cai, X. Gong, Y. Cao, *Sol. Energy Mater. Sol. Cells,* 2010, 94, 2, 114–127.

[105] M. Jørgensen, K. Norrman, S. A. Gevorgyan, T. Tromholt, B. Andreasen, F. C. Krebs, *Adv. Mater.,* 2012, 24, 5, 580–612.

[106] S. A. Gevorgyan, M. Jørgensen, F. C. Krebs, *Sol. Energy Mater. Sol. Cells,* 2008, 92, 7, 736–745.

[107] J. Meyer, S. Hamwi, M. Kröger, W. Kowalsky, T. Riedl, A. Kahn, *Adv. Mater.,* 2012, 24, 40, 5408–5427.

[108] R. C. I. Mackenzie, V. S. Balderrama, S. Schmeisser, R. Stoof, S. Greedy, J. Pallarès, L. F. Marsal, A. Chanaewa, E. von Hauff, *Adv. Energy Mater*, 2016, 6, 4, 1501742.

[109] K. Zilberberg, S. Trost, J. Meyer, A. Kahn, A. Behrendt, D. Lützenkirchen-Hecht, R. Frahm, T. Riedl, *Adv. Funct. Mater.*, 2011, 21, 24, 4776–4783.

[110] G. Terán-Escobar, J. Pampel, J. M. Caicedo, M. Lira-Cantú, *Energy Environ. Sci.,* 2013, 6, 3088.

[111] A. Kösemen, Z. Alpaslan Kösemen, B. Canimkubey, M. Erkovan, F. Başarir, S. E. San, O. Örnek, A. V. Tunç, *Sol. Energy*, 2016, 132, 511–517.

[112] A. Ko, C. Ulbricht, O. Usluer, D. Ayuk, M. Egbe, Y. Yerli, *Sol. Energy*, 2014, 99, 88–94.

[113] S. H. Kim, S. H. Park, K. Lee, *Curr. Appl. Phys.,* 2010, 10, 3, S528–S531.

[114] M. O. Reese, S. A. Gevorgyan, M. Jørgensen, E. Bundgaard, S. R. Kurtz, D. S. Ginley, D. C. Olson, M. T. Lloyd, P. Morvillo, E. A. Katz, A. Elschner, O. Haillant, T. R. Currier, V. Shrotriya, M. Hermenau, M. Riede, K. R. Kirov, G. Trimmel, T. Rath, et. al., *Sol. Energy Mater. Sol. Cells,* 2011, 95, 5, 1253.

[115] P. Kumar, C. Bilen, B. Vaughan, X. Zhou, P. C. Dastoor, W. J. Belcher, *Sol. Energy Mater. Sol. Cells,* 2016, 149, 179–186.

[116] Z. Lin, C. Jiang, C. Zhu, J. Zhang, *ACS Appl Mater Inter,* 2013, 5, 3, 713.

[117] K. Lee, J. Y. Kim, S. H. Park, S. H. Kim, S. Cho, A. J. Heeger, *Adv. Mater.*, 2007, 19, 18, 2445–2449.

[118] J. Xiong, B. Yang, C. Zhou, J. Yang, H. Duan, *Org. Electron.,* 2014, 4, 835–843.

[119] H. Sun, J. Weickert, H. C. Hesse, L. Schmidt-Mende, *Sol. Energy Mater. Sol. Cells*, 2011, 95, 12, 3450–3454.

[120] B. Y. Finck, B. J. Schwartz, *Appl. Phys. Lett.*, 2013, 103, 5, 1–4.

[121] A. Wagenpfahl, D. Rauh, M. Binder, C. Deibel, V. Dyakonov, *Phys. Rev.*, 2010, 82, 115306, 9.

[122] B. Ecker, H. J. Egelhaaf, R. Steim, J. Parisi, E. von Hauff, *J. Phys. Chem. C,* 2012, 116, 31, 16333–16337.

[123] B. Romero, G. Del Pozo, E. Destouesse, S. Chambon, B. Arredondo, *Org. Electron. physics, Mater. Appl.*, 2014, 15, 12, 3546–3551.

[124] X. Wang, C. Xinxin Zhao, G. Xu, Z. K. Chen, F. Zhu, *Sol. Energy Mater. Sol. Cells*, 2012, 104, 1–6.

[125] M. P. Nikiforov, J. Strzalka, S. B. Darling, *Sol. Energy Mater. Sol. Cells*, 2013, 110, 36–42.

[126] T. Endale, E. Sovernigo, A. Radivo, S. Dal Zilio, A. Pozzato, T. Yohannes, L. Vaccari, M. Tormen, *Sol. Energy Mater. Sol. Cells*, 2014, 123, 150–158.

[127] Z. Li, G. Lakhwani, N. C. Greenham, C. R. McNeill, *J. Appl. Phys.*, 2013, 114, 3.

[128] J. Pallarès, R. Cabré, L. F. Marsal, R. E. I. Schropp, *J. Appl. Phys.*, 2006, 100, 8.

[129] D. Rathee, S. K. Arya, M. Kumar, *Journal of semiconductors,* 2012, 33, 2, 022001-1 - 022001-4.

[130] S. Thiagarajan, M. Thaiyan, R. Ganesan, *New J. Chem.,* 2015, 39, 9471 – 9479.

[131] H. Zhicai, C. Zhong, S. Su, M. Xu, H. Wu, Y. Cao, *Nature Photon.,* 2012, 6, 591 – 595.

[132] O. Carp, C. L. Huisman, A. Reller, *Prog. Solid St Chem,* 2004, 32 (1–2), 33–177.

[133] M. Thambidurai, J. Y. Kim, H. Song, Y. Ko, N. Muthukumarasamy, D. Velauthapillai, V. W. Bergmann, S. A. L. Weber, C. Lee, *J. Mater. Chem. A*, 2014, 2, 29.

[134] S. Yuan, Y. Zhang, W. Liu, W. Zhang, *Electrochim. Acta*, 2014, 116.

[135] J. You, C. C. Chen, L. Dou, S. Murase, H. S. Duan, S. A. Hawks, T. Xu, H. J. Son, L. Yu, G. Li, and Y. Yang, *Adv. Mater.*, 2012, 24, 38, 5267–5272.

[136] M. Thambidurai, J. Y. Kim, Y. Ko, H.-J. Song, H. Shin, J. Song, Y. Lee, N. Muthukumarasamy, D. Velauthapillai, C. Lee, *Nanoscale*, 2014, 6, 15, 8585–9.

[137] F. J. Lim, A. Krishnamoorthy, G. W. Ho, *ACS Appl. Mater. Interfaces,* 2015, 7, 12119−12127

[138] M. Xu, X. Zhu, X. Shi, J. Liang, Y. Jin, Z. Wang, and L. Liao, *ACS Appl. Mater. Interfaces*, 2013, 5, 2935–2942.

[139] Y. Liu, J. Zhao, Z. Li1, C. Mu, W. Ma, H. Hu, K. Jiang, H. Lin, H. Ade, H. Yan, *Nat. Commun.,* 2014, 5:5293, 9.

[140] S. H. Liao, H. J. Jhuo, P. N. Yeh, Y. S. Cheng, Y. L. Li, Y. H. Lee, S. Sharma, S. A. Chen, *Sci. Rep.,* 2015, 4, 1, 6813.

[141] J. Zhao, Y. Li, G. Yang, K. Jiang, H. Lin, H. Ade, W. Ma, H. Yan, *Nat. Energy,* 2016, 1, 2, 15027.

[142] M. A. Green, Y. Hishikawa, W. Warta, E. Dunlop, D. Levi, J. Hohl-Ebinger, A. Ho-Baillie, *Prog. Photovoltaics Res. Appl.,* 2017, 25, 7, 668-676.

[143] X. Gu, Y. Zhou, K. Gu, T. Kurosawa, Y. Guo, Y. Li, H. Lin, B. C. Schroeder, H. Yan, F. Molina-Lopez, C. J. Tassone, C. Wang, S. C. B. Mannsfeld, H. Yan, D. Zhao, M. F. Toney, Z. Bao, *Adv. Energy Mater.*, 2017, 7, 1602742

[144] R. Søndergaard, M. Hösel, D. Angmo, T. T. Larsen-Olsen, F. C. Krebs, *Mater. Today,* 2012, 15, 1, 36–49.

[145] S. C. Lim, J. B. Koo, C. W. Park, S. W. Jung, B. S. Na, S. S. Lee, H. Y. Chu, *Jpn. J. Appl. Phys.,* 2014, 53, 5S3, 05HB10.

[146] V. T. Tran, Y. Wei, H. Yang, Z. Zhan, H. Du, *Nanotechnology,* 2017, 28, 9, 95204.

[147] A. Singh, S. K. Gupta, A. Garg, *Org. Electron.,* 2016, 35, 118-127.

[148] Sigma-Aldrich. ZnO nanoparticle ink. Information obtained from sigma-Aldrich: *http://www.sigmaaldrich.com/catalog/product/aldrich/793361?lang=es&region=ES*

[149] S. H. Liao, H. J. Jhuo, Y. S. Cheng, S. A. Chen, *Adv. Mater.,* 2013, 25, 34, 4766-4771.

[150] P. Lv, S. C. Chen, Q. Zheng, F. Huang, K. Ding, *Appl. Phys. Lett.,* 2015, 106, 16, 163902.

[151] D. Lee, T. Kang, Y. Choi and S. Oh, *J. Phys. Chem. Solids,* 2017, 105, 66–71.

[152] S. Oh, T. Kang, S. G. Oh, *Sol. Energy,* 2015, 120, 363-369.

[153] T. Kirchartz and J. Nelson, *Phys. Rev. B*, 2012, 86, 16, 1-12.

[154] D. Credgington, Y. Kim, J. Labram, T. D. Anthopoulos, J. R. Durrant, *J. Phys. Chem. Lett.,* 2011, 2, 2759-2763.

[155] D. Credgington, J. R. Durrant, *J. Phys. Chem. Lett.,* 2012, 3, 11, 1465-1478.

[156] A. Maurano, C. G. Shuttle, R. Hamilton, A. M. Ballantyne, J. Nelson, W. Zhang, M. Heeney, J. R. Durrant, *J. Phys. Chem. C,* 2011, 115, 5947-5957.

[157] T. M. Clarke, A. Ballantyne, S. Shoaee, Y. W. Soon, W. Duffy, M. Heeney, I. McCulloch, J. Nelson, J. R. Durrant, *Adv. Mater.,* 2010, 46, 22, 5287-91.

[158] T. M. Clarke, J. R. Durrant, *Chem. Rev.,* 2010, 11, 110, 6736-67.

[159] D. Credgington, R. Hamilton, P. Atienzar, J. Nelson, J. R. Durrant, *Adv. Funct. Mater.,* 2011, 14, 21, 2744-53.

[160] A. Maurano, R. Hamilton, C. G. Shuttle, A. M. Ballantyne, J. Nelson, B. O'Regan, W. Zhang, I. McCulloch, H. Azimi, M. Morana, C. J. Brabec, J. R. Durrant, *Adv. Mater.,* 2010, 44, 22, 4987.

[161] R. Shivanna, S. Shoaee, S. Dimitrov, S. K. Kandappa, S. Rajaram, J. R. Durrant, K. S. Narayan, *Energy Environ. Sci.,* 2014, 1, 7, 435-41.

[162] C. G. Shuttle, R. Hamilton, B. C. O'Regan, J. Nelson, J. R. Durrant, *Proc. Natl. Acad. Sci. U.S.A.,* 2010, 38, 107, 16448-52.

[163] C. G. Shuttle, A. Maurano, R. Hamilton, B. O'Regan, J. C. de Mello, J. R. Durrant, *Appl. Phys. Lett.,* 2008, 18, 93, 183501-3.

[164] C. G. Shuttle, B. O'Regan, A. M. Ballantyne, J. Nelson, D. D. C. Bradley, J. R. Durrant, *Phys. Rev. B: Condens. Matter Mater. Phys.,* 2008, 11, 78, 113201.

[165] P. L. Han, A. Viterisi, J. Ferre-Borrull, J. Pallarès, L. F. Marsal, *Org. Electron,* 2017, 41, 229-236.

[166] D. Fernandez, A. Viterisi, V. Challuri, J. W. Ryan, E. Martinez-Ferrero, F. Gispert-Guirado, M. Martinez, E. Escudero, C. Stenta, L. F. Marsal, E. Palomares*, ChemSusChem,* 2017, 10, 15, 3118-3134.

[167] A. Sánchez-Díaz, M. Izquierdo, S. Filippone, N. Martin, E. Palomares, *Adv. Funct. Mater.,* 2010, 16, 20, 2695-700.

[168] G. Garcia-Belmonte, P. P. Boix, J. Bisquert, M. Lenes, H. J. Bolink, A. La Rosa, S. Filippone, N. Martin, *J. Phys. Chem. Lett*., 2010, 17, 1, 2566-71.

[169] D. Fernandez, A. Viterisi, J. William Ryan, F. Gispert-Guirado, S. Vidal, S. Filippone, N. Martin, E. Palomares, *Nanoscale,* 2014, 11, 6, 5871-78.

[170] I. Etxebarria, A. Guerrero, J. Albero, G. Garcia-Belmonte, E. Palomares, R. Pacios, *Org. Electron.,* 2014, 11, 15, 2756-62.

[171] E. Barsoukov, J. R. MacDonald, *Wiley-Interscience,* 2005.

[172] G. Garcia-Belmonte, P. P. Boix, J. Bisquet, M. Sessolo, H. J. Bolink, *Sol. Energy Mater. Sol. Cells,* 2010, 94, 366 - 375.

[173] G. García-Belmonte, A. Munar, E. M. Barea, J. Bisquert, I. Ugarte, R. Pacios, *Org. Electron.,* 2008, 9, 847–851.

[174] A. Guerrero, N. F. Montcada, J. Ajuria, I. Etxebarria, R. Pacios, G. García-Belmonte, E. Palomares*, J. Mater. Chem. A*, 2013,1, 12345-12354.

[175] B. Ecker, H. J. Egelhaaf, R. Steim, J. Parisi, E. von Hauff, *J. Phys. Chem. C.,* 2012, 116, 31, 16333–16337.

[176] M. S. Suresh, *Sol. Energy Mater. Sol. Cells,* 1996, 43, 21-28.

[177] E. Osorio, J. G. Sánchez, L. N. Acquaroli, M. Pacio, J. Ferré-Borrull, J. Pallarès, L. F. Marsal, *ACS Omega,* 2017, 2, 7, 3091-3097.

[178] W. H. Press, S. A. Teukolsky, W. T. Vettering, B. P. Flannery, Numerical Recipes in C: The Art of Scientific Computing, 1994, second ed., Cambridge University Press.

UNIVERSITAT ROVIRA I VIRGILI
FABRICATION, CHARACTERIZATION AND MODELLING OF HIGH EFFICIENCY INVERTED POLYMER SOLAR CELLS
José Guadalupe Sánchez López

UNIVERSITAT
ROVIRA i VIRGILI